WESTFÄLISCHE WILHELMS-UNIVERSITÄT MÜNSTER

MASTER THESIS

Setup and commissioning of a Michelson interferometer for the demonstration of gravitational wave detection principles in outreach activities

Supervisor:
Prof. Dr. Alexander KAPPES

Second examiner:
Prof. Dr. Christian WEINHEIMER

A thesis submitted in the fulfillment of the requirements for the degree of
Master of Science *at* Westfälische Wilhelms-Universität Münster

by

David KOKE
AG Kappes
Institut für Kernphysik
Department of Physics

Wednesday 15th June, 2022

Contents

1 Introduction

Ever since the early beginnings of mankind, it has been part of human nature to want to understand their surroundings and environment. This desire extends not only to the immediate environment, but also to more general questions that humans have been trying to answer for millennia. Who are we? Where do we come from? What is the universe, and how does it work? To search for answers to these questions, astronomy was created by man as one of the most ancient sciences. Its beginnings are manifested in the observation of the stars with the naked eye, on the basis of which the first calendars were created. With increasing knowledge and technological progress, the observation methods were permanently improved. One of the most important milestones in astronomy was the development of the telescope in the 17^{th} century. Nowadays, it seems almost natural to use state-of-the-art telescopes to detect electromagnetic radiation in a broad wavelength range from the depths of space and, in this way, to constantly gain new insights into the universe and the processes taking place in it. In addition to perfecting existing observation techniques, entirely new methods have been created to learn about the universe in unprecedented ways. Significant turning points are the balloon flight of Viktor Hess in 1912, which led to the discovery of cosmic rays, or the supernova SN 1987A, in which a strong neutrino emission was detected by various neutrino observatories three hours before any visible light reached Earth [1]. The observational possibilities created by this are now part of the standard repertoire of astroparticle physics, for example in the form of the Pierre Auger Observatory, a cosmic ray observatory in Argentina, [2] or the IceCube Neutrino Observatory [3].

In the moment, the next door to the universe is being opened. The foundation for this was laid by Einstein who, in formulating the general theory of relativity in 1915 [4], also predicted the existence of gravitational waves. These describe wavelike perturbations in spacetime produced by accelerated masses, for example by binary black holes. However, because the effects of gravitational waves on spacetime are extremely small, Einstein doubted that they could ever be detected. Yet in September 2015, nearly 100 years after Einstein's work, the first direct observation of gravitational waves was achieved by the LIGO gravitational wave observatory [5]. LIGO consists of two detectors based on two Michelson interferometers, which, because of their enormous arm length of 4 km, are capable of measuring even the smallest distortions in spacetime. The field of gravitational wave astronomy, which has been opened up by this pioneering work, is to be extended in the coming decades by next generation observatories such as the Einstein Telecope [6]. These are to achieve significantly higher detection rates by using even larger detectors and technological improvements. It is hoped that this will provide revolutionary new insights into physical processes of the universe that are still unknown and not yet fully understood.

Especially in the case of young and exciting fields of physics such as gravitational wave astronomy, it is of great importance to make them tangible for people outside the academic world, for example pupils, within the framework of outreach activities. Besides increasing the general interest in physics, this can also awaken the interest and motivation of potential young scientists.

On the basis of this motivation, the objective of this master thesis is the design, setup, and commissioning of a Michelson interferometer to demonstrate the complex principles of gravitational wave detection in outreach activities.

2 Theory of gravitational waves

Much of our current knowledge about the universe originates from observations and measurements of electromagnetic radiation. Even the oldest part of this knowledge, derived from observing the stars, goes back to this method of observation. For a long time, the effects of gravitation were merely an everyday phenomenon, described by Newton's classical mechanics, and part of astronomy via Kepler's laws. The modern description of gravitation is Einstein's general relativity, which describes gravitation as a curvature of spacetime. An important consequence of general relativity is the existence of gravitational waves. These are emitted during many cosmic events in which large masses are accelerated. Although Einstein doubted that gravitational waves could ever be detected, they were directly detected for the first time in 2015, opening a new window for astronomy to observe the universe.

2.1 Description of gravitational waves by the general theory of relativity

In modern-day physics, gravitation is most precisely described by the general theory of relativity (GR). General relativity is the classical theory of gravitation, of which the core elements have been published by Albert Einstein in 1915 [4]. In general relativity, gravitation is not described as a classical Newtonian force. Instead, gravitation manifests itself in the curvature of spacetime, which in turn is caused by the distribution of mass and energy. Particles that are free of other forces move through spacetime along geodesic trajectories whose shape is determined by spacetime's curvature. Expressed in the words of theoretical physicist John Archibald Wheeler, "Geometry tells matter how to move, and matter tells geometry how to curve."[7]

The mathematical description of the relationship between the mass and energy distribution and the curvature of spacetime is given by Einstein's field equations, which, together with the equations of motion in the gravitational field, constitute the basic equations of general relativity. The field equations are a set of 10 second order coupled partial differential equations, given by [8, p. 358]

$$R_{\mu\nu} - \frac{1}{2} R g_{\mu\nu} = \frac{8\pi G}{c^4} T_{\mu\nu}. \tag{2.1.1}$$

The left side of eq. (2.1.1), which is often summarized as Einstein tensor $G_{\mu\nu} = R_{\mu\nu} - \frac{1}{2} R g_{\mu\nu}$, describes the curvature of spacetime. For this, the Ricci tensor $R_{\mu\nu}$ and the Ricci scalar R are employed, which are obtained by contraction of the Riemann curvature tensor, once and twice, respectively [8, p. 314]. The tensor $g_{\mu\nu}$ describes the metric of spacetime, which in general relativity, unlike in special relativity, has an intrinsic curvature. The right side of eq. (2.1.1) contains the field generating sources of gravitation via the stress-energy tensor $T_{\mu\nu}$ and G is the gravitational constant.

In the following, the effect of gravitational waves on matter will be considered in more detail. The derivations and examples are based on [8, ch. 16, 9, ch. 16]. For deeper insights and mathematical details the reader is referred to this literature.

In order to use Einstein's field equations to describe the propagation of gravitational waves, it is first assumed that the observer is far away from the gravitational waves' sources, and that the gravitational field around the observer is weak, but not stationary. Consequently, the metric can be written as

$$g_{\mu\nu} = \eta_{\mu\nu} + h_{\mu\nu}, \tag{2.1.2}$$

where $\eta_{\mu\nu}$ is the Minkowski metric known from special relativity, and $h_{\mu\nu} \ll 1$ is a small perturbation term. This assumption is commonly referred to as the weak field limit. Starting from the weak-field approximation and using the transverse-traceless gauge, it can be shown that the vacuum solutions of Einstein's field equations (the solutions of equation 2.1.1 for $T_{\mu\nu} = 0$) take the form of plane waves

$$h_{\mu\nu}(t, x, y, z) = A_{\mu\nu} e^{i(\mathbf{k}\cdot\mathbf{x} - \omega t)}, \tag{2.1.3}$$

which propagate at the speed of light. The term gravitational wave refers exactly to this wavelike propagation of the perturbation. The general solution is given by a superposition of these plane waves with different directions, frequencies, and amplitudes. Furthermore, it can be shown that using the transverse traceless gauge, only two degrees of freedom remain for the components of $A_{\mu\nu}$. For a gravitational wave propagating in the z-direction, for example, $A_{\mu\nu}$ can be written as

$$A_{\mu\nu} = \begin{pmatrix} 0 & 0 & 0 & 0 \\ 0 & A_+ & A_\times & 0 \\ 0 & A_\times & -A_+ & 0 \\ 0 & 0 & 0 & 0 \end{pmatrix} = A_+ \begin{pmatrix} 0 & 0 & 0 & 0 \\ 0 & 1 & 0 & 0 \\ 0 & 0 & -1 & 0 \\ 0 & 0 & 0 & 0 \end{pmatrix} + A_\times \begin{pmatrix} 0 & 0 & 0 & 0 \\ 0 & 0 & 1 & 0 \\ 0 & 1 & 0 & 0 \\ 0 & 0 & 0 & 0 \end{pmatrix}, \tag{2.1.4}$$

where A_+ and $A_\times$ are independent constants. Hence, $h_{\mu\nu}$ is a linear combination of two different solutions, which are also referred to as "+"-polarization and "×"-polarization (pronounced "plus" and "cross"). Although eq. (2.1.4) is specific to the propagation of a wave in the z-direction, any plane gravitational wave can be expressed in this form due of the free choice of coordinates.

The effects of gravitational waves on matter will now be examined by means of a simple example. For this, consider a "+"-polarized gravitational wave propagating in the z-direction, characterized by the perturbation term[1]

$$h_{\mu\nu}(t, \mathbf{0}) = \begin{pmatrix} 0 & 0 & 0 & 0 \\ 0 & A_+ & 0 & 0 \\ 0 & 0 & -A_+ & 0 \\ 0 & 0 & 0 & 0 \end{pmatrix} \sin(-\omega t). \tag{2.1.5}$$

The spacetime interval, which in a flat Minkowski-spacetime would be given by

[1] In physical applications only the real part of the plane wave solution, given by eq. (2.1.3), is relevant.

$$\begin{aligned} ds^2 &= g_{\mu\nu} dx^\mu dx^\nu \\ &= \eta_{\mu\nu} dx^\mu dx^\nu \\ &= -c^2 dt^2 + dx^2 + dy^2 + dz^2, \end{aligned} \tag{2.1.6}$$

now becomes

$$\begin{aligned} ds^2 &= g_{\mu\nu} dx^\mu dx^\nu \\ &= (\eta_{\mu\nu} + h_{\mu\nu})\, dx^\mu dx^\nu \\ &= -c^2 dt^2 + (1 + h_{xx})\, dx^2 + (1 + h_{yy})\, dy^2 + dz^2 \\ &= -c^2 dt^2 + (1 + A_+ \sin(-\omega t))\, dx^2 + (1 - A_+ \sin(-\omega t))\, dy^2 + dz^2. \end{aligned} \tag{2.1.7}$$

Additionally, consider two separate free test masses, one at rest at the origin[2] of the coordinate system, and the other at rest at $x = L^*, y = z = 0$. The spacetime distance between the two test masses in the x-direction is then given by

$$\begin{aligned} L(t) = \int_0^{L^*} \sqrt{g_{xx}}\, dx &= L^* \sqrt{1 + h_{xx}(t, \mathbf{0})} \\ &\approx L^* \left(1 + \frac{1}{2} h_{xx}(t, \mathbf{0})\right) \\ &= L^* \left(1 + \frac{1}{2} A_+ \sin(-\omega t)\right). \end{aligned} \tag{2.1.8}$$

The result shows that under the influence of the gravitational wave, the measured distance in spacetime $L(t)$ oscillates with the frequency ω of the wave. However, the coordinate distance of the two test masses does not change during this time. For illustration, this connection is shown in figure fig. 2.1.1.

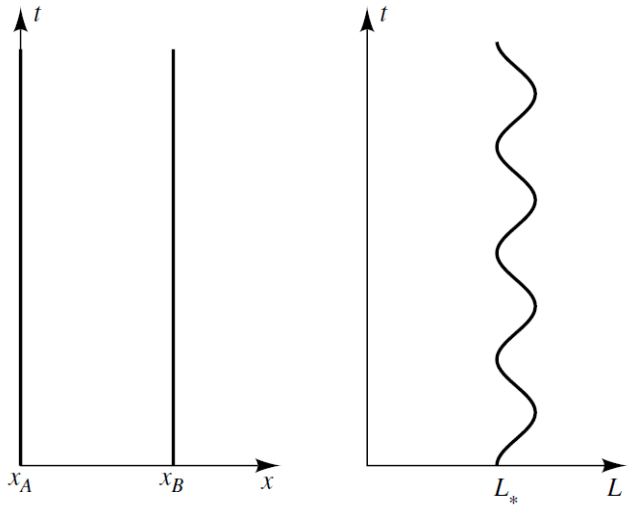

FIGURE 2.1.1: Motion of the test masses in the explained example. **Left:** The coordinates $x_A = 0$ and $x_B = L^*$ of the test masses remain identical during the period of time considered. **Right:** The spacetime distance $L(t)$ of the test masses oscillates around L^* with the frequency of the gravitational wave. The representation is strongly exaggerated. Taken from [9, p. 335].

[2] Denoted by the vector in three spatial coordinates $(x, y, z)^T = \mathbf{0}$

An important parameter to describe the effect of a gravitational wave on matter is the imposed strain, which describes the relative change in length in relation to the original length. Defining

$$\delta L := L(t) - L^*, \tag{2.1.9}$$

the strain is given by

$$\begin{aligned} \frac{\delta L}{L^*} &= \frac{1}{2} h_{xx}(t, \mathbf{0}) \\ &= \frac{1}{2} A_+ \sin(-\omega t). \end{aligned} \tag{2.1.10}$$

The considerations from this example can be applied analogously to a more general case. Suppose that the first test mass remains at the origin and that the second test mass is at a distance L^* from the origin in the direction of a unit vector $\mathbf{e}$ in the plane at $z = 0$ orthogonal to the direction of propagation of the gravitational wave. The strain is then

$$\frac{\delta L}{L^*} = \frac{1}{2} h_{ij}(t, \mathbf{0}) \mathbf{e}^i \mathbf{e}^j. \tag{2.1.11}$$

A better picture of the signature of a gravitational wave can be obtained if instead of only two test masses, a ring of several free test masses is considered. The ring is arranged in the xy-plane and the gravitational wave propagates in the z-direction. Figure 2.1.2 shows the changes of the test masses' distances during one period $0 \leq t \leq T$ of the gravitational wave, for a "+"-polarized gravitational wave (h_+, upper row) and a "×"-polarized gravitational wave ($h_\times$, lower row) respectively.

During the passage of a "+"-polarized gravitational wave, the particle ring is compressed in the x-direction for the first half of the period, and in the y-direction for the second half of the period. During the passage of a "×"-polarized gravitational wave, the particles on the

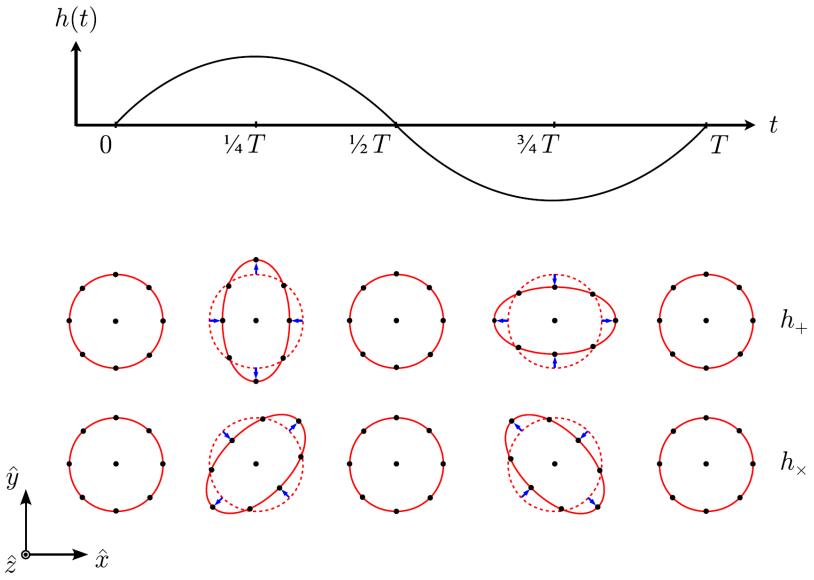

FIGURE 2.1.2: Influence of a gravitational wave on a ring of free test masses in the xy-plane. **Top:** Amplitude $h(t)$ of the perturbation term during a period T. **Bottom:** Behavior of the distances of the test masses during passage of a "+"-polarized (top row) and a "×"-polarized (bottom row) wave. Image taken from [10], adjusted.

ring behave analogously, with the axes along which the ring is compressed being tilted by 45 degrees. The two possible polarizations of a plane gravitational wave are thus linearly independent but can be transformed into each other by rotation of the coordinate system.

2.2 Astrophysical sources of gravitational waves

Gravitational waves are generated by accelerated masses. However, not every system of accelerated masses radiates gravitational waves. Since in physical systems energy and in a broader sense mass are conserved, no gravitational monopole radiation is possible [9, p. 502]. Furthermore, due to conservation of momentum, gravitational dipole radiation can also not exist. Instead, for the emission of gravitational waves, a system needs a non-zero mass quadrupole moment, which is given by [7, pp. 974, 9, pp. 499]

$$I_{ij} = \int d^3x \, \rho\,(t, \vec{x})\, x^i x^j, \tag{2.2.1}$$

where $\rho\,(t, \vec{x})$ is the rest-mass density of the system. The total energy radiated by a source per unit of time is referred to as luminosity L_{GW} and depends directly on the trace-free part ("reduced part") of the mass quadrupole moment, [8, p. 455]

$$\mathcal{I}_{ij} = I_{ij} - \frac{1}{3}\delta_{ij} I^k_k. \tag{2.2.2}$$

The connection between the reduced quadrupole moment and the luminosity is given by Einstein's quadrupole formula [8, p. 465]

$$L_{\mathrm{GW}} = -\frac{dE}{dt} = \frac{G}{5}\left\langle \dddot{\mathcal{I}}_{ij} \dddot{\mathcal{I}}^{ij} \right\rangle. \tag{2.2.3}$$

Here, the square brackets denote the averaging over one period of the emitted wave. The dots mark the threefold time derivative. In direct consequence from eq. (2.2.3) spherically symmetric objects cannot emit gravitational waves, because for them $\ddot{\mathcal{I}}_{ij}$ vanishes [9, p. 507].

There are several known types of astrophysical objects that have a non-zero mass quadrupole moment and a high enough mass and acceleration to emit detectable gravitational waves at various frequency ranges and strains. An overview is presented in fig. 2.2.1. Depending on the source, gravitational wave events can be divided into several categories:

- **Continuous gravitational waves** with nearly constant frequency are expected to be emitted by the galactic population of rapidly rotating neutron stars (also called "pulsars"). If such neutron stars deviate from perfect spherical symmetry, they possess a mass quadrupole moment and emit gravitational waves with amplitudes that depend on the star's deformation and frequency [11]. The expected frequency and strain range for sources of this type is indicated by the box labeled "Pulsars" in fig. 2.2.1.
- **Binary inspirals** are collapses of binary systems of compact heavy objects, which continuously reduce their orbit until they finally merge. Depending on the mass of the objects, one distinguishes different types. The first type includes compact binary inspirals consisting of binary neutron stars, binary black holes with a few solar masses, or

systems consisting of a neutron star and a black hole [13]. Massive and supermassive binary inspirals refer to the collapse of systems of heavier black holes, the latter being associated with the merger of two galaxies with supermassive black holes at their centers. Furthermore, extreme mass ratio inspirals occur when compact stellar-mass objects collapse into supermassive black holes at galaxy centers [11]. The first directly detected gravitational wave, as well as all other events detected to date, fall into this category [14, 15]. Typical strain and frequency ranges are marked in fig. 2.2.1 by the corresponding boxes.

- The emission of **transient burst gravitational waves** is expected from several sources such as supernovae [16] (see box "Core collapse supernovae" in fig. 2.2.1) and gamma-ray bursts [17], the gravitational wave emission behavior of which is not yet fully understood and modeled. Consequently, burst gravitational waves are hoped to provide new insight into yet unexplored parts of astrophysics.

- The **stochastic gravitational wave background** is a superposition of a large number of gravitational waves from different independent events. The main source of the stochastic background is assumed to be the physical processes immediately after the Big Bang - The background may therefore contain information about the origin and history of the early universe. Another part of the background is assumed to have been formed during the history of the universe by the merger of binary black holes and binary neutron stars [18].

As can be easily seen, the strains expected from gravitational waves are extremely small, with magnitudes between 10^{-14} and 10^{-22}. Additionally, there is a tendency towards lower strains for sources with higher frequencies, due to the lower masses of the objects involved.

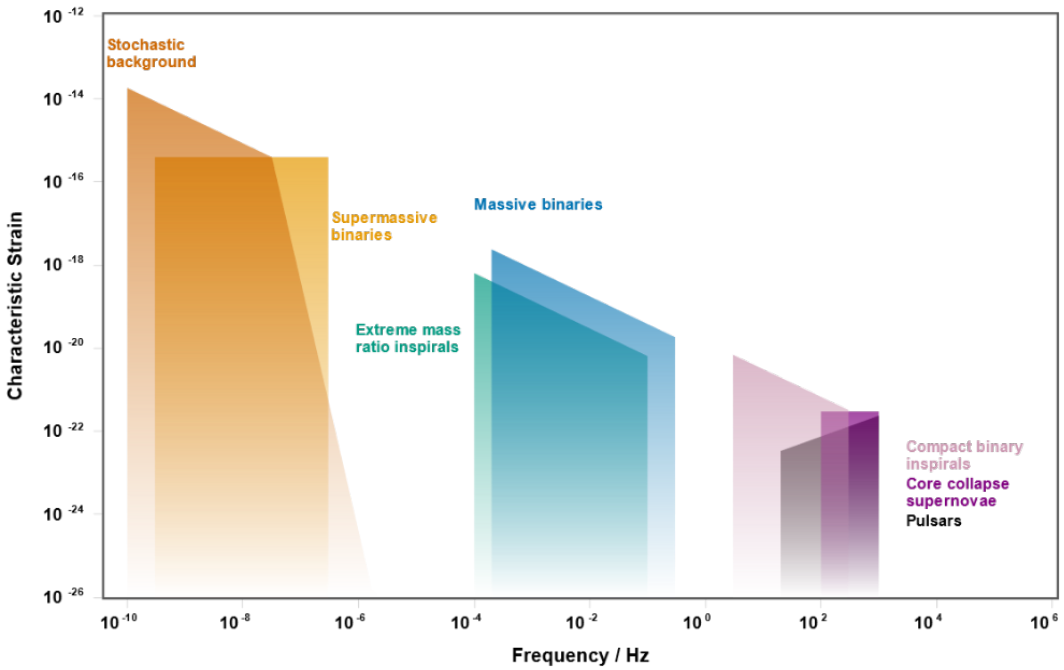

FIGURE 2.2.1: Overview of expected strains and frequencies of various gravitational wave sources. For the estimates, fiducial events were used as a reference - the amplitudes shown were chosen to be roughly consistent with the optimistic end of current estimates. For a detailed discussion of the procedure, see [11]. Plot created with [12].

3 Interferometers and Gravitational Wave Detection

For the detection of gravitational waves, interferometers are the most effective, and currently the only available tool. Since the construction of an interferometer is also the core subject of this thesis, the theory of the Michelson interferometer as well as its application in gravitational wave detection will be explained in the following sections.

3.1 The Michelson Interferometer

The Michelson interferometer is an amplitude-splitting interferometer, initially developed by Albert A. MICHELSON to detect the velocity of the Earth relative to a hypothetical luminiferous aether (Michelson-Morley experiment) [19]. Since then, it has been frequently used in many areas of physics due to its capability to reliably measure very small changes in distance. The structure of a Michelson interferometer is shown schematically in fig. 3.1.1.

The setup consists of an extended light source, a beamsplitter, two mirrors M_1 and M_2, and a detector or screen at the interferometer output. The source emits a light wave, one part of which moves towards the beamsplitter. There, a part of the wave is reflected in the direction of M_2, and the other part of the wave is transmitted in the direction of M_1. The mirrors reflect the incoming rays back to the beamsplitter. Part of the wave reflected by M_2 is reflected back to the light source, and the remaining part is transmitted to the detector. Similarly, part of the light reflected by M_1 is transmitted to the light source, while the other part is reflected to the detector. The two partial beams hitting the detector interfere depending on their phase difference caused by the different lengths of the interferometer's arms.

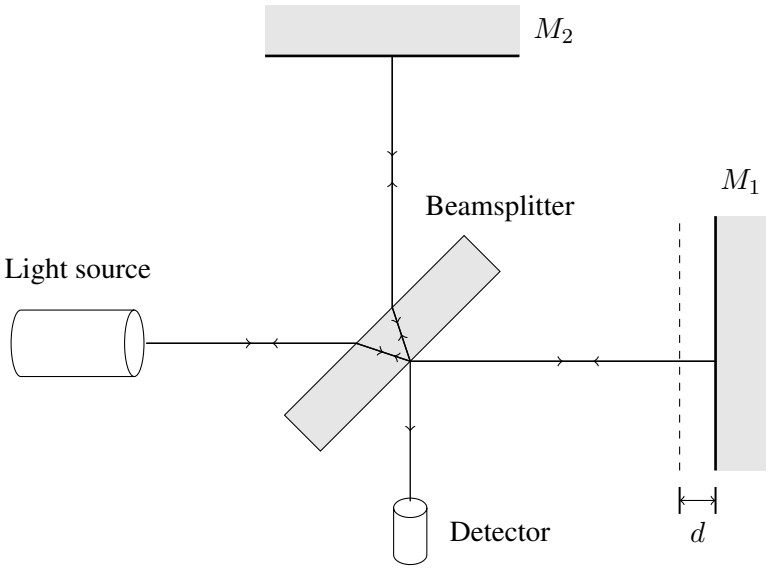

FIGURE 3.1.1: Generalized schematic representation of a Michelson interferometer. The arrowheads symbolize the superposition of the light beams in both directions. The dashed line represents the position of the mirror M_2 with respect to the beamsplitter, projected onto the beam path from the beamsplitter to the mirror M_1. The arm length difference (ignoring the thickness of the beamsplitter) is d.

It can be shown that the total irradiance of the partial beams arriving at the detector is given by

$$I = I_1 + I_2 + 2\sqrt{I_1 I_2}\cos(\Delta\phi), \tag{3.1.1}$$

where I_1 and I_2 describe the intensities of the interfering light beams, and $\Delta\Phi$ describes their phase difference [20, p. 765]. Assuming that the light source has an irradiance I_0 and that the beamsplitter has a reflection to transmission ratio of 50 to 50, the intensities of the partial beams at the detector are $I_1 = I_2 = 0.25I_0$. Equation 3.1.1 thus becomes

$$I = 0.5I_0\,(1 + \cos(\Delta\phi)). \tag{3.1.2}$$

As can easily be seen, total constructive interference occurs for $\cos(\Delta\phi) = 1$, i. e. for

$$\Delta\phi = (2n)\cdot\pi,\ n \in \mathbb{Z}, \tag{3.1.3}$$

while total destructive interference occurs for $\cos(\Delta\phi) = -1$, i.e.

$$\Delta\phi = (2n+1)\cdot\pi,\ n \in \mathbb{Z}. \tag{3.1.4}$$

The phase difference is related to the path difference via

$$\Delta\phi = \frac{2\pi}{\lambda}\Delta s. \tag{3.1.5}$$

When calculating the path difference, it must be considered that a light beam arriving at the detector after reflection at M_2 has passed the beamsplitter a total of three times, while the light beam that was reflected at M_1 only passed the beamsplitter once. Therefore, if a broadband light source is used, a compensator plate (an exact duplicate of the beamsplitter without reflective coating) must be inserted into the beam path between the beamsplitter and M_1 to compensate for the beamsplitter's dispersion[3] [20, p. 813]. If, as in the context of this work, only monochromatic light is used, it is sufficient to adjust the length of one interferometer arm to compensate for the thickness of the beamsplitter.

The exact appearance of the interference pattern at the interferometer output depends strongly on the chosen light source. For the previous discussions, a single light beam from an extended source was considered. If now a well collimated laser beam is considered, the emitted light can be described approximately as plane waves. Thus, at the interferometer output, a single illuminated spot with the diameter of the laser beam can be expected, the brightness of which depends on the interference condition. If, on the other hand, a light

[3]Dispersion: Dependence of the refractive index of a medium (in this case the beamsplitter) on the wavelength of the incident light [20, p. 143]

source with a divergent beam is used, a different image can be expected at the interferometer output. This shall now be derived in greater detail.

To illustrate the beam paths, it is useful to virtually rearrange the components of the interferometer as shown in fig. 3.1.2. To do this, the interferometer arm with mirror M_1 is projected onto the arm with mirror M_2, such that a virtual mirror M_1' is created. Starting from the detector or screen, located in the plane D, light arrives only from one direction. Thus, the detector "sees" two images of the light source S, which is physically located in the plane Σ. One image, labeled S_2, emanates from mirror M_2, and is located in the plane Σ_2. The image, labeled S_1, emanates from the mirror M_1' and is located in the plane Σ_1.

Now consider two beams of light emitted from S at different angles in the xz-plane so that both beams are incident on the detector at point P. The exact beam path is shown in fig. 3.1.2. If the distances between the components are assumed as shown in the figure, it can easily be found that the distances s_1 and s_2 traveled by the beams emerging from S_1 and S_2 are given by

$$\begin{aligned} s_1 &= \sqrt{(2a+2d+c)^2+z^2} \qquad \text{and} \\ s_2 &= \sqrt{(2a+c)^2+z^2}. \end{aligned} \tag{3.1.6}$$

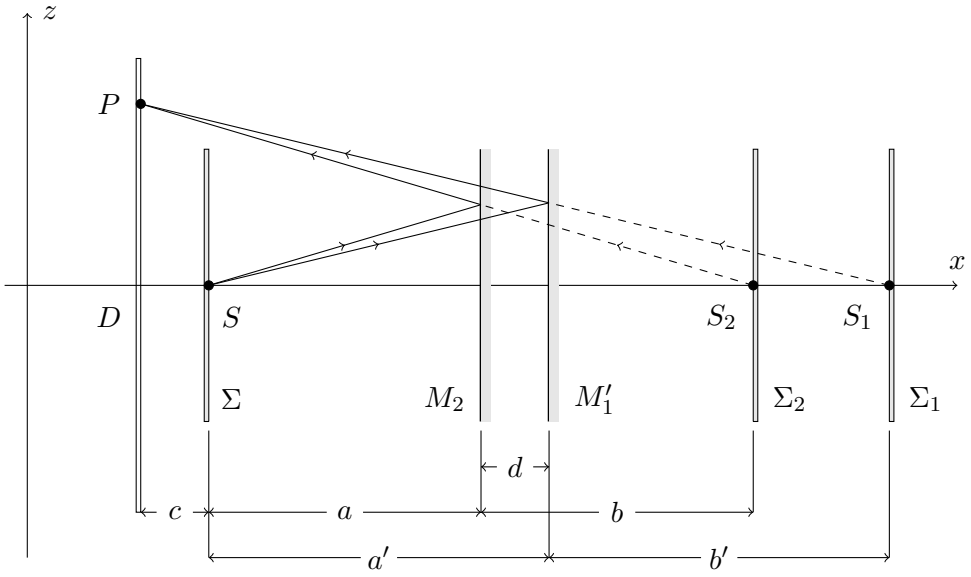

FIGURE 3.1.2: Schematic diagram explaining the formation of the interference pattern. S is the divergent light source. $M1'$ and M_2 are the mirrors, projected onto a single straight line. Σ_1 and Σ_2 are projections of the light source, as seen by the detector. The images S_1 and S_2 of the light sources emanate from Σ_1 and Σ_2. Because of the symmetry $a = b$ and $a' = b'$.

Given eq. (3.1.1), this results in an irradiance at P of

$$\begin{aligned} I &= I_1 + I_2 + 2\sqrt{I_1 I_2}\cos(\Delta\Phi) \\ &= I_1 + I_2 + 2\sqrt{I_1 I_2}\cos\left(\frac{2\pi}{\lambda}\Delta s\right) \\ &= I_1 + I_2 + 2\sqrt{I_1 I_2}\cos\left(\frac{2\pi}{\lambda}\sqrt{(2a+2d+c)^2+z^2} - \sqrt{(2a+c)^2+z^2}\right). \end{aligned} \tag{3.1.7}$$

To understand this result, the light intensity obtained from eq. (3.1.7) as a function of the position on the detector or screen is shown graphically in fig. 3.1.3. As can be easily seen, an interference pattern of alternating bright and dark concentric fringes is formed. The center fringe interferes constructively for $d = 2k \cdot \lambda/4,\ k \in \mathbb{N}$ (see figs. 3.1.3a and 3.1.3b) and destructively for $d = (2k+1) \cdot \lambda/4,\ k \in \mathbb{N}$. The distances between the fringes decrease as the path difference d increases (compare the upper and lower rows in fig. 3.1.3).

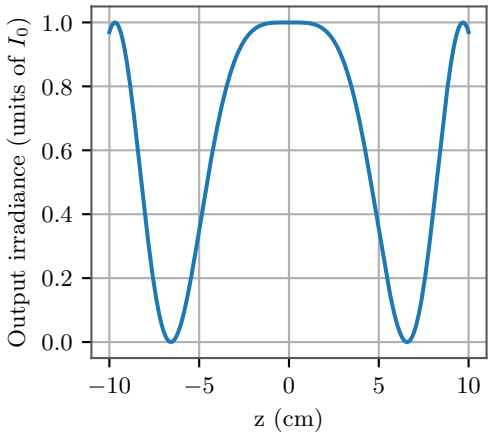

(A) 1d profile ($y = 0$) for $d = 5\lambda$

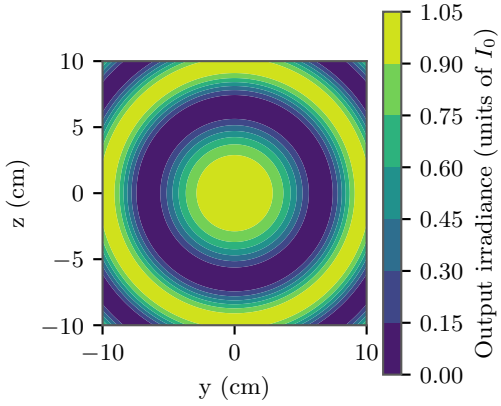

(B) Fringe pattern for $d = 5\lambda$

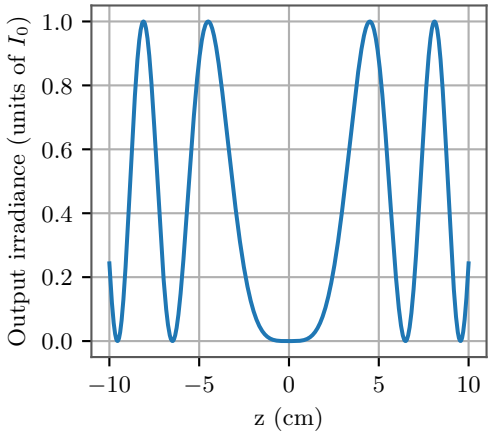

(C) 1d profile ($y = 0$) for $d = 10.25\lambda$

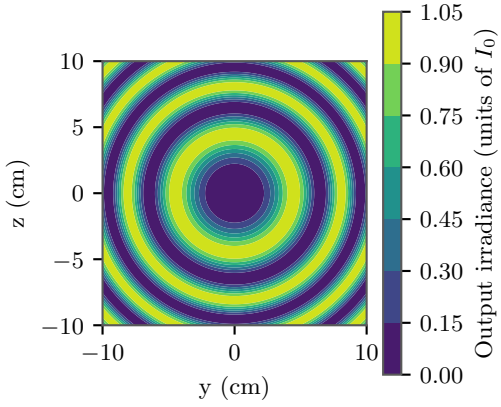

(D) Fringe pattern for $d = 10.25\lambda$

FIGURE 3.1.3: Example fringe patterns with $a = 10\,\text{cm}$ and $c = 0\,\text{cm}$ for two path differences. Upper row: $d = 5\lambda$, lower row: $d = 10.25\lambda$. The considered section of $10 \times 10\,\text{cm}$ corresponds approximately to the proportions of the real experimental setup.

3.2 Gravitational wave detection with interferometers

In section 2.1 the effects of gravitational waves on space-time and on free masses were discussed. These considerations will now be applied concretely to a Michelson interferometer in order to outline the basic working principles of current gravitational wave detectors.

Consider a "+"-polarized gravitational wave propagating in the z-direction and an interferometer located in the xy-plane as shown in fig. 3.2.1. Now, the time required for a light beam to travel from the beamsplitter at the origin of the coordinate system to the free mass M_1 at $x = L$ will be calculated. As has already been shown, eq. (2.1.7) holds for the space-time interval. Using that for two events in spacetime, which are separated by a light beam, $ds = 0$ holds, one gets

$$ds^2 = -c^2dt^2 + (1 + h_{xx})\, dx^2 + (1 + h_{yy})\, dy^2 + dz^2 = 0 \tag{3.2.1}$$

and thus

$$(1 + h_{xx})\, dx^2 + (1 + h_{yy})\, dy^2 + dz^2 = c^2dt^2. \tag{3.2.2}$$

The time required for the light beam to reach M_1 is therefore

$$t_1 := \int_{t_{BS}}^{t_{M_1}} dt = \frac{1}{c}\int_0^L \sqrt{1 + h_{xx}}dx \approx \frac{1}{c}\int_0^L \left(1 + \frac{1}{2}h_{xx}\right) dx, \tag{3.2.3}$$

and the travel time back to the beamsplitter analogously is

$$t_2 := \int_{t_{M_1}}^{t'_{BS}} dt = -\frac{1}{c}\int_L^0 \sqrt{1 + h_{xx}}dx \approx -\frac{1}{c}\int_L^0 \left(1 + \frac{1}{2}h_{xx}\right) dx. \tag{3.2.4}$$

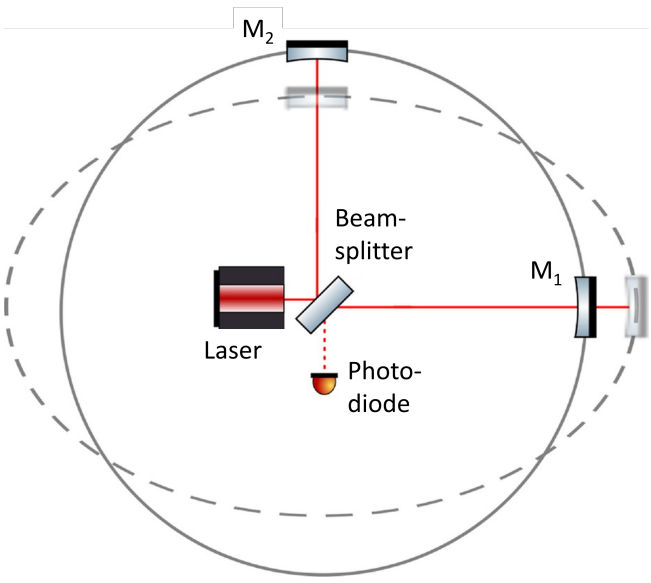

FIGURE 3.2.1: Schematic representation of the arm length change of a Michelson interferometer caused by a gravitational wave. The continuous circle describes the arm lengths in the unperturbed state, the dashed circle describes the arm lengths at the maximum displacement of the mirrors by the wave. Taken from [21], modified.

The total time of flight is

$$\Delta t_x := t_1 + t_2 = \frac{2L}{c} + \frac{1}{2c}\int_0^L h_{xx}dx - \frac{1}{2c}\int_L^0 h_{xx}dx. \tag{3.2.5}$$

Here we can easily distinguish the unperturbed part of the transit time from the part affected by the perturbation. Since we assume that the period of the gravitational wave is very long, h can be assumed to be approximately constant (for a more detailed argument, see [22]). Using this approximation for the integrals, one obtains

$$\Delta t_x = \frac{2L}{c} + \frac{L}{c}h_{xx}. \tag{3.2.6}$$

For the conditions chosen in this example, an analogous term Δt_y can be derived for the arm in the y-direction, with the only difference being the integration over h_{yy} instead of h_{xx}. Since $h_{yy} = -h_{xx} \equiv h_+$, the difference in travel time between the two arms is given by

$$\Delta t_y - \Delta t_x = \Delta t = \frac{2L}{c}h_+(t). \tag{3.2.7}$$

The phase difference at the interferometer output then is

$$\Delta\phi = \frac{2\pi c}{\lambda}h_+(t). \tag{3.2.8}$$

As can be seen from eq. (3.2.8), direct conclusions concerning the perturbation term of the gravitational wave can be drawn from the phase shift at the interferometer output. It must be considered, however, that the example given is a special case. In the general case, the gravitational wave can be of any polarization and have an arbitrary direction of incidence with respect to the interferometer plane. To localize the source of a gravitational wave or to make a precise statement about its polarization, measurements with several differently positioned and aligned interferometers are therefore necessary.

Enhancement of a Michelson interferometer for gravitational wave detection

As explained in section 2.2, the strains caused by gravitational waves are very small with $h \approx 10^{-21}$ at frequencies around 10^2 Hz. Since the induced phase shift at the interferometer output is proportional to the strain according to eq. (3.2.8), interferometers for gravitational wave detection must be extremely precise. The required measurement precision is easily illustrated by the example of the LIGO observatory [23], which consists of two Michelson interferometers with arm lengths of about 4 km (for a more detailed discussion of LIGO, see section 3.3.1). Assuming this arm length and a laser wavelength of $\lambda = 1064\,\text{nm}$, the transition from the dark fringe to the bright fringe (corresponding to an optical path length change of $\lambda/4$) would require a strain of

$$h = \frac{\Delta L}{L} = \frac{\lambda/4}{4\,\text{km}} \approx 10^{-10}. \tag{3.2.9}$$

This is eleven orders of magnitude larger than the maximum strain expected from gravitational waves in the considered frequency range.

To overcome the remaining orders of magnitude, various techniques are used in modern gravitational wave detectors, the most relevant of which will be briefly described; for a detailed discussion of these techniques, which go well beyond the scope of this thesis, the reader is referred to the cited literature in the following paragraphs.

One of the most important tools is the use of Fabry-Pérot resonators. These are resonant optical cavities created by inserting semitransparent mirrors into the interferometer arms. When these mirrors are separated by an integer number of $\lambda/4$ from the end mirrors, resonance occurs between the mirrors, causing the laser light to be reflected back and forth between the mirrors many times, depending on the reflection/transmission coefficients of the mirrors. The average number of reflections a light beam passes through in the cavity is called finesse. A higher finesse increases the effective optical path length, and thus also the sensitivity of the interferometer. A finesse of $\mathcal{O}(100)$ increases the sensitivity up to $\mathcal{O}(10^{-13})$ [24].

The remaining orders of magnitude are achieved by not only distinguishing between the bright and the dark fringe but by detecting the exact position between interference maximum and minimum via high-precision measurement of the interferometer output power (often referred to as "splitting the fringe"). To achieve the required precision, noise reduction is the primary design goal.

One of the main noise types in an interferometer is shot noise. This refers to the statistical fluctuation of the number N of photons that reach the output of the interferometer. Since the number of photons is generally Poisson distributed, one finds that the significance of the fluctuation decreases with larger N. To increase the number of photons at the interferometer output, so-called "power recycling" is used in modern interferometers in addition to a sufficiently strong laser. The concept of power recycling is based on the principle that the interferometer generally operates near the dark fringe. Consequently, most of the laser light is sent back to the light source and is not used. By installing a partially reflective mirror between the light source and the beamsplitter, another optical cavity can be formed which is in resonance with the whole interferometer and effectively stores the laser light, which would otherwise be dumped. This gives the effect of a laser that is more powerful by the number of the finesse of the cavity [25].

In some current detectors, the idea of using optical resonators is also applied to the interferometer output. In this case, the laser light used is modulated before being fed into the interferometer. If an incident gravitational wave now changes the optical path lengths in the interferometer, frequency sidebands are added to the light. This can be exploited by installing another partially reflecting mirror in the interferometer output, the location of which can be tuned so that resonance occurs for beats between the laser modulation frequency and the sidebands. As a result, gravitational wave signals are preferentially extracted at the output. This technique is called "signal recycling" [25, 24].

Besides shot noise, there are noise sources which cause a physical variation of the interferometer arm length. Two important noise sources of this kind are thermal noise, due to Brownian motion of the mirrors and losses in the wire material of the mirror suspensions [26], and seismic noise, caused by the persistent vibration of the surface of the earth's surface [27]. To reduce such noise, modern gravitational wave detectors employ sophisticated vacuum, cooling, and suspension mechanisms.

3.3 Current and future gravitational wave detectors

At the present time, there are several ground-based gravitational wave detectors in operation or in planning. In the scope of this introduction, two observatories will be discussed, one of which is in operation and the other in the planning phase.

3.3.1 LIGO

LIGO, acronym for Laser Interferometer Gravitational-Wave Observatory, is currently the largest gravitational wave detector [23]. It consists of two facilities, one in Hanford (Washington, USA) and one in Livingston (Louisiana, USA), each housing a Michelson interferometer with the modifications introduced in section 3.2 and an arm length of 4 km. The layout of the interferometers used is presented in fig. 3.3.1a. Exterior views of these facilities are presented in figs. 3.3.1c and 3.3.1d. LIGO was first commissioned in 1999 with the first measurements being conducted in the period from 2002 to 2010. Although no gravitational wave events were detected during this time, substantial scientific progress was made by finding observational limits on the strength and frequency of gravitational waves from a spectrum of possible sources [15].

From 2008 to 2015, numerous hardware improvements were implemented under the name “Advanced LIGO” (abbreviated “aLIGO”). These include but are not limited to the

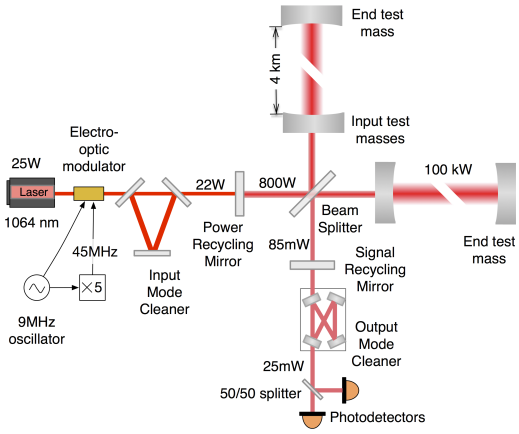

(A) Schematic layout of an aLIGO interferometer, as used identically at Hanford and Livingston. Included are the power and signal recycling structures described in section 3.2. Taken from [28].

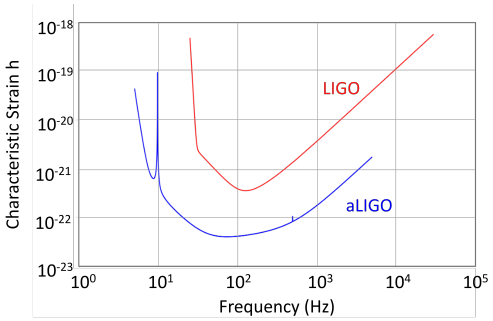

(B) Strain sensitivity curves for original LIGO and Advanced LIGO. Created with [12].

(C) Exterior view of the LIGO Hanford facility [29]

(D) Exterior view of the LIGO Livingston facility [29]

FIGURE 3.3.1: Illustration of the setup, sensitivity curves and exterior images of the LIGO observatory.

implementation of signal recycling and improvements to mirrors and seismic isolation [30]. In its current state, advanced LIGO has a peak sensitivity of below 10^{-22} Hz for source frequencies around 10^2 Hz, compared to a sensitivity of just below 10^{-21} Hz for the original LIGO design. The full sensitivity curves are displayed in fig. 3.3.1b.

The breakthrough result of LIGO is the first direct detection of gravitational waves, which was achieved in 2014 and for which the Nobel Prize in Physics was awarded in 2017 [5]. The source of the detected signal was the coalescence of a binary system consisting of two black holes with masses of 36 $M_\odot$ and 29 $M_\odot$, respectively. The signals recorded by the Hanford and Livingston detectors are depicted in fig. 3.3.2. The shown part of the inspiral is limited to two tenths of a second. As can be easily seen from the plot in frequency domain (bottom row of fig. 3.3.2), the rotation frequency of the system increases monotonically until the signal fades out immediately after the merger. Due to its importance, this signal is the perfect candidate for the exemplary signal of the setup that will be presented later in this work.

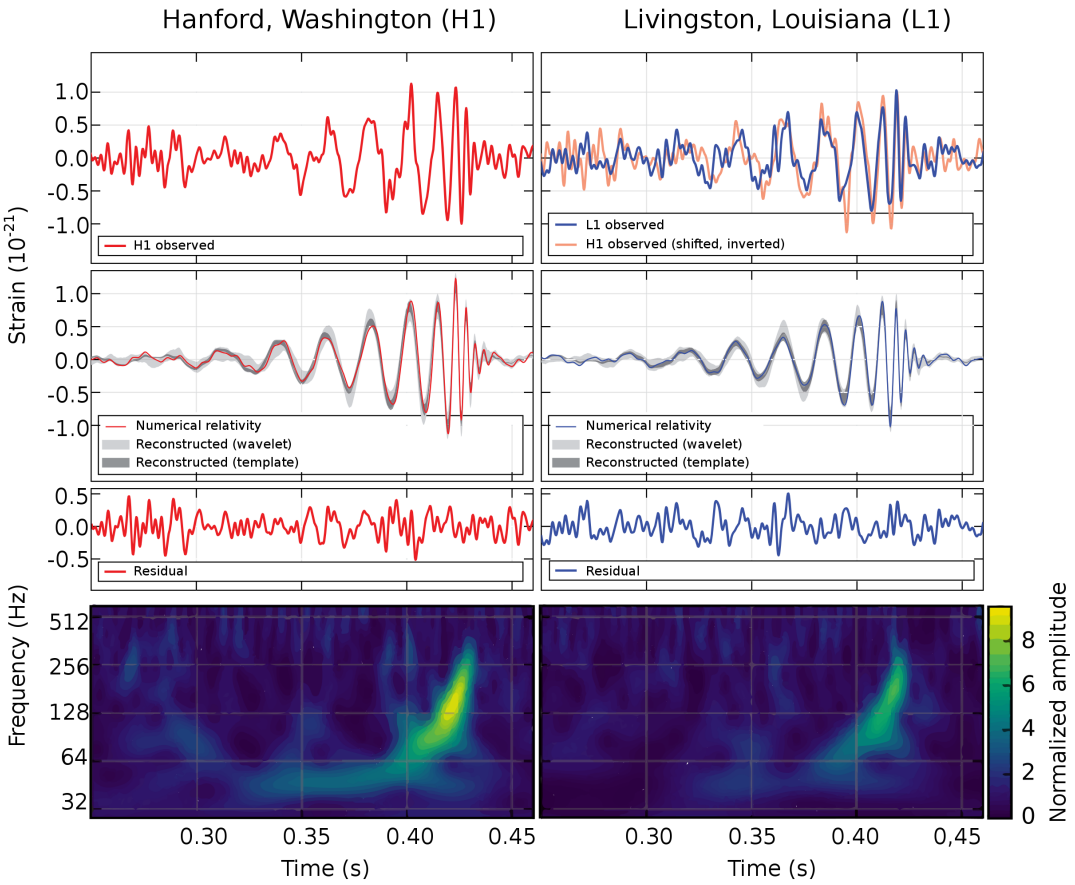

FIGURE 3.3.2: Gravitational wave event GW150914 recorded by LIGO in 2014. **Left column:** data from the Hanford site ("H1"), **right column:** data from the Livingston site ("L1"). **Top row:** strain observed by the detectors, on the right also compared with data from Hanford. Second row: Comparison of the waveform reconstructed from the measured data according to two different models (gray areas) with the theoretical model of a merger of two black holes with the corresponding masses (solid line). Third row: reconstruction subtracting measured data. **Bottom row:** representation of the signal in frequency space. Taken from [14].

3.3.2 Einstein Telescope

The Einstein Telescope is a proposed gravitational wave observatory currently in the design phase. As a next-generation[4] gravitational wave detector, the sensitivity will be improved by one order of magnitude in the entire detection frequency band (ranging from $\mathcal{O}(10\,\mathrm{Hz})$ to $\mathcal{O}(1\,\mathrm{kHz})$) compared to current observatories, such as aLIGO. To detect gravitational waves at lower frequencies, an extension of the detection range towards lower frequencies is planned. The intended design sensitivity, compared to aLIGO discussed in section 3.3.1, is shown in fig. 3.3.3a.

To achieve the desired sensitivity, fundamental design changes are planned compared to the L-shaped interferometers of the current generation [6]. The most important changes are the extension of the interferometer arms to 10 km and the location of the interferometers several hundred meters below the earth's surface to reduce the influence of seismic noise. The complete observatory will consist of three detectors arranged in an equilateral triangle. The triangular arrangement offers the advantage of equal sensitivity to both possible polarizations of a gravitational wave (see section 2.1) compared to an L-shaped detector. Each detector will contain two interferometers, one optimized for detection of low frequencies in the range from 3 Hz to 30 Hz, and the other optimized for detection of high frequencies in the range from 30 Hz to several kHz. For the six interferometers, the previously explained main concept, including power and signal recycling, as well as Fabry-Pérot resonators in the arms, will be used. A simplified illustration of the planned setup is included in fig. 3.3.3b.

Thanks to its high sensitivity, the Einstein Telescope will significantly increase the observational capabilities in gravitational wave astronomy [6]. Among other things, it will be possible to detect binary black hole coalescences in the range of tens to hundreds of solar masses even at cosmological distances, at expected event rates of 10^5 to 10^6 per year. This is hoped to provide new insights into the formation and binary evolution of black holes with stellar masses. Furthermore, the Einstein Telescope is planned to extend the range of observable black hole masses to both ends. On

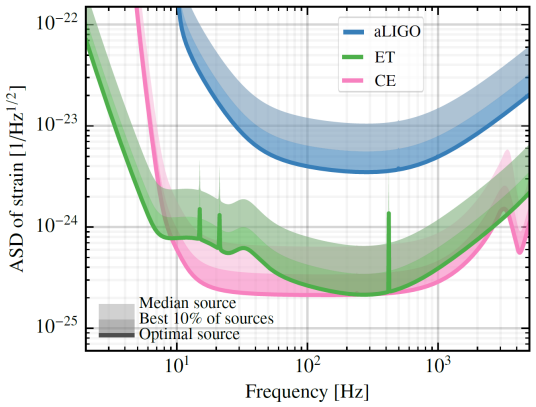

(A) Design sensitivity of the Einstein Telescope ("ET", green) compared to aLIGO (blue) and Cosmic Explorer ("CE", pink). Note that the sensitivity is plotted as the amplitude spectral density of the strain - therefore, the values can only be compared with the direct strains, as shown in fig. 3.3.1b, after conversion. The different color shades represent different source orientations and locations. The influence and characteristics of Cosmic Explorer are not studied in the scope of this thesis. Taken from [6].

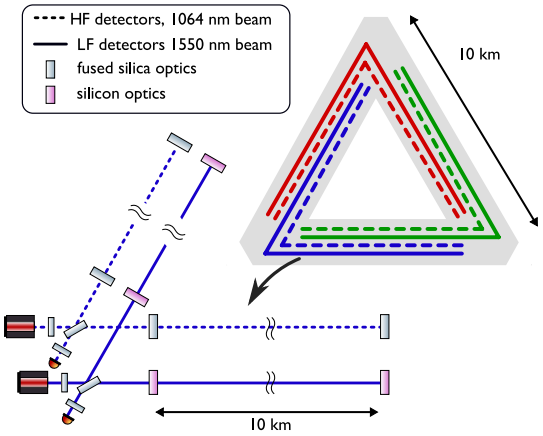

(B) Schematic illustration of the proposed setup of the Einstein telescope. Taken from [31].

FIGURE 3.3.3: Proposed design sensitivity and setup of the future Einstein Telescope.

[4]The Einstein Telescope is considered a third-generation gravitational wave detector, while detectors such as the original LIGO and aLIGO are considered first- and second-generation, respectively.

the top end, black holes with several thousand solar masses will be detectable (depending on the redshift). At the other end of the mass spectrum, hypothetical black hole binaries of primordial origin with a total mass of about one solar mass will also be detectable. Besides binary black hole coalescences, higher event rates are also expected to provide new insights into the formation mechanisms and demography of binary neutron stars, as well as insights regarding new astrophysical sources of gravitational waves, such as core collapse supernovae, and a stochastic gravitational wave background.

4 Piezoelectric effect and Preisach model

In the context of the outreach experiment, which was constructed for this work, piezoelectric actuators were used. Therefore, the piezoelectric effect will be briefly discussed in the following section. Since a significant part of this thesis deals with the correction of the nonlinear hysteretic behavior of piezoelectric actuators, the model used to correct the nonlinearity will also be introduced.

4.1 The piezoelectric effect

Materials are called piezoelectric, if they do not exhibit spontaneous electric polarization but can become electrically polarized by mechanical deformation. The cause of the piezoelectric effect is illustrated in fig. 4.1.1a. Every piezoelectric material, like the depicted crystal, contains isolated positive and negative charges, which are located at the opposite ends of the polar axes. If the crystal is deformed by an external force in the direction of a polar axis, the centers of the negative and positive charges are no longer at the same point, and an electric dipole is created, which can be measured as a voltage on the material [32, pp. 653-655].

Inversely, applying an electrical voltage to a piezoelectric material can induce deformation. This is referred to as the converse piezoelectric effect. For this reason, piezoelectric materials are often used in actuators for micro and nano positioning purposes. A well-known example is the positioning of the tip in scanning tunneling microscopes [32, p. 655]. In the scope of this work piezo actuators will be used for positioning with nanometer precision.

One of the disadvantages of piezoelectric actuators is the nonlinear relationship between the input voltage supplied to the actuator and the actuators displacement. The nonlinear relationship is due to hysteretic behavior of piezoelectric materials [34]. This hysteretic

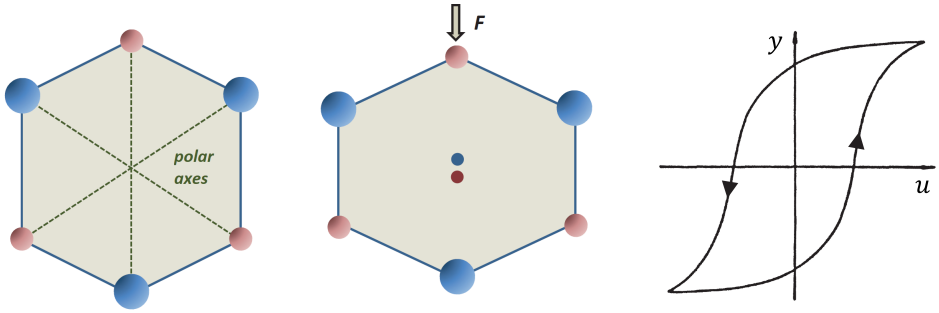

(A) Crystal lattice of a piezoelectric crystal with three polar axes. If the lattice is deformed along a polar axis by an external force F, the centers of the positive and negative charges are no longer located in the same place. Taken from [32, p. 645], translated.

(B) Example of a hysteresis curve for an input signal u and an output signal y. Taken from [33], modified.

FIGURE 4.1.1: Explanatory illustration of the piezoelectric effect and exemplary hysteresis curve.

behavior is exemplified in fig. 4.1.1b. When the voltage u applied to the actuator is increased, the displacement y increases in a nonlinear way. If the voltage is subsequently lowered again, the expansion decreases as well. However, the expansion lags behind the voltage change. The relationship between the applied voltage and the expansion of the actuator is, therefore, ambiguous. The shape of the hysteresis curve varies depending on the material used.

4.2 The Preisach hysteresis model

To be able to use piezo actuators for positioning without restrictions, the hysteresis must be corrected. This requires a mathematical model that describes the hysteresis in good approximation. In this thesis, the Preisach hysteresis model was implemented to this end. The Preisach model is a mathematical phenomenological model, which compared to physical-based models (e.g. the Jiles-Atherton model of hysteresis [35]) has the advantage that it is easier to implement and numerically robust [36]. The following mathematical explanations of the Preisach model are based on [33], to which the technically interested reader is referred.

The Preisach model is based on mathematical operators $R_{\beta,\alpha}$, which represent delayed relays. These relays are referred to as **hysterons**. The behavior of a hysteron operator is shown in fig. 4.2.1a. The operator has a switch-on threshold α and a switch-off threshold β, and can assume the output states $+1$ or -1. If the operator is cast on an input signal $u < \beta$, its output is $y = -1$. If the input u is now increased above the switch-on threshold α, the output of the operator changes to $y = 1$. If the input is now decreased below the switch-off threshold β, the output of the operator changes back to $y = -1$. Mathematically, the state of a hysteron can thus be written as

$$R_{\beta,\alpha}\left[u,\xi\right](t) = \begin{cases} -1, & \text{for } u(t) < \beta \\ \xi, & \text{for } \beta \leq u(t) \leq \alpha \\ 1, & \text{for } u(t) > \alpha \end{cases}, \quad (4.2.1)$$

where ξ describes the hysteron's current state, i.e. its state prior to the change of the input signal u.

A hysteretic system can be described by a continuous plane of hysterons, where one hysteron is assigned to each possible combination of on and off thresholds satisfying $\alpha > \beta$. The on and off thresholds are limited by the maximum values α_m and β_m, which correspond to the physical limits of the system. The half-plane in the coordinate space spanned by (α, β), which is described by

$$S = \{(\beta, \alpha) : \alpha \geq \beta,\ \alpha \leq \alpha_m,\ \beta \geq \beta_m\}, \quad (4.2.2)$$

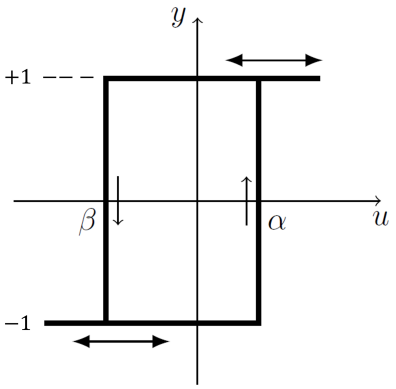

(A) Function of a single relay operator ("Hysteron"). Taken from [36], modified.

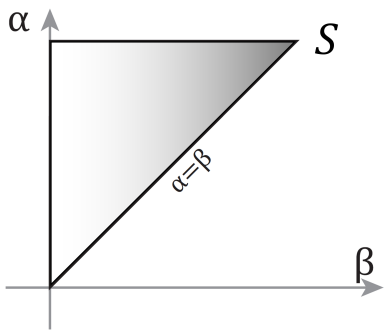

(B) Plot of the Preisach triangle S. Illustration based on [37].

FIGURE 4.2.1: Mathematical basis of the Preisach model. (A): A single hysteron. (B): Preisach triangle containing the hysterons.

forms the so-called **Preisach triangle**, which is illustrated in fig. 4.2.1b. The output $y(t)$ of a hysteretic system can be expressed as an integral

$$y(t) = \iint_{\alpha \geq \beta} \mu(\beta, \alpha) \, R_{\beta,\alpha}[u, \xi](t) d\beta d\alpha \tag{4.2.3}$$

over the Preisach triangle, where each hysteron is individually weighted by a non-negative weight function $\mu(\beta, \alpha)$.

Figure 4.2.2 illustrates how a hysteresis curve is approximated by the integral from eq. (4.2.3). Assume that the system is in an initial state in which all hysterons assume a value of -1 and therefore the output of the total system is minimal. If the input signal u, starting from its minimum value, is increased to $u = \alpha_1$, all the hysterons for which $\alpha < \alpha_1$ holds will be switched on. The Preisach triangle can then be divided horizontally into an area S^+ with hysterons in state $+1$, and an area S^- with hysterons in state -1. The output y increases with the area of S^+.[5] If the input signal is increased to its maximum value of $u_{\max} = \alpha_m$, all hysterons will be in the $+1$ state and the output will reach its maximum value. If the input signal is now lowered to $u = \beta_1$, all hysterons are switched off with $\beta > \beta_1$. Therefore, the dividing line between the areas S^+ and S^- moves vertically to the left and the output of the system decreases accordingly. In this way, the output of the signal follows any arbitrary variation of the input. If the input signal, as illustrated in fig. 4.2.2, is increased again to $u = \alpha_1$ and then decreased to $\beta_2 > \beta_1$, the line L dividing the Preisach triangle into two areas shows a step pattern, and the hysteresis curve shows so-called minor loops within the envelopes of the system.

The separation line L, also referred to as the system's memory curve, depends on the system's past inputs. Different memory curves can sometimes yield the same result of the integral and consequently the same output of the system. As a result, it is impossible to predict the response of the system to a change of input, if only the current input and output are known. Instead, the complete state of the Preisach triangle, i.e. the sum of all past inputs leading to the system's current state, must be known.

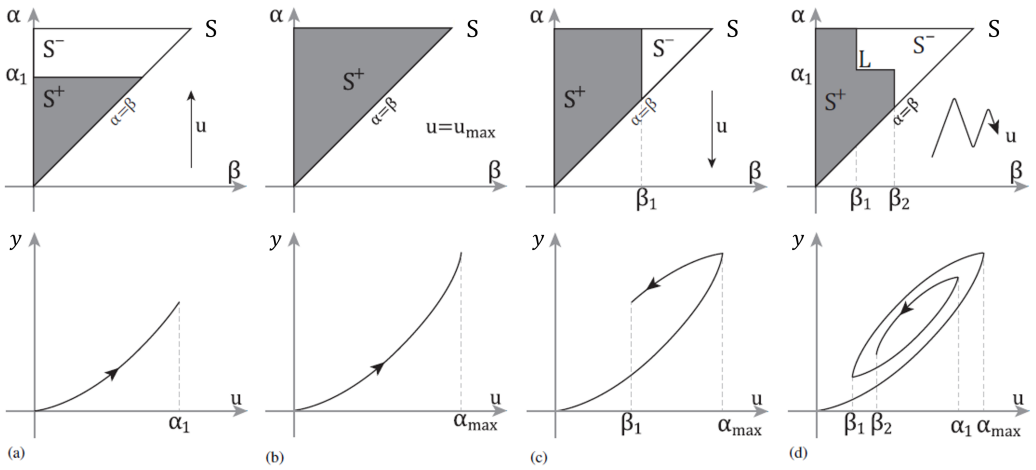

FIGURE 4.2.2: Example of how a hysteresis curve is obtained from the state of the Preisach triangle. Taken from [37], modified.

[5] For the sake of simplicity, the weight function $\mu(\beta, \alpha)$ is assumed to be constant in this example.

5 Setup and commissioning of a Michelson interferometer as an outreach experiment

The subject of this thesis is the construction and commissioning of a Michelson interferometer to demonstrate the principles of gravitational wave detection in outreach activities.

In physics, as in the other natural sciences, outreach activities are of great importance. The term outreach in this context encompasses activities whose primary goal is to promote the awareness and understanding of physics among a broader audience of non-experts (most often pupils) and to make physics tangible outside of university research. In addition to increasing general interest in physics, important benefits of outreach activities include sparking the interest and motivation of potential young scientists and providing accountability for the use of research funds. It is especially in still young fields of physics, which include gravitational wave astronomy, that outreach activities can reach their full potential. Out of this motivation, an experimental setup is developed with the aim to illustrate the complex principles of gravitational wave detection in a simplified and understandable way.

The setup constructed as part of this work is based on a Michelson interferometer with piezo-driven mirrors, the motion of which can be used to simulate the strain of an incident gravitational wave. The first part of this thesis concentrates on the construction of this experimental setup, and the challenges involved, such as the selection, adjustment and characterization of suitable components, seismic isolation and stabilization of the setup. The second part of the thesis focuses on characterizing and correcting the nonlinear expansion behavior of the piezoelectric actuators used to control the mirrors through application of the mathematical Preisach hysteresis model, as well as applying the corrections to a gravitational wave signal. The effective use of the setup in outreach activities is beyond the scope of this work and will be left to future researchers and students.

5.1 Setup and function of the Michelson interferometer

The core of this work is the constructed experimental setup based on a Michelson interferometer. In the following sections the technical details of the final version of the setup as well as its adjustment and operation will be explained.

5.1.1 Setup and technical realization

The final version of the experimental setup is shown schematically in fig. 5.1.1. A photo of the setup is included in fig. 5.1.2. In the following, the choice and function of the individual components of the interferometer will be discussed. A detailed list of all components with model designations of the individual components is provided in table 7.0.1.

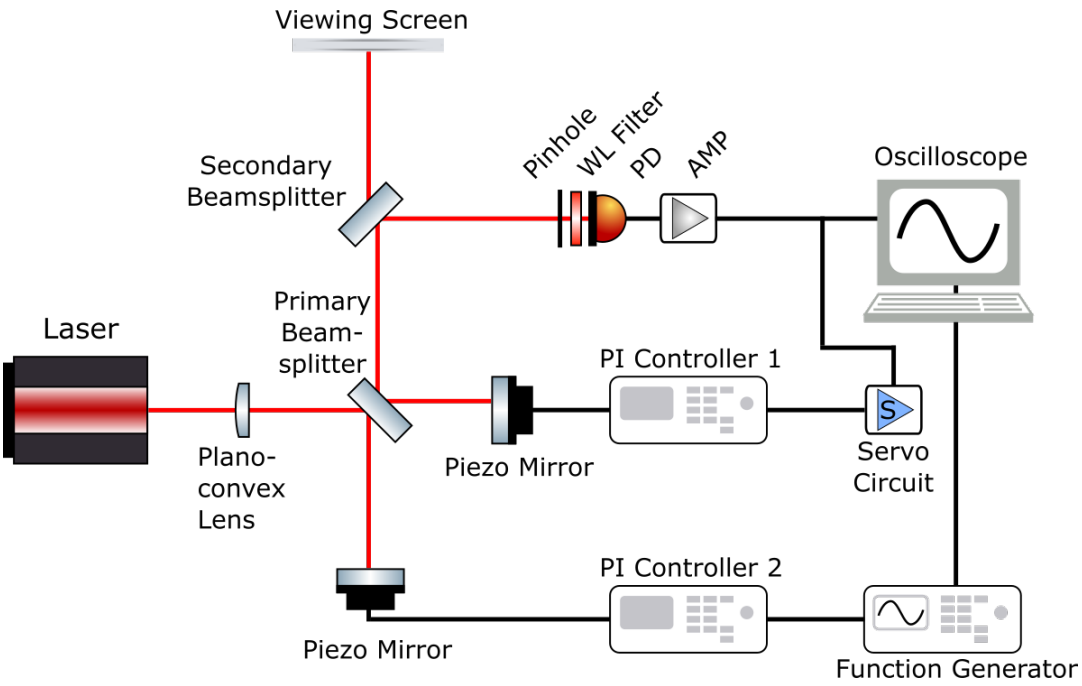

FIGURE 5.1.1: Schematic representation of the experimental setup. The red lines represent the laser light, the black lines denote the cables. For the sake of clarity, the laser beams are shown as lines of constant width. In the actual setup, the light beams are divergent due to the plano-convex lens. "WL Filter" refers to the optical bandpass filter, "PD" to the photodiode, and "AMP" to the transimpedance amplifier connected to it. The "PI Controllers" are voltage sources designed for the use with piezoelectric stack actuators. Illustration created using [38].

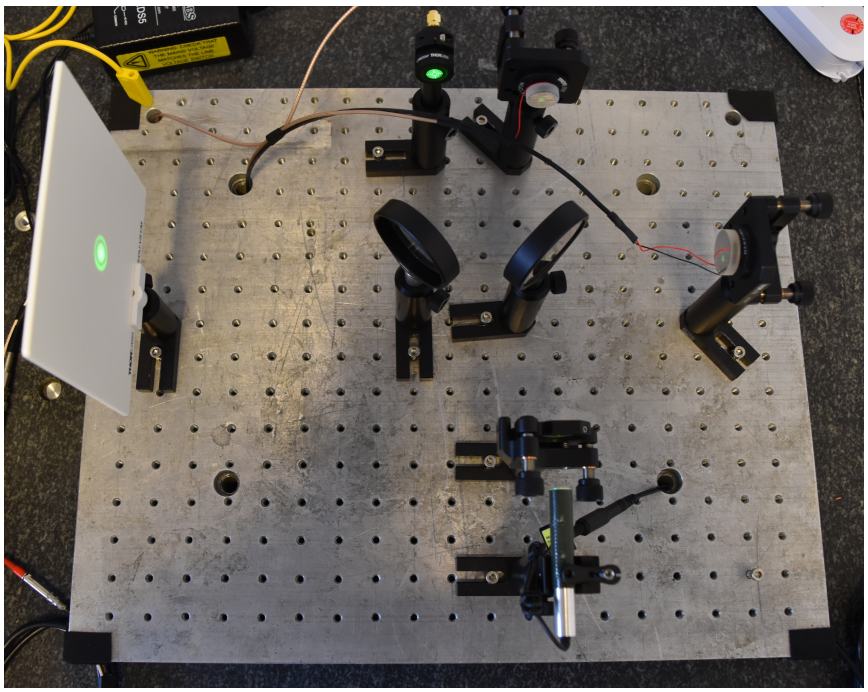

FIGURE 5.1.2: Basic experimental setup without control electronics and acrylic cover. Rotated by 90 degrees compared to the schematic in fig. 5.1.1.

The light source of the interferometer is a diode-pumped solid state (DPSS) laser with a wavelength of 532 nm, which emits quasi unpolarized light [39] in a collimated beam (divergence 0.5 mrad) of about 3.5 mm diameter. A model with a power of 0.87 mW was selected to produce a sufficiently strong signal while remaining within laser safety class 2. The use of a more powerful laser would improve the interference fringe visibility of the setup, but would not be viable for an outreach experiment as it is potentially dangerous.

The light beam emitted by the laser is expanded by a 1-inch plano-convex lens with a focal length of $f = 100\,\text{mm}$. The lens is oriented with the convex side facing the laser to reduce spherical aberration. Spherical aberration describes the property of an optical lens that causes light rays incident parallel to the optical axis to have no uniform focal point after passing the lens. This effect is shown schematically for both possible lens orientations in fig. 5.1.3 - for a detailed explanation, the reader is referred to [20, pp. 509]. The use of the plano-convex lens is a key design element, since it enables the observation of a circular fringe pattern (see section 3.1). The size of the fringe pattern can be controlled by moving the plano-convex lens in the optical path. It was found that a larger fringe pattern simplifies adjustments and observations on the screen.

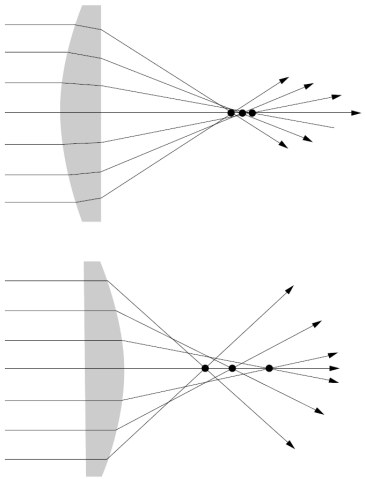

FIGURE 5.1.3: Effect of spherical aberration for a plano-convex lens. The aberration is less when the light rays are incident on the convex side of the lens. Taken from [20, p. 512].

The expanded light beam then hits the primary beamsplitter at an angle of 45 degrees. The beamsplitter has a reflection to transmission ratio of 50 to 50 for unpolarized light in a wavelength range between 450 nm and 650 nm. A 2-inch model was chosen to ensure that it can also be used for light beams with greater divergence and at greater distances from the light source. This is relevant in the context of possible future extensions to the experimental setup, since the clear aperture of a 1-inch beamsplitter previously used in the setup was almost completely utilized.

The portions of the light reflected or transmitted by the beamsplitter are then incident on two mirrors at the ends of the interferometer arms, which serve as analogs to the test masses of a gravitational wave detector. The mirrors chosen were fused silica models with a broadband dielectric coating, which have a reflection coefficient of $R > 99\%$ in a broad wavelength range from 400 nm to 750 nm. This ensures the function of the interferometer even when using a different light source. For the two arms, two mirrors with the same coating but with different sizes of 1.0 inch and 0.7 inch (see figs. 5.1.4a and 5.1.4b) were chosen to investigate the stability of the mount and the behavior of the piezos for two different configurations.

A crucial feature of the experimental setup is the attachment of the mirrors to piezoelectric stack actuators (hereafter: piezos), the expansion of which can be regulated by applying a control voltage, allowing dynamic adjustment of the arm length (see chapter 4). The mirrors are glued directly to the piezo stacks using an epoxy adhesive. The stacks are attached to a metal plate using the same adhesive. The metal plate, in turn, is screwed into a kinematic mirror mount. This construction is shown in fig. 5.1.4c viewed from the side for the larger of the two mirrors. The piezo stacks used are fabricated from layered sheets of piezoelectric ceramic, and have a maximum displacement of 2.1 μm at a drive voltage of 150 V. This corresponds to about 3.9 times the laser wavelength λ. However, only about 1.4 μm ($\hat{=}2.6\lambda$) of this displacement can be used, since the voltage sources used only provide up to 100 V. However, this is not a limitation for the intended use of the interferometer. The reason for choosing this specific model was the large surface area of (10×10) mm, which is necessary

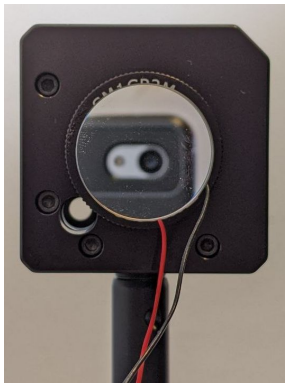

(A) Large mirror, mounted

(B) Small mirror, mounted

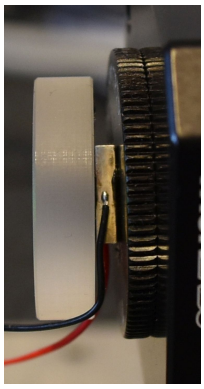

(C) Side view of the large mirror, glued onto a piezo stack

(D) Frontal view of the uncovered photodetector

(E) Frontal view of the covered photodetector, including a fringe pattern

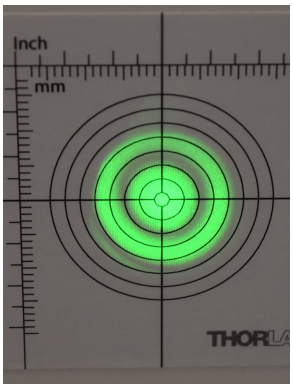

(F) Fringe pattern the viewing screen

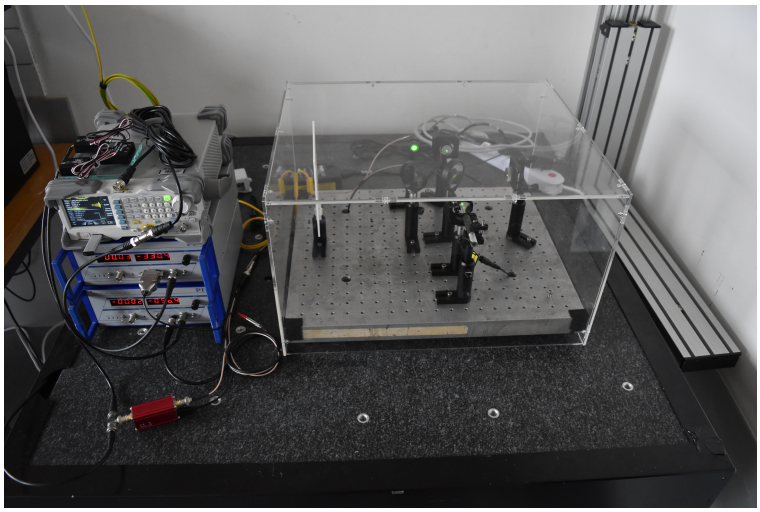

(G) Photo of the complete experimental setup. Visible is the breadboard with the interferometer, covered by an acrylic hood. The interferometer as well as the control and measuring equipment (to the left in the picture) are arranged on a granite plate.

FIGURE 5.1.4: Photos of various selected components as well as the complete experimental setup.

for attaching the mirrors. Mirrors with lower drive voltage ranges were also available from the same manufacturer, but all had an insufficient surface area.

The beams reflected by the mirrors are reunited at the primary beamsplitter, which directs the beams to the secondary beamsplitter with half their amplitude. The other half is returned to the laser. The secondary beamsplitter, which is identical to the primary beamsplitter, splits the light into two equal portions, one of which is projected onto an approximately (150×150) mm wide viewing screen of white polystyrene, while the other is projected onto the detector unit. Figure 5.1.4f shows a fringe pattern on the viewing screen, attached with a sticker containing a millimeter scale for estimating the sizes of the fringes.

The detector unit is installed in a 1 inch long lens tube. It contains a large-area silicon photodiode with a wavelength range of 350 nm to 1100 nm, a large active area of $13\,\mathrm{mm}^2$, and a rise/fall time of 10 ns. This diode was chosen to allow the use of a different light source and to simplify the adjustment of the setup compared to a diode with a smaller active area. To improve the signal to noise ratio, an optical bandpass filter with a passband of 532 ± 10 nm (FWHM) is installed in front of the photodiode. Since the bandpass filter is matched to the wavelength of the laser, it must be changed when a different light source is used. To measure only the intensity of the center fringe of the circular fringe pattern, for which the plane-wave approximation holds, an end cap with a 1 mm open aperture is placed in front of the lens tube. The end cap features concentric circles printed on it which serve as an alignment help. The frontal view of the uncovered detector with an unobstructed view of the wavelength filter is included in fig. 5.1.4d. The detector equipped with the pinhole is shown in fig. 5.1.4e.

All components are mounted on a $(41 \times 50 \times 4)$ cm aluminum breadboard with a weight of approximately 22 kg. Both mirrors are mounted at a distance of 12.5 cm from the primary beamsplitter. Since voltages of over 100 V are used in the setup, it has proven useful to fit the breadboard with a grounding cable as a protection against static electricity. Lens, beamsplitter, detector unit and screen are mounted on rigid mounts, which allow manual height adjustment and rotation around a vertical axis. The piezo-driven mirrors are additionally mounted on kinematic mirror mounts, which can be tilted around two axes using two adjuster screws. This allows for the required fine adjustment. For seismic isolation, the breadboard is equipped with four feet made of a viscoelastic urethane polymer, and is placed on a table made of a granite slab with a mass of about 40 kg. The mass of the entire table, which also contains solid wood and aluminum, is estimated[6] at about 100 kg. For thermal stabilization and to reduce the influence of moving air, the interferometer is fitted with a custom-made cuboid acrylic hood. A photograph of the complete setup, showing all mentioned components, is included in fig. 5.1.4g.

In addition to the optical components, other electronics are required to operate the interferometer. The piezo driven mirrors are controlled by two piezo controllers, which are custom designed voltage sources for the operation with piezo actuators. Their maximum output voltage is 100 V. The voltage sources can be regulated by input of a control voltage, which is amplified by a factor of 10 and passed on to the piezo. The voltage sources are equipped with interfaces for the connection to strain sensors, which are attached to certain piezos. This would allow real-time correction of piezo nonlinearities like hysteresis and creep, which is referred to as “closed loop operation”. Due to the simplicity and flexibility regarding the hardware used, the piezos were operated without sensors and feedback control for the purpose of this work. This is called “open loop operation”. Nevertheless, modifications for “closed loop operation” are possible in the future to further improve the precision of the interferometer.

[6]The masses of the granite slab and table were estimated based on the dimensions and known densities of the material - an exact value is not known because no available scale could record the weight of the table.

The photodiode is connected to a transimpedance amplifier with a gain of 100 kV/A. This converts the photodiode's output current into a voltage that can be processed by common instruments such as an oscilloscope, as is used in the setup. Additionally, converting the photocurrent to a voltage is much less expensive than the hardware required to measure currents in the μA to mA range at a high sampling rate.

The interferometer arm length is controlled by a function generator, that allows the display of custom voltage signals with high accuracy. The function generator can be connected to either of the piezo controllers. Additionally, the arm length can be varied by hand using the piezo controllers' inbuilt potentiometers.

For stabilization of the interferometer and for automated adjustment to an interference minimum, a servo circuit was designed. It consists of a voltage input module, a voltage output module, and a control hub, which is connected to the laboratory PC. The voltage input module is connected to the photodiode amplifier. The voltage read out is passed on to the hub and then to the laboratory PC. Using an algorithm created for this purpose, the PC determines from the brightness at the interferometer output the required displacement of the interferometer arm to get closer to a local interferometer minimum. The displacement is converted into a voltage and passed on from the PC to the piezo controller via the hub and voltage output module. For the adjustment process the interferometer arm is used, which is not connected to the function generator, because stabilization and signal display are mutually exclusive. The exact function of the servo circuit will be discussed in section 5.2.3.

In summary, an experimental setup was created which is suitable as an outreach experiment due to its visual component (displaying a fringe pattern on the screen) without sacrificing the ability to quantitatively analyze what is seen. This is achieved by using a second beamsplitter. In addition, the operation principle of a gravitational wave detector can be mimicked in a sensible manner by adjusting the interferometer to its dark fringe through the servo circuit on one arm, and then displaying a gravitational wave signal by moving the piezo on the other arm. The general working principle of a gravitational wave detector can thus be simulated without limiting the setup's outreach capabilities by implementing complicated techniques such as resonators, power recycling or signal recycling.

5.1.2 Alignment procedure for the interferometer

To ensure good functionality, the interferometer must be precisely aligned prior to operation. To that end, the components are installed and adjusted successively. First, the laser and the opposing mirror are installed. The mirror is aligned with its adjustment screws so that the light is reflected back into the laser. Next, the primary beamsplitter and the second mirror are installed. The beamsplitter is aligned so that the light hits the center of the second mirror. Both mirrors are readjusted so that the reflected light is centered back onto the laser. The observation screen is then installed. The two laser beams of the interferometer output should overlap completely on the screen. If this is not the case, the mirrors must be readjusted accordingly. Next, the plano-convex lens is installed. A fringe pattern should then be visible on the screen. If the fringes are not perfectly concentric, the mirrors adjustment must be corrected. Then the fringe pattern is shifted slightly horizontally by tilting the mirrors. This prevents the back reflection into the laser, which was previously arranged for convenience, as this can lead to unwanted disruptive optical effects. A very small tilt of about 1° is already sufficient. A stronger displacement would result in a wrong measurement of the piezos' expansion, since the tilt angle is very difficult to determine and to take into account mathematically. In the last step, the secondary beamsplitter is installed and the photodiode is positioned to collect the light reflected by it. The mirrors are not to be adjusted in this process so as not to interfere with the already completed alignment.

When using the interferometer over an extended time period, it was found useful to clean the optical components regularly with compressed air, and in the case of more severe contamination, with a lens paper and ethanol.

5.1.3 Basic principle of relative length measurements with the interferometer

Part of this work was to accurately measure the arm length change of the interferometer for the purpose of characterizing the behavior of the piezo actuators (see section 5.3). However, as is shown in the theoretical explanations in section 3.1, a Michelson interferometer lacks the ability to determine the arm lengths as an absolute value without external measuring devices. Yet, the relative arm length change can be determined from the sequence of irradiance maxima and minima at the interferometer output. This procedure will now be explained.

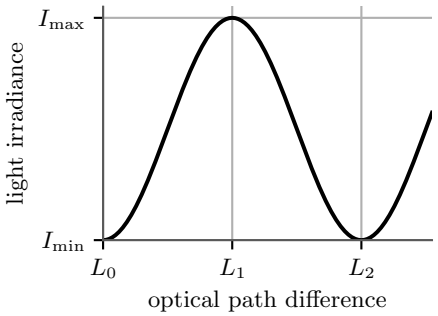

FIGURE 5.1.5: Exemplary behavior of the interferometer output under variation of the arm length. The marked extrema at L_0, L_1, L_2 are separated by distances of $\lambda/4$.

As discussed previously, the light intensity at the interferometer output depends on the cosine of the path difference of the interferometer arms (see eqs. (3.1.2) and (3.1.5)). This relation is plotted in fig. 5.1.5. The local extrema at L_0, L_1, L_2 have distances of $\lambda/4$ and intensities of I_{min} and I_{max}, respectively.

Since the cosine is equivalent to a phase-shifted sine, the rising and falling edges in fig. 5.1.5 can be described by modified sine functions. The rising edge is described by

$$I(L) = a \sin\left(\pi\left(\frac{L - L_0}{L_1 - L_0}\right) - \frac{\pi}{2}\right) + b, \tag{5.1.1}$$

while the falling edge is described by

$$I(L) = a \sin\left(\pi\left(\frac{L - L_1}{L_2 - L_1} - 1\right) - \frac{\pi}{2}\right) + b. \tag{5.1.2}$$

Here, the abbreviations

$$a := I_{\text{max}} - \frac{I_{\text{max}} + I_{\text{min}}}{2} \tag{5.1.3}$$

and

$$b := \frac{I_{\text{max}} + I_{\text{min}}}{2} \tag{5.1.4}$$

are used for amplitude and offset of the edge. The quantities $(L - L_0)/(L_1 - L_0)$ and $(L - L_1)/(L_2 - L_1)$ describe the relative position on the edge between 0 (first extremum)

and 1 (second extremum). By rearranging eqs. (5.1.1) and (5.1.2) one obtains the inverse functions

$$\frac{L - L_0}{L_1 - L_0} = \frac{1}{\pi}\left(\arcsin\left(\frac{I - b}{a}\right) + \frac{\pi}{2}\right) \tag{5.1.5}$$

and

$$\frac{L - L_1}{L_2 - L_1} = 1 - \frac{1}{\pi}\left(\arcsin\left(\frac{I - b}{a}\right) + \frac{\pi}{2}\right). \tag{5.1.6}$$

Thus, provided the maximum and minimum intensities I_{max} and I_{min} are known, the relative position on the edge, and therefore the optical path difference, can be determined from the intensity at the interferometer output. A disadvantage of the method is the ambiguity of the obtained results. Only the current position between the two nearest extrema can be determined, as the same light intensity is also assumed at the equivalent positions of all other edges.

The practical application of this method will now be discussed using an example measurement, conducted with the interferometer. For this purpose, the interferometer was first set to destructive interference using the servo circuit connected to the larger of the two mirrors. Subsequently, a voltage signal increasing linearly from 0 V to 100 V was then applied to the piezo mounted underneath the smaller of the two mirrors, and the light intensity at the interferometer output was recorded. To obtain standard deviations, the measurement was performed ten times. Input and output signals are shown in fig. 5.1.6a.

As to be expected on the basis of the manufacturer's specifications, the piezo expands by a distance corresponding to several laser wavelengths when the voltage is increased. This can be seen from the multiple sine-like peaks. Since the interferometer was set to destructive interference before conducting the measurement, it can be assumed that the voltage level before the first peak corresponds to the baseline expansion of the examined piezo. The voltage drop preceding the first peak is due to the fact that the measurement was repeated several times in succession. Since the piezo had enough time to reach its baseline displacement again, this does not need to be considered in the calculation of the displacement. The previously discussed calculations of the piezo's expansion were applied to the complete signal shown. For the values I_{max} and I_{min} the local extrema of the respective edges were assumed. The right and left edges of the signal, which cannot be assigned to any peak, were treated as independent edges. Here, the arithmetic mean of the maximum values of all peaks was used for I_{max}. The determined change in displacement of the piezo is shown in fig. 5.1.6b.

The relationship between the piezo's displacement and the applied voltage is linear in rough approximation. Unexpected, however, is the maximum expansion of (1860.90 ± 0.05) nm or $(3.498 \pm 0.001)\lambda$. Assuming that the approximate linearity is maintained over the complete voltage range of the piezo, i.e. up to 150 V, it was expected that at 100 V about $2/3$ of the maximum displacement specified by the manufacturer would be reached. This would correspond to only 1400 nm. There are several possible reasons for this. For one, the manufacturer states that production related differences of up to 15% exist between all manufactured piezos [40]. Furthermore, according to the manufacturer, the displacement under load can be larger than the free stroke displacement. However, the load specified by the manufacturer to achieve maximum displacement is 1600 N, several orders of magnitude

greater than the load caused by the mounted mirror. One further possible cause for the too high displacement is an improper alignment of the surface of the piezo-mounted mirror with respect to the beam path of the interferometer. A sufficiently strong misalignment for this is found to be unlikely though. A combination of the discussed possible reasons is assumed to be the most realistic reason for the unexpectedly large displacement.

Another important observation can be made regarding the uncertainties of the calculated displacement. These turn out to be disproportionately large at the transition points between two edges (i.e. at integer multiples of $\lambda/4$), as shown exemplarily for $\Delta L = 3\lambda$ in the zoomed-in section of fig. 5.1.6b. The reason for this is that the values of I near the local extrema naturally are very close to the boundaries of the domain of the inverse functions given by eqs. (5.1.5) and (5.1.6). Since the derivatives of the inverse functions diverge here, the standard deviations are greatly magnified by Gaussian error propagation. However, no negative influence of these mathematical artifacts on the quality of the results is found.

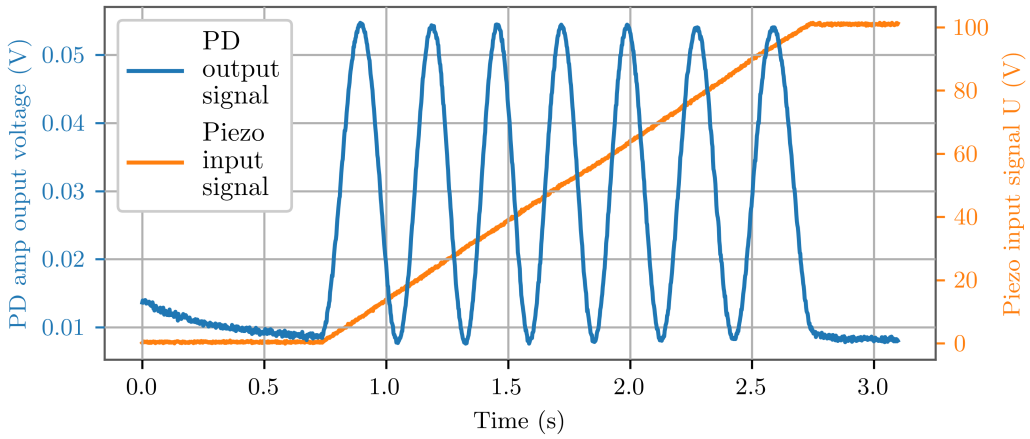

(A) Response of the piezo of the smaller of the two mirrors to a linearly increasing voltage signal in the range from 0 V to 100 V. Uncertainties smaller than symbol size.

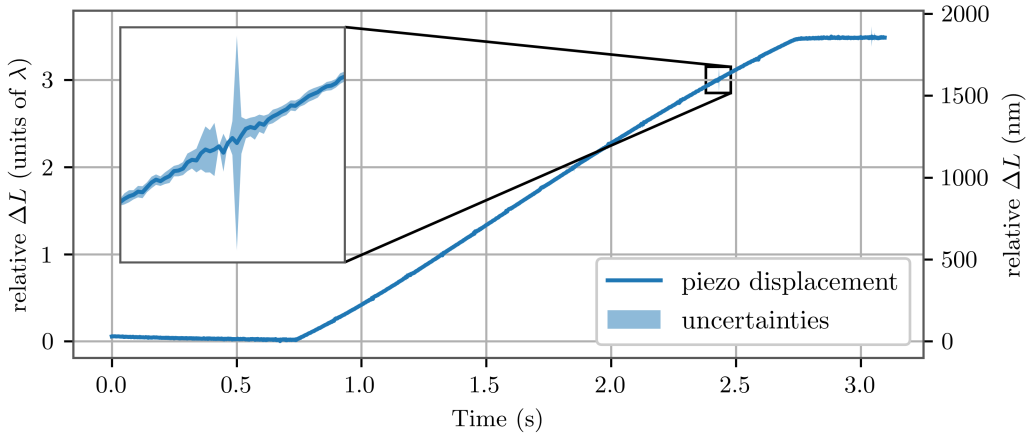

(B) Displacement of the piezo as a function of time calculated from the signal shown in (A). The zoomed area exemplarily shows the strong fluctuation of the calculated standard deviations around the transition points between two edges.

FIGURE 5.1.6: Demonstration of the piezo displacement calculation on the basis of the interferometer output. (A): Signal at the interferometer output when applying a linearly increasing voltage. (B): Displacement calculated from the output in (A).

5.2 Characterization and stabilization of the Interferometer

In the following sections, the performance of the interferometer will be analyzed and characterized. First, the effectiveness of the measures taken to decouple the interferometer from seismic vibrations and vibrations of the surrounding air is analyzed. Furthermore, the contrast of the interference pattern is studied with respect to the relevant optical components. Finally, the performance of the servo circuit used to adjust the interferometer to destructive interference is being reviewed.

5.2.1 Effectiveness of the vibration reduction measures

To achieve good stability and performance of the experimental setup, both when used as an outreach experiment and when performing measurements for testing and characterization purposes in this thesis, the setup was isolated from vibrations of the laboratory floor, such as those caused by the seismic background, as explained in section 5.1.1.

To check the effect of the measures taken, a vibration measurement was carried out. For this purpose, two seismometers[7] were placed on the test setup. One seismometer was placed directly on the breadboard (the beamsplitters were removed for this purpose), while the other was placed under the table on the lab floor as a reference (see fig. 5.2.1). To obtain representative results, a continuous measurement was performed over five days. On day 1, the setup was assembled, with the acrylic cover not attached. Day 2 was used entirely (over 24 continuous hours) as a measurement period. On day 3, the acrylic cover was attached over the breadboard. Day 4 was used entirely (over 24 continuous hours) as another measurement period. On day 5, the seismometers were removed from the setup. In the following discussions, the measurement periods of day 2 and day 4 will be compared. The remaining days are not usable for analyses, since here the setup was interacted with. It is assumed that there is good comparability between days 2 and 4, since both were regular working days (Tuesday and Thursday) without any unusual events.

The results of the vibration measurements are shown in fig. 5.2.2a as mean values of the measured power spectral densities (PSDs), while fig. 5.2.2b shows the difference between the measurement on the breadboard and the reference measurement under the table for both measurement periods. The power spectral density describes how the power of a measured signal is distributed over the different frequencies. Power here describes the square of the amplitude of the measurement signal. The quantity measured by the seismometers is the

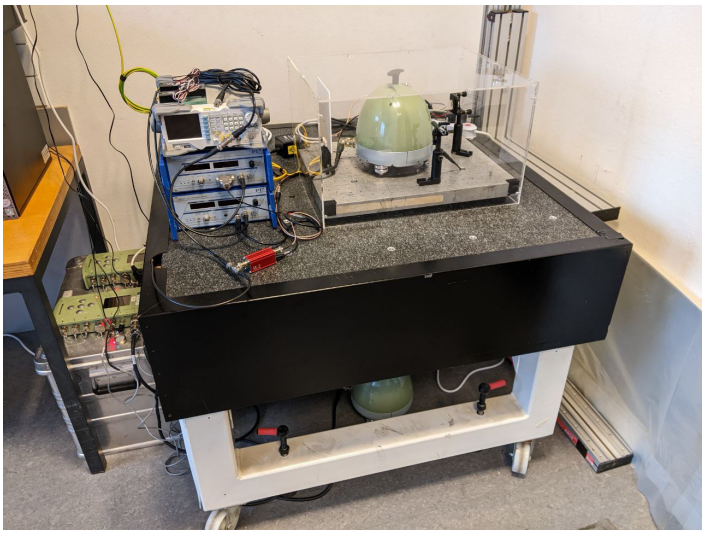

FIGURE 5.2.1: Setup of the vibration measurement. Clearly visible are the two seismometers, one on the breadboard, the other under the table. The beamsplitters and the plano-convex lens were removed to make room for the seismometer. The data loggers are located on the silver metal box to the left of the table.

[7] Nanometrics Trillium 120 PA, connected to loggers of type Nanometrics Taurus

ground acceleration (in $\mathrm{m/s^2}$), therefore the power spectral density has the unit $(\mathrm{m/s^2})^2/\mathrm{Hz}$. The data in decibels contained in the fig. 5.2.2a refers to a reference value of $1\,(\mathrm{m/s^2})^2/\mathrm{Hz}$.[8]

Considering the results, a general difference between the two measurement periods is apparent: during the first day of measurement (Tuesday), the vibration amplitude of both seismometers is higher throughout most of the frequency range than on the second day of

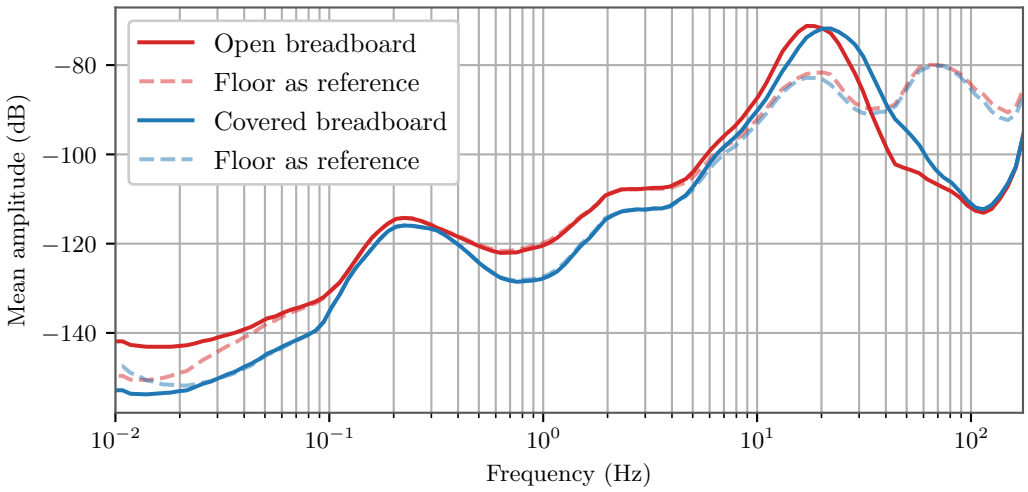

(A) The power spectral densities of the two different measurement periods in decibels. Measurement period 1, in which the breadboard was used open, is shown in red. Measurement period 2, with the acrylic hood attached, is shown in blue. Solid lines refer to the seismometer on the breadboard, dashed lines to the reference seismometer on the floor of the laboratory. Uncertainties smaller than line width.

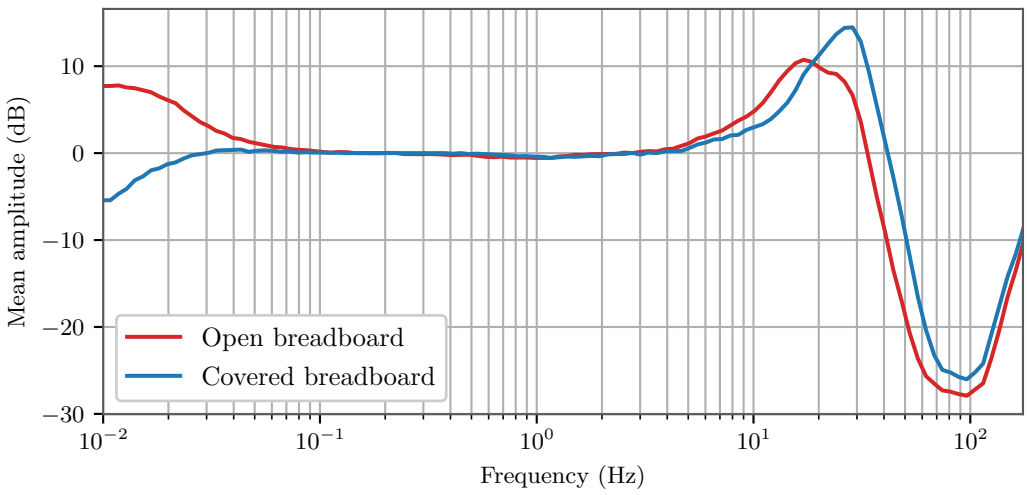

(B) Difference between the measured data of the seismometer on the breadboard and the reference seismometer on the ground. Coloring similar to (A). Uncertainties smaller than line width.

FIGURE 5.2.2: Results of the vibration measurement in two different configurations (with and without acrylic cover), each compared to a reference measurement (upper plot), as well as difference between measurement on the breadboard and the reference the floor (lower plot).

[8] For the understanding of the following discussions of the effectiveness of the noise mitigation measures, a detailed knowledge of how the PSDs are obtained is not necessary. A complete derivation is therefore beyond the scope of this thesis. The reader who is nevertheless interested is referred to the detailed mathematical derivation in [41].

measurement (Thursday). This is to be expected given the natural variations in environmental conditions, such as activity in the laboratory.

For both measurement periods however, there are clear differences between the measured vibrations on the breadboard and the vibrations on the ground: Above a frequency of about 33.5 Hz for the open breadboard and 41.6 Hz for the covered breadboard, respectively, the vibration amplitude on the breadboard is significantly lower than on the ground. The maximum attenuation is reached in both cases at approximately 95 Hz, and is slightly higher for the open breadboard with (-27.91 ± 0.01) dB than for the covered breadboard with (-26.0 ± 0.01) dB. The damping in this frequency range can most likely be attributed to the breadboard's vibration-reducing feet, the damping characteristics of which are shown in fig. 5.2.3. According to the manufacturer, when applied with a load of 5.5 kg per foot, which is a quarter of the weight of the breadboard and the mounted components, vibrations in frequency ranges greater than 40 Hz are reduced by over 80%. This agrees well with the obtained results.

Considering frequencies lower than 33.5 Hz for the open breadboard or 44.6 Hz for the covered breadboard, however, it is noticeable that the amplitude of the vibrations on the breadboard is higher than on the floor. This is the case for frequencies down to approximately 3 Hz. This unwanted amplification is more pronounced on the covered breadboard with (14.47 ± 0.01) dB at 28.6 Hz than on the open breadboard. Here, the amplification of the vibrations is (10.74 ± 0.01) dB at 17.1 Hz. A plausible hypothesis is that the system of table, feet and breadboard goes into resonance at these frequencies. However, since no negative effects on the stability of the setup and the quality of the measurement results could be detected during normal use of the interferometer, no further investigation of the cause was carried out.

For medium frequencies between 0.1 Hz and approximately 3 Hz, no significant difference between the vibration amplitude on the breadboard and on the floor is measured. This applies to both measurement periods.

At frequencies below 0.1 Hz, the vibration amplitude measured on the floor deviates from the vibration amplitude measured on the breadboard for both measurement periods. For the first measurement period, the vibration measured on the breadboard is up to (7.74 ± 0.01) dB higher than on the ground, while for the second measurement period, the vibration on the breadboard is up to (5.42 ± 0.01) dB lower than on the ground. Here, a correlation with the coverage of the breadboard by the acrylic hood, which was only attached on the third day, can be identified. However, the hypothesis that the acrylic hood reduces vibrations in frequency ranges around 10^{-2} Hz cannot be validated with certainty, since the seismometers were only available on two days.

In conclusion, the vibration damping seems to work to a limited extent, since frequencies around 100 Hz are significantly damped. Contrary to the expectations, however, frequencies

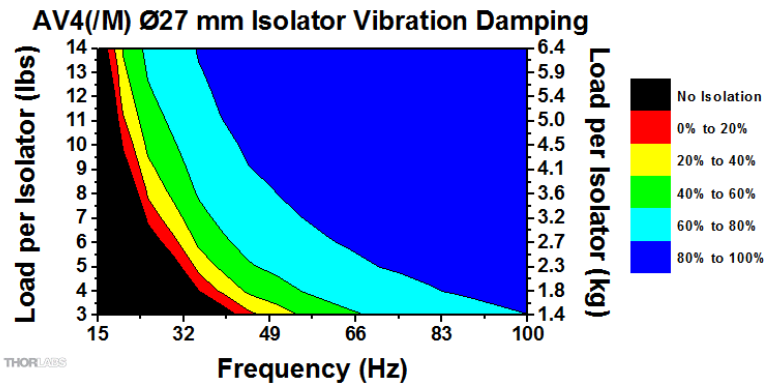

FIGURE 5.2.3: Vibration damping characteristics of the rubber feet of the breadboard as specified by the manufacturer, depending on the load per isolator and the frequency of the vibration. Source: [42].

around 30 to 40 Hz are amplified instead of being attenuated. Consequently, it must be decided, depending on the use case of the interferometer, whether it makes sense to use the vibration-reducing measures investigated. Comparing the open and closed configurations, the open breadboard appears to perform better overall. The unwanted amplification is lower and the desired damping higher than with the covered breadboard. The fact that oscillations with frequencies around 10^{-2} Hz are damped with the covered breadboard, while they are amplified with the open breadboard, can be neglected in the context of using the interferometer as an outreach experiment, since frequencies higher than $\mathcal{O}(1\,\text{Hz})$ are more relevant here. Since the desired damping of vibrations outweighs the undesired amplification at lower frequencies, it was decided to use the discussed measures without modification in the further course of the experiment.

5.2.2 Fringe visibility

One of the primary design goals of the experimental setup was to produce a fringe pattern that is both clearly visible on the observation screen and provides high contrast in measurements with the photodetector. To assess how well this design goal was achieved, a quantification of the optical quality of the fringe pattern is required. A suitable mathematical quantity is the so-called interferometric visibility, also referred to as "fringe visibility". This was first formulated by MICHELSON, and is a measure of the fluctuation of the irradiance around the mean value, relative to this mean value [20, pp. 1131]. Mathematically, the fringe visibility K is defined by

$$K = \frac{\frac{1}{2}\left(I_{\text{max}} - I_{\text{min}}\right)}{\frac{1}{2}\left(I_{\text{max}} + I_{\text{min}}\right)} = \frac{I_{\text{max}} - I_{\text{min}}}{I_{\text{max}} + I_{\text{min}}}, \tag{5.2.1}$$

where I_{max} and I_{min} describe the intensities in constructive and destructive interference, respectively. As can be easily seen, $0 \leq K \leq 1$ holds. A larger value of K is achieved at $I_{\text{max}} >> I_{\text{min}}$ and is thus desirable, while a lower value of K is achieved at $I_{\text{max}} \approx I_{\text{min}}$ and corresponds to poorer visibility.

To verify the achievement of the aforementioned design objective, the effects of each component on the fringe visibility were investigated. For this purpose, measurements of the interferometer output were performed in four optical configurations:

1. Open photodiode (no pinhole, no bandpass filter, no secondary beamsplitter)
2. Photodiode with pinhole (no bandpass filter, no secondary beamsplitter)
3. Photodiode with pinhole and bandpass filter (no secondary beamsplitter)
4. Complete configuration of photodiode with pinhole, bandpass filter and secondary beamsplitter.

After setting the interferometer to destructive interference using the servo circuit connected to the piezo of the larger mirror, triangular voltage signals with a period of 2 s and an amplitude of 100 V were applied to the piezo of the smaller mirror of the interferometer. All measurements were performed ten times and averaged to obtain standard deviations. To produce the same conditions as in future outreach applications, all measurements are taken with the room lights switched on. For the values I_{min} and I_{max} required to calculate K, the arithmetic means of all recorded local minima and maxima, respectively, were used. The results are illustrated in fig. 5.2.4.

When using the open photodiode without pinhole, the fringe visibility is $K = 0.3688 \pm 0.0013$. If the pinhole is installed, the visibility increases to $K = 0.7659 \pm 0.0027$. This increase by more than a factor of 2 results from the photodiode's large area of 13 mm^2. This is larger than the center fringe, resulting in automatic averaging over several fringes. Due to this unwanted averaging, the measured contrast is significantly smaller than the true mathematical contrast of the pattern. As expected, when the pinhole is used, the average signal intensity in terms of the output voltage is significantly lower with only (0.081 ± 0.001) V compared to $(0.65 \pm 0.01)\,V$ without the pinhole.

If in addition to the pinhole the optical bandpass filter is used, the maximum and minimum values of the output voltages drop to $(76 \pm 1)\%$ of the levels measured without the filter. This is consistent with the wavelength filter manufacturer's claims which state a minimum transmission at center wavelength of $T_{\text{min}} = 0.7$. Since the intensities of the maxima and minima decrease by the same percentage within the range of uncertainties, it can be concluded that the portions of light of other wavelengths reaching the photodetector are negligible in amplitude. Mathematically, this means that the use of the wavelength filter has minimal effect on the fringe visibility, which changes only from 0.7659 ± 0.0027 to 0.767 ± 0.010,

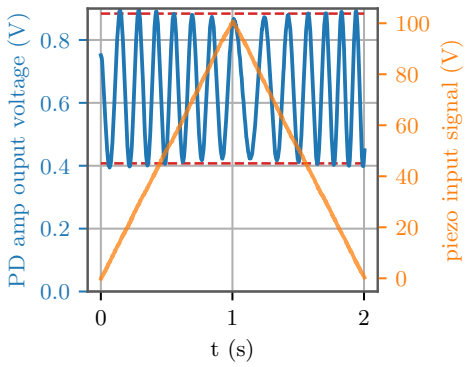

(A) Open photodiode (no pinhole, no bandpass filter, no secondary beamsplitter), $K = 0.3688 \pm 0.0013$.

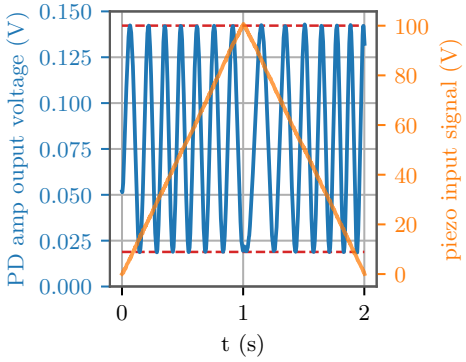

(B) Photodiode with pinhole (no bandpass filter, no secondary beamsplitter), $K = 0.7659 \pm 0.0027$.

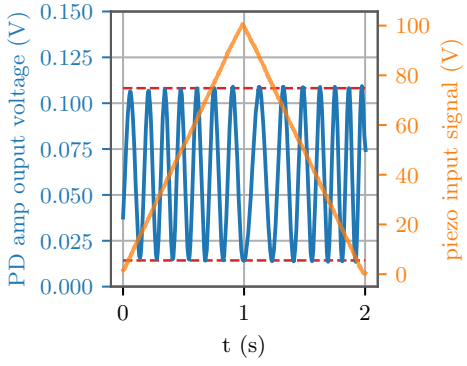

(C) Photodiode with pinhole and bandpass filter (no secondary beamsplitter), $K = 0.767 \pm 0.010$.

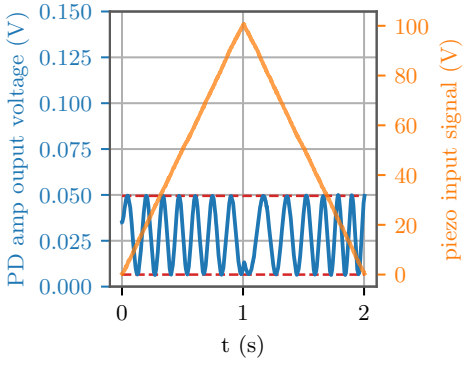

(D) Complete configuration of photodiode with pinhole, bandpass filter and secondary beamsplitter, $K = 0.766 \pm 0.007$.

FIGURE 5.2.4: Interferometer output (blue) in response to a triangular test signal (orange), for four different configurations of the optical components. The mean values of the local extrema (I_{max} and I_{min}) are plotted as dashed red lines.

i.e. in the range of measurement uncertainties. The use of the wavelength filter is nevertheless useful: if the setup is used in a different environment, the filter provides additional robustness even in the vicinity of potentially interfering light sources. Furthermore, it can be observed that the output voltage in the interference minima is noticeably above zero with about $(0.014 \pm 0.001)\,\mathrm{V}$ despite the use of the wavelength filter. Since the offset of the photodiode amplifier was adjusted to be 0 V (with noise levels of <1 mV) when the photodiode is completely darkened, it can be concluded that some laser light reaches the detector even in destructive interference. This is due to the limitations of manual adjustment of the interferometer, but is considered unproblematic in view of the intended use.

When the secondary beamsplitter is integrated into the setup, the intensities of the maxima and minima decrease equally by another $(46 \pm 0.1)\%$ compared to the previous configuration. This is fully in line with expectations, since the beamsplitter transmits 50% of the incident light to the observation screen. The remaining 4% loss may be due to possible tolerances in the manufacture of the beamsplitter, or due to unintended displacement of the photodiode during the installation of the beamsplitter. If the optical path length between the primary beamsplitter and the photodiode is extended, this results in a reduction of the light power per area due to the divergence of the light beam.

It can be concluded that the use of a wavelength filter and a second beamsplitter reduces the irradiance at the photodiode without noticeably changing the fringe visibility. Since this reduction in irradiance is not problematic within the intended use case, a setup is obtained that is less susceptible to changes in ambient lighting and provides better outreach capabilities by allowing simultaneous observation and measurement of the fringe pattern.

5.2.3 Adjusting for destructive interference and drift compensation using a servo control circuit

Before using the interferometer for measurements or displaying signals, it is necessary to adjust the interferometer for destructive interference. This is possible by manual adjustment of the potentiometer of one of the piezo controllers. However, since the manual adjustment requires a lot of fine-tuning and a time effort of several minutes, a servo circuit was created to automate this task.

The main component of the servo circuit is a control hub, which controls a voltage input module and a voltage output module (see fig. 5.2.5b). The voltage output module can provide voltages up to 4.2 V, and is connected to a piezo via one of the piezo controllers. It can be freely chosen which of the two piezos is connected to the servo circuit. This allows the servo circuit to control the arm length and influence the fringe pattern. The voltage output from the transimpedance amplifier is read by the voltage input module as a measure of the intensity of the center fringe, and fed back to the hub. The operating range of the voltage input module is $\pm 300\,\mathrm{mV}$, which is significantly larger than the range of possible output voltages. The control hub has no separate microprocessor, and is fully controlled by the laboratory PC. A schematic drawing of the servo circuit is included in fig. 5.2.5a. For a detailed listing of the components, see table 7.0.1.

To automatically find an interference minimum, a gradient descent algorithm is implemented. The algorithm computes the gradient of the photodetector output voltage as a function of the applied servo control voltage, and changes the control voltage in the opposite direction of the gradient. The procedure is performed iteratively, with the iteration rule

$$U_{\text{servo}}^{k+1} = U_{\text{servo}}^{k} - \alpha \frac{U_{\text{PD}}^{k} - U_{\text{PD}}^{k-1}}{U_{\text{servo}}^{k} - U_{\text{servo}}^{k-1}}. \tag{5.2.2}$$

Here U_{servo} is the voltage which is passed from the voltage output module to the piezo. U_{PD} describes the returned voltage of the amplifier of the photodetector. The superscripts mark the respective iteration. The fraction approximates the gradient via the difference quotient. The parameter α is a measure of the strength or aggressiveness of the control, and can be varied. The initial values used are the voltages U_{PD} at control voltages U_{servo} of 2.0 V and 2.1 V, respectively.

To ensure the proper operation of the servo circuit under any condition, several mechanisms have been implemented. On the one hand, the wide operating range of the voltage output module ensures that there is always more than one interference minimum within the control range. The maximum voltage of the voltage output module of 4.2 V corresponds to 42 V at the piezo after amplification. As can be seen in fig. 5.1.6, this corresponds to a change in length of the piezo by about 1.5λ, i.e. a sweep of three minima. Additional safeguards were integrated into the algorithm. If the control voltage leaves the permissible range, it is reset to the mean value of 2.1 V. If the output voltage U_{PD} of an iteration is equal to the last interation, which corresponds to a gradient of zero, $U_{\text{servo}}^{k+1} = U_{\text{servo}}^{k} + 0.001\,\text{V}$ is automatically set to avoid a division by zero and thus a stall condition.

To test the performance of the servo circuit, several series of measurements were performed. First, the time required by the servo circuit to adjust to an interference minimum was investigated. Specifically, the effects of the parameter α on this time were examined. For this purpose, the interferometer was manually adjusted for constructive interference in each case. Then the servo circuit was connected to the piezo of the larger mirror and the algorithm was started. The control voltage and photodiode voltage were recorded for 100 seconds and with the room lighting on. According to the hardware manufacturer's specifications, the uncertainties of U_{PD} were estimated to be $\pm 0.01\%$, and the uncertainties of U_{servo} were estimated to be ± 1 mV. Due to their small magnitude, they are negligible in the context of the measurements. Figure 5.2.6 contains the measurement results for the four tested values of α. In the plots, the output voltage of the amplifier is plotted against the control voltage applied to the piezo by the servo circuit. The scaling of the output voltage is chosen so that the first seconds, in which the output voltage is still at the pre-set maximum, are not visible, but the more relevant part for the performance of the servo circuit, in which the minimum is set and held, is better visible.

Considering fig. 5.2.6, several general observations can be made. For instance, for all values of α, the servo circuit succeeds in adjusting and holding a minimum with $U_{\text{PD}} < 8\,\text{mV}$ within the examined period of 100 seconds. An exact comparison of the brightness of the

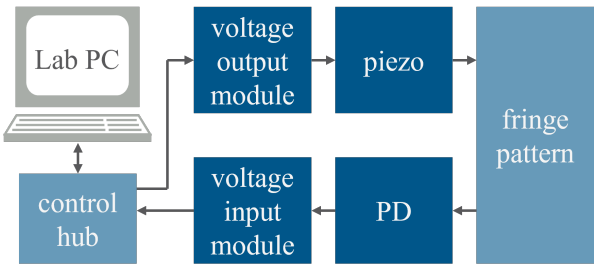

(A) Schematic diagram of the servo circuit structure, including the relevant components of the interferometer and Lab PC.

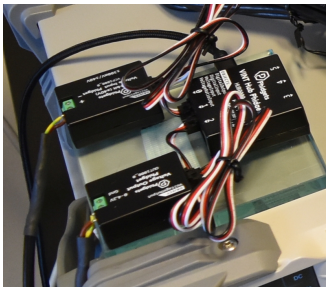

(B) Photo of the main components of the servo circuit. Right: Control hub. Top left: Voltage input module. Bottom left: Voltage output module.

FIGURE 5.2.5: Schematic diagram (left) and photo (right) of the servo circuit hardware.

set minima is not meaningful, since the brightness of the interference minima is subject to fluctuations due to changing environmental conditions. It is well recognizable that very similar features, some of them mirrored, appear in the control signal (shown in red) and the

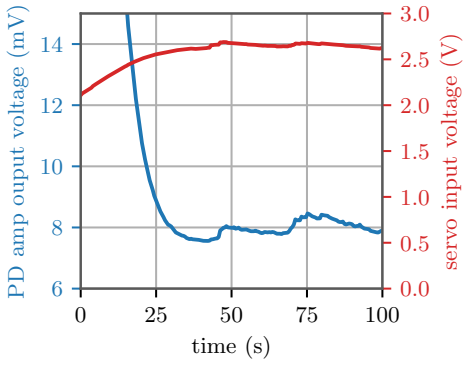

(A) $\alpha = 0.125$

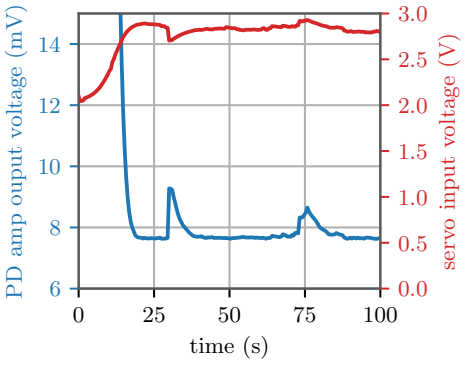

(B) $\alpha = 0.5$

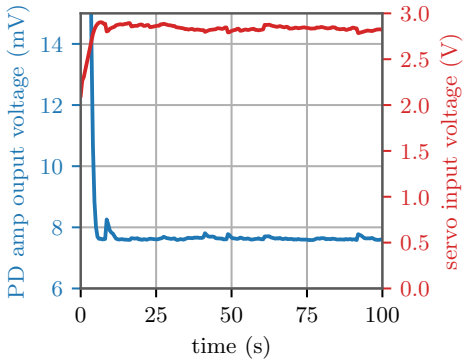

(C) $\alpha = 1.0$

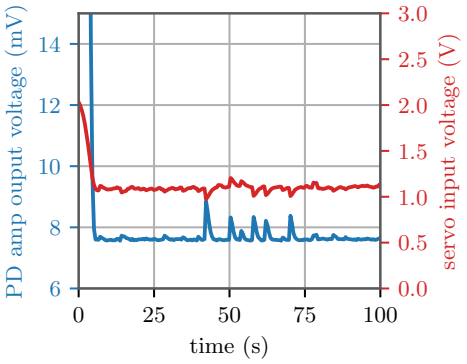

(D) $\alpha = 2.0$

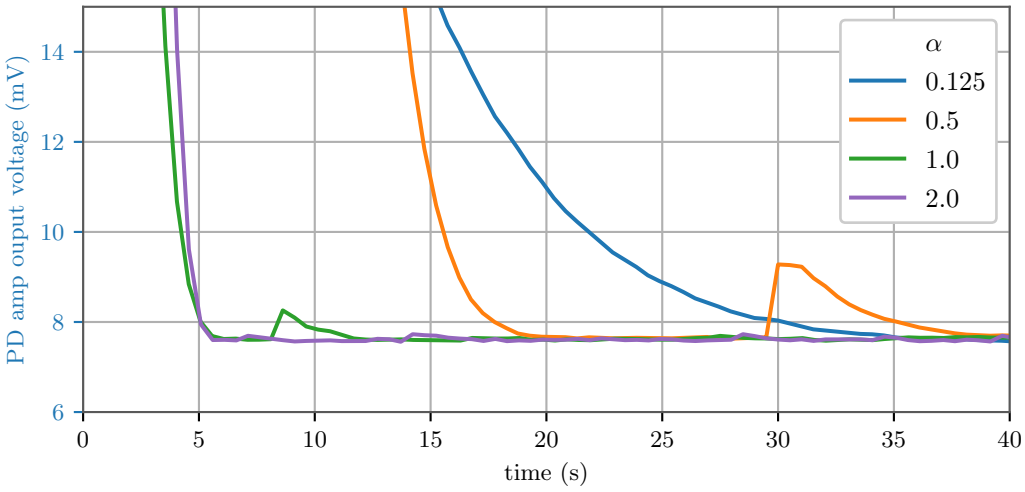

(E) Setting speed of an interference minimum for different values of α.

FIGURE 5.2.6: Performance of the servo circuit for different values of the parameter α. The control voltage U_{servo} is shown in red, the output voltage U_{PD} is shown in blue. Uncertainties smaller than line width.

output signal (shown in blue). This can be explained by the fact that the servo circuit reacts immediately to a change of the output, caused for example by a bump of the interferometer, with a corresponding change of the input.

For the various values of α differences are observed in the time needed to adjust an interference minimum. This can be seen particularly well in fig. 5.2.6e. For example, it is visible that the setting of the minimum is faster for higher α than for lower α. The threshold of an output signal of 8 mV is undercut for the first time at $\alpha = 0.125$ after (30.23 ± 0.03) s, at $\alpha = 0.5$ already after (17.64 ± 0.03) s , and at $\alpha = 1.0$ after (5.08 ± 0.03) s. At $\alpha = 2.0$ the performance does not improve noticeably, and the threshold is undercut after (5.07 ± 0.03) s. This is fully in line with expectations, since a larger value of alpha corresponds to a larger step size in the voltage. A more accurate quantitative analysis of the times needed by the servo circuit to adjust to a minimum is not conducted, since the exact time depends on many statistical processes, and can therefore vary significantly. For the sufficient optimization of the parameter α with regard to the intended use of the interferometer the performed qualitative analysis is sufficient.

Differences in the stability of the set minima are also visible. For example, at low $\alpha = 0.125$ it takes a long time of over 20 seconds to readjust the minimum if the adjustment is disturbed (see fig. 5.2.6a), for example by a bump of the interferometer. At $\alpha = 0.5$ this readjusting, in response to the two visible disturbances, is much faster (see fig. 5.2.6b). At $\alpha = 1.0$ the minimum is kept very stable (see fig. 5.2.6c). At $\alpha = 2.0$, several shorter disturbances are visible, to which the servo circuit responds immediately, as can be seen from the servo input voltage (see fig. 5.2.6d). Accurate interpretation of the results is challenging because it is not possible to control how often the interferometer leaves the minimum due to external perturbations. On the one hand, it is possible that more externally induced disturbances occurred during the measurement with $\alpha = 2.0$ than during the measurement with $\alpha = 1.0$. On the other hand, it cannot be excluded that the number of external disturbances is about the same, but the servo circuit with $\alpha = 2.0$ tends to overshoot, and the visible disturbances are, at least partly, caused by this.

Since there seems to be no advantage in the setting speed of the minimum at $\alpha = 2.0$ compared to $\alpha = 1.0$, and no clear conclusion can be drawn as to whether the servo circuit tends to overshoot at $\alpha = 2.0$, the parameter α is left at a value of 1.0 in the further course.

Besides the main purpose of adjusting an interference minimum, the servo circuit was also designed with the aim of keeping the interferometer stable in an interference minimum over a longer period of time. To test this functionality, three measurements were performed over 60 minutes each. During the first measurement, the interferometer was first adjusted to an interference minimum using the servo circuit. The servo circuit was then paused so that the voltage was maintained and not changed. The interferometer output was recorded for the next 60 minutes. The interferometer was operated without a cover. For comparison, the procedure was repeated with the acrylic cover attached. The results are illustrated in fig. 5.2.7a. In a third measurement, the interferometer was operated for 60 minutes without the acrylic cover, but with the servo circuit permanently active. The results of this measurement are illustrated in fig. 5.2.7b.

When operating the interferometer without cover and active servo circuit, strong fluctuations between (9.28 ± 0.01) mV and (55.53 ± 0.01) mV occur at the interferometer output within the measuring period. The range of these fluctuations corresponds to the complete range between an interferometer minimum and maximum, as seen in the results discussed in section 5.1.3. A possible cause is thought to be thermal drift, due to the change of expansion of the interferometer components (i.e. a change in arm length) in response to variations of the ambient temperature. Regardless of the suspected cause, due to the ambiguity of the interferometer output with respect to the arm length, no conclusion can be made as to whether

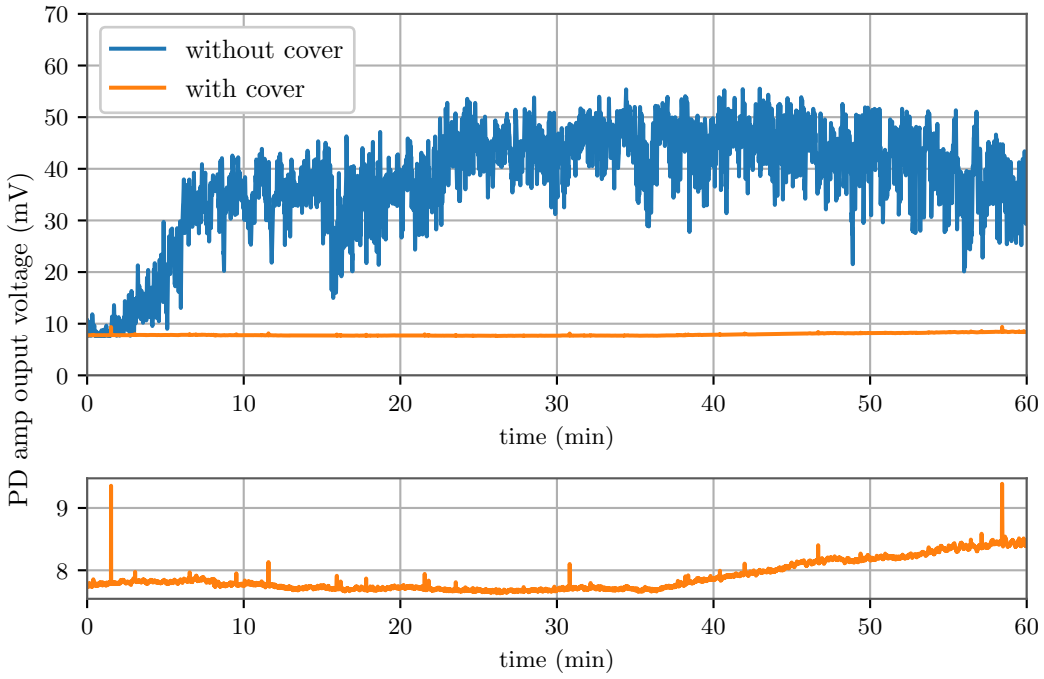

(A) **Upper plot:** Variation of the interferometer output over 60 minutes with the servo circuit halted. In blue without acrylic cover, in orange with cover. **Lower plot:** Zoom in on the measurement without cover.

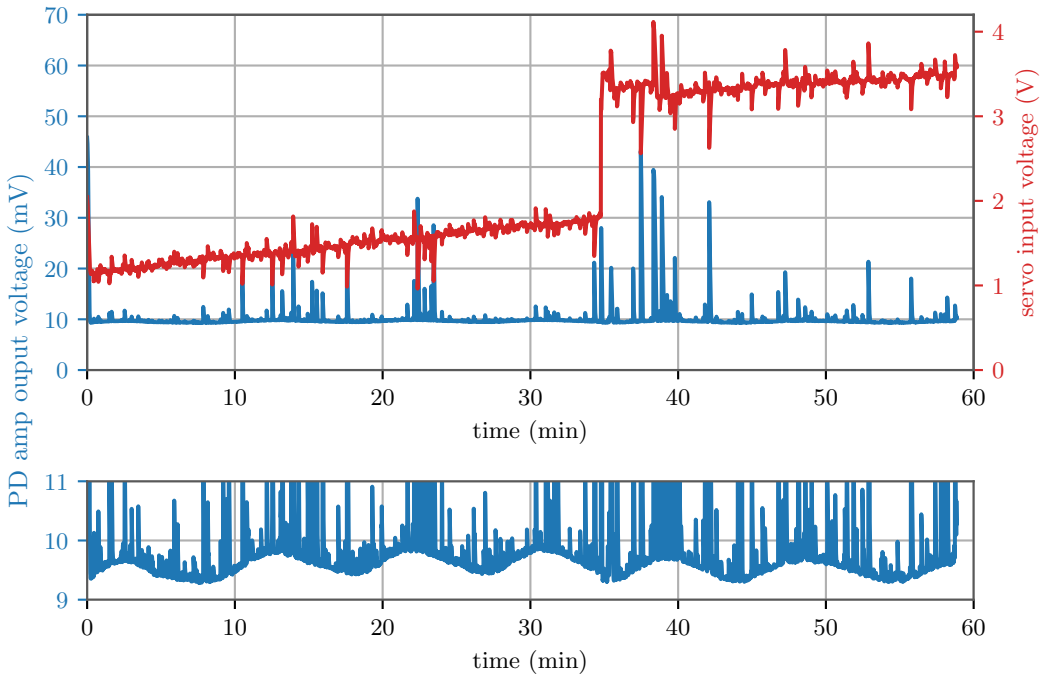

(B) **Upper plot:** Variation of the interferometer output over 60 minutes with active servo circuit and without acrylic cover. Interferometer output in blue, servo input voltage in red. **Lower plot:** Zoom in on the interferometer output.

FIGURE 5.2.7: Continuous measurement of the interferometer output. Comparison between enabled and disabled servo circuit and operation with and without acrylic cover.

the drift occurs in only one direction, or whether the sign of the drift varies. If the acrylic cover is placed on the interferometer, an enormous improvement of the signal quality can be observed. With the exception of two outliers, the output voltage remains permanently below 9 mV, and the fluctuations are several orders of magnitude smaller (see lower section of fig. 5.2.7a). Also for the output of the covered interferometer, a similar drift can be seen (bend starting at 36 min), which is also several orders of magnitude smaller. It can be concluded that the cover strongly reduces both the noise and the drift of the interferometer output. The reduction of the drift is consistent with the hypothesis that the drift is thermally induced, since a fixed temperature should be expected under the cover after warm-up. The reduction of the noise can possibly be attributed to the fact that sudden air movements and turbulences are reduced.

As is clearly visible in fig. 5.2.7b, the servo circuit is able to keep the interferometer output very stable compared to the measurement without servo circuit. The mean output voltage of (10.13 ± 0.01) mV is slightly higher than in the comparable measurement without servo circuit and with acrylic cover - here, an average of (7.91 ± 0.01) mV is found. This difference can be explained by slight adjustment changes, which naturally occur during every interaction with the hardware. In addition, fluctuations or outliers are clearly recognizable, but these occur in smaller numbers than in the comparative measurement without servo circuit. This can be explained by the fact that the servo circuit only has a limited ability to react to all fluctuations in a very short time. Another noticeable feature is the visible jump in the input at approximately 35 min. This most likely originates from the servo circuit being reset due to a stall condition or a leaving of the allowed voltage range, and can thus be considered as a normal function of the servo circuit. Unexpected, however, is the fluctuation of the interferometer output with an amplitude of about approximately (0.19 ± 0.03) mV and a period of approximately (550 ± 15) s, (values estimated from the local extrema of the five fully visible periods of the oscillation), which is visible in the lower section of fig. 5.2.7b. A similar fluctuation could not be observed during the measurement without servo circuit and installed acrylic hood. A possible hypothesis is a periodic fluctuation of the laser intensity, which caused the brightness of the interference minimum to vary. However, this reasoning raises the question of why the fluctuation was not observed in the comparative measurement without active servo circuit. Alternatively, it is hypothesized that the periodic fluctuation is an artifact caused by the gradient descent algorithm of the servo circuit, although the exact process which might cause the periodic fluctuation is unclear.

In view of the results, it can be concluded that the servo circuit adequately fulfills the intended task. With the parameter of $\alpha = 1$ found to be optimal, the adjustment of a minimum is significantly faster and more effective than by manual adjustment. In addition, the servo circuit can keep the interferometer stable over a longer period of time, which would also not be practical with manual adjustment. This result illustrates that good performance can be achieved even with relatively simple algorithms such as the chosen gradient descent method. Earlier approaches involving the software implementation of a full PID controller[9] were discarded as they proved to be more error-prone and unstable due to the higher complexity. No further time was invested in investigating the periodic fluctuation of the interferometer output observed in the last of the three measurements, since the amplitude of the fluctuation is very small compared to the amplitude of the signals to be displayed and measured on the interferometer, considering the intended field of use of the interferometer.

[9] A controller commonly used in control engineering that processes the difference between the actual and setpoint values using a proportional, an integral and a differential part.

5.3 Analysis of the behavior of the piezo actuators and correction of hysteresis

The control of the arm lengths of the interferometer is done by two piezo actuators, as already discussed in detail. In order to be able to display signals correctly using the piezos, as intended in the outreach experiment, detailed study of the response behavior and of the piezos is necessary. This also includes the correction of the hysteresis, which has already been mentioned in chapter 4.

5.3.1 Analysis of the step response of the piezos

When using the interferometer as an outreach experiment, signals of up to 10 seconds in duration are to be displayed on the interferometer. On this time scale, the response of the piezos is relevant.

To investigate the behavior of the piezos, the step response of both piezos was examined. For this purpose, the interferometer was first set to destructive interference using the servo circuit. Then, a periodic square-wave voltage signal with a period of 150 ms was applied to the piezo which was not connected to the servo circuit. The minimum voltage of the square wave signal was 0 V, while for the maximum voltage values from 5 V to 100 V were used. For each voltage selected, the positive and negative step responses, corresponding to the responses to the rising and falling edges of the periodic square wave signal, respectively, were recorded. To obtain standard deviations, all measurements were performed ten times. Based on the recorded signal from the photodetector, the changes in arm length (i.e. the change in extension of the piezo) were calculated using the procedure explained in detail in section 5.1.3. The brightnesses of the maxima and minima needed to calculate the extension were determined in a separate calibration measurement. The results are shown in fig. 5.3.1. The time of 0 ms in the figure refers to the trigger, which was coupled to the square wave signal.

Comparing the step responses of the piezo mounted under the large mirror with the piezo mounted under the small mirror reveals a clear difference in the displacements achieved at 100 V. This is fully in line with expectations.

The piezo installed under the large mirror reaches a displacement of (1460.09 ± 0.03) nm at 100 V at 75 ms. This agrees well with expectations, as the value is very close to 1400 nm, which is two thirds of the maximum displacement at 150 V specified by the manufacturer. It is not to be expected that the values match exactly, since the manufacturer specifies the piezo with “up to 15% of hysteresis” - this will be examined in detail in the next chapter.

The piezo of the small mirror reaches a displacement of (1919.9 ± 1.6) nm at 100 V at 75 ms, which is larger than expected, as already discussed in detail in section 5.1.3. The fact that the piezo of the large mirror, unlike this piezo, behaves as specified by the manufacturer supports the hypothesis that either a manufacturing anomaly occurred with this piezo, or that the wrong model of piezo was shipped (the distributor offers models with different displacements that are indistinguishable externally).

It is also noticeable that the measured displacement of (1919.9 ± 1.6) nm is about 3.2% larger than the displacement of (1860.90 ± 0.05) nm determined in the measurement described in section 5.1.3. This difference of 59 nm is several orders of magnitude larger than the measurement uncertainties determined based on the standard deviations of the repeated measurements. However, this does not contradict expectations: If the alignment of the interferometer is unintentionally changed during the interaction with the setup so that the mirror is no longer completely orthogonal to the beam path, the change in displacement of the piezo is measured incorrectly. This is not taken into account by the uncertainties. A change in the measured displacement of 3.2% between two measurements seems plausible.

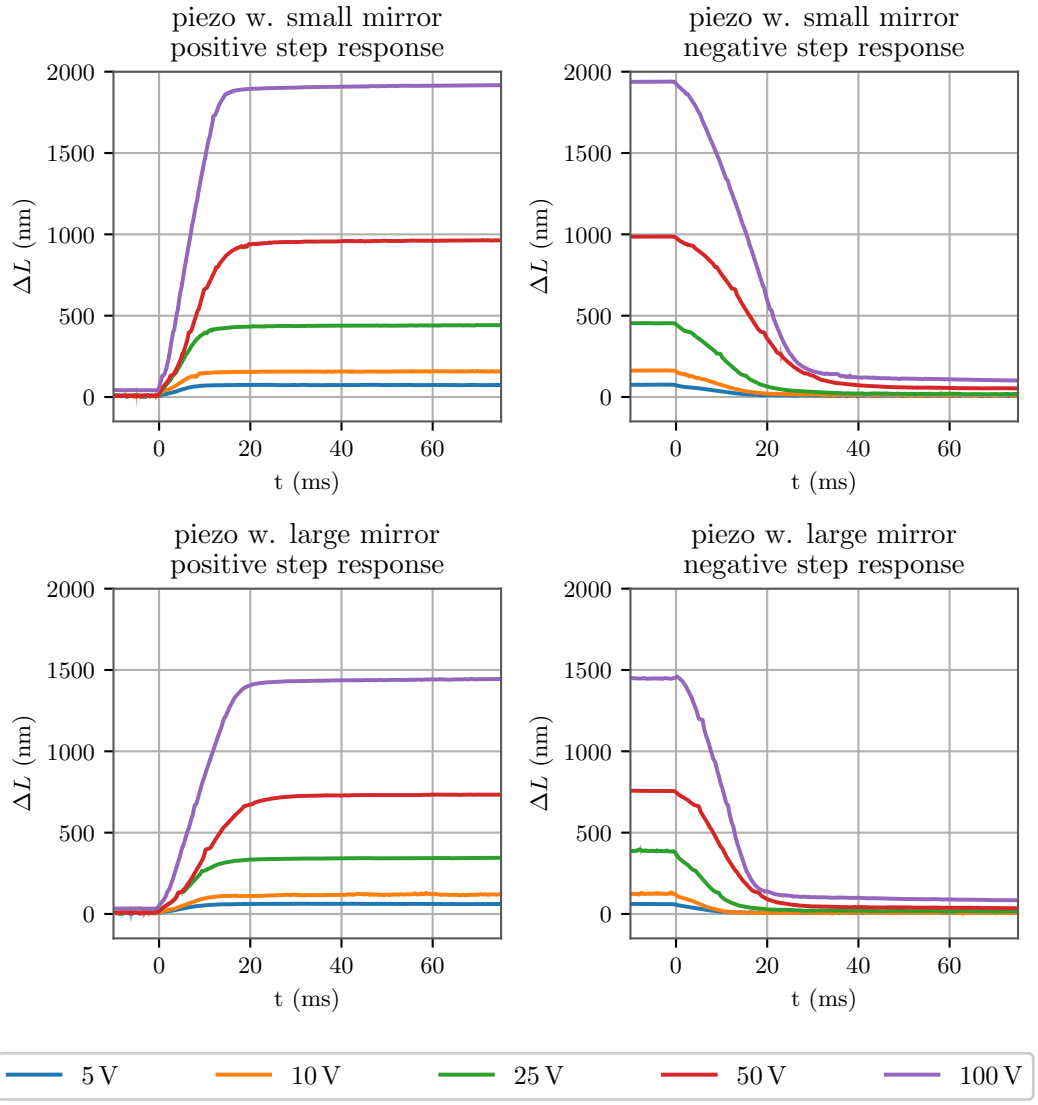

FIGURE 5.3.1: Step response of the two piezos for different voltages. **Upper row:** Piezo of the smaller mirror. **Bottom row:** Piezo of the larger mirror. The time of 0 ms refers to the timing of the trigger coupled to the applied square wave signal.

As a measure of the speed of response of the piezo to the applied voltage, the rise and fall times were determined. These were defined as the time periods in which the piezo expands from 10% to 90% of its measured maximum displacement, or falls from 90% to 10% of its maximum displacement. The maximum displacement used is the displacement at 75 ms after trigger (at 0 ms) in the case of rise time, and immediately before trigger in the case of fall time. The obtained rise and fall times are shown in fig. 5.3.2 as a function of the amplitude of the square wave signal.

As the plot shows, all piezos reach 90% of their "final" displacement (displacement at 75 ms) after less than 20 ms. A clear relationship between rise time and target voltage cannot be recognized. However, there is a tendency that the rise time for the piezo of the large as well as for the piezo of the small mirror increases monotonously starting from 5 V. At a target voltage of 50 V it is highest with (16.00 ± 0.16) ms and (12.80 ± 0.08) ms, respectively, but at 100 V it decreases again. Overall, the rise times are significantly larger than the "sub millisecond response time at zero load" advertised by the manufacturer. However, this is not

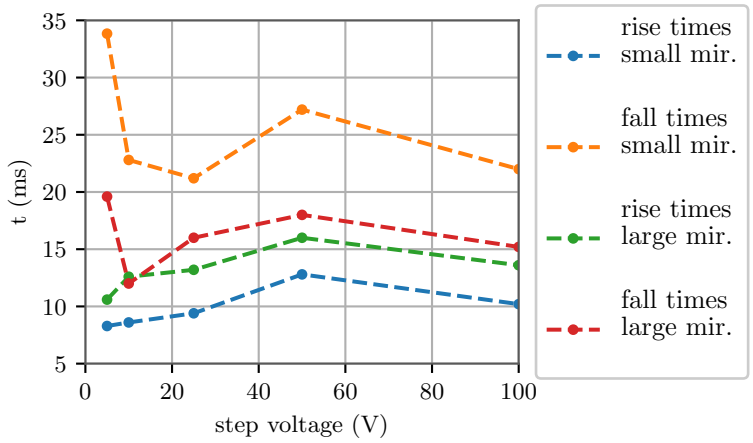

FIGURE 5.3.2: Comparison of rise and fall times for the piezos mounted beneath the large and small mirrors. Dashed line serves as a guide to the eye, and does not represent any data. Uncertainties smaller than symbol size.

necessarily a contradiction, since on the one hand the piezos are provided with a payload, and on the other hand the manufacturer does not give a definition of the response time. Presumably, the manufacturer's definition of the response time is related to the time between application of a voltage signal and the start of the expansion process.

A clear relationship between the fall time and the previous maximum stress can also not be observed. At 5 V the fall time is largest for both the piezo of the large and the piezo of the small mirror with (19.60 ± 0.12) ms and (33.84 ± 0.12) ms, respectively, and decreases sharply at 10 V. Analogous to the rise time, the fall time at a previous voltage of 50 V is larger than at the other voltages, with (18.00 ± 0.16) ms and (27.20 ± 0.16) ms, respectively, except for the fall time at 5 V. Besides, it is noticeable that the rise times are generally higher with the piezo of the larger mirror, while the fall times are lower with the piezo of the larger mirror than with the piezo of the smaller mirror. A reason for this is not known.

An interesting observation is also that the drop in displacement for both piezos when the voltage changes from 100 V to 0 V seems to have a slightly different shape compared to the shape of the displacement for other initial voltages (see fig. 5.3.1). The bend between 20 s and 40 s is more pronounced here. An exact reason for this behavior is not known. However, this effect only has to be taken into account when working with fast signals and high displacements, and is not relevant for the outreach experiment.

Finally, it can be concluded that the results obtained for the response time of the piezos are in line with theoretical expectations. For all voltages used and for both piezos, rise times of less than 100 ms were observed. This is consistent with the results of past research in which it was shown that piezos typically have a dynamic response in the first 100 ms after a voltage is applied, the shape of which varies depending on the individual piezo [43]. With respect to the intended use of the interferometer, i.e. the display of signals on the scale of several seconds, a rise time on the observed time scale is not problematic. Besides, when using the interferometer as an outreach experiment, continuous signals are to be displayed. Step signals represent a special case which is not relevant in this scenario.

Furthermore, it has to be mentioned that piezos in general do not only have a dynamic response in the timespan up to 100 ms, but also a so-called creep. This describes a displacement process which continues after the dynamic phase when a voltage is applied and which behaves logarithmically with time. According to the current state of research, this can be described by [43]

$$L(t) = L_0 \left[1 + \gamma \log_{10} \left(\frac{t}{0.1} \right) \right] \tag{5.3.1}$$

where L_0 is the displacement of the piezo at 0.1s and $0.01 < \gamma < 0.02$. Because of the creep, the choice of the time of 75 ms as a reference for maximum intensity of the signal, as used to calculate the rise and fall times, seems arbitrary. The value was taken because it is in a reasonable order of magnitude for the outreach experiment. However, the creep will not be investigated further in this work since it is not relevant on the time scales of interest for the outreach experiment. It is more relevant for nanopositioning tasks where, for example, a sample must be held at the same position for a long period of time, such as in a scanning tunneling microscope.

5.3.2 Hysteresis compensation using the Preisach model

Since in the outreach experiment the piezos will be used to mimic gravitational wave signals, it is necessary to fully understand the relationship between the applied voltage and the achieved displacement. The hysteresis behavior of the piezos is a constraint in this regard, as the relationship between voltage and displacement is ambiguous and dependent on the past of the system, as explained in chapter 4. To approach this problem, the hysteresis behavior of the piezos is characterized and compensated using the Preisach model.

For a first test of the hysteresis behavior, the response to a triangular signal with an amplitude of 100 V and a period of 2 s was measured for both piezos. To calculate the displacement from the interferometer output, the already discussed procedure was used. To obtain standard deviation, the responses were averaged over ten periods of the input signal. The results are illustrated in fig. 5.3.3.

Analogous to the previous measurements, it is observed that the overall displacement of the piezo mounted under the large mirror is less than that of the piezo mounted under the small mirror. As a measure of hysteresis, the relative difference in displacement between the ascending and descending branches at 50 V can be used. If this hysteresis measure is compared for both piezos, one obtains $(20.0 \pm 1.8)\%$ for the piezo of the large mirror and $(20.5 \pm 1.5)\%$ for the piezo of the small mirror. The relative magnitude of hysteresis thus agrees within the range of uncertainties for both piezos. The manufacturer specifies a "hysteresis of <15%" for the piezos used [40]. This is about 5% smaller than the hysteresis observed. However, the manufacturers specifications apply to an operation range of up to

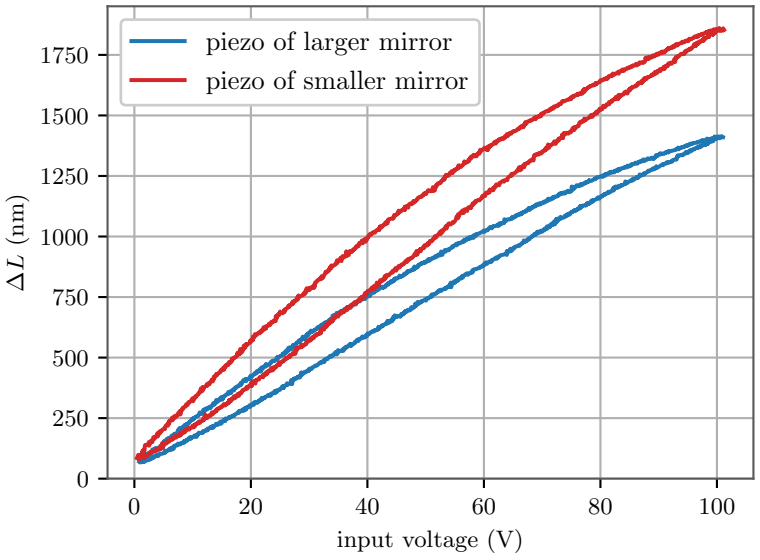

FIGURE 5.3.3: Comparison of the hysteresis of both piezos. In red the displacement of the piezo of the smaller mirror, in blue the displacement of the piezo of the larger mirror. Uncertainties smaller than symbol size.

150 V, where the relative amount of hysteresis may be different. Furthermore, the manufacturer provides no mathematical definition of its measure for hysteresis.

In the following, it will be investigated how the hysteresis can be compensated with the help of the Preisach model. First, the method used to fit the Preisach model to the hysteresis behavior of the tested piezo will be introduced. Subsequently, the inversion of the fitted Preisach model for precise control of the piezo will be discussed. The studies conducted for this purpose were performed using only the piezo of the larger mirror since it has the lower displacement at 100 V, which simplifies data processing and accurate driving of the piezo (the interferometer output spans less extrema overall, and the change in displacement per volt is smaller). Performing the studies with the other piezo would yield no additional benefit, considering the intended use of the interferometer.

Fit and inversion of the Preisach model

For the numeric implementation of the Preisach model, the Preisach triangle has to be discretized. For this purpose, a discretization level n_h is chosen, and the input u of the system is divided into $n_h + 1$ levels. The Preisach triangle is thus divided into

$$n_q = \frac{n_h \left(n_h + 1\right)}{2} \tag{5.3.2}$$

cells, each corresponding to a hysteron of the model. This discretization is shown in fig. 5.3.4a as an example for a discretization level of $n_h = 4$. The weight function $\mu\left(\beta, \alpha\right)$ is to be understood as center weights, so that an individual weight is assigned to each hysteron.

The main challenge is to identify the weight function $\mu\left(\beta, \alpha\right)$, which describes the studied system. To identify the weight function, a periodic input signal ("probe signal") with increasing amplitude is used. This signal has n_h peaks to cover all input levels of the system. The probe signal, which would be needed to identify the weight function of the system shown in fig. 5.3.4a, is shown in fig. 5.3.4b. The input signal causes each hysteron in each row of the triangle to be successively activated individually. For example, if the first peak is fed to the system, the single hysteron of the first row is turned on and off again. If the second peak is sent to the system, after the lowest hysteron, the second lowest row of hysterons is also activated. When the voltage drops, it is successively deactivated again. In this way, information about each hysteron can be obtained.

The response $y(t)$ of the system to the probe signal $u(t)$ is the first part of the information needed to find the weight function of the system. The second component is the information about which hysterons

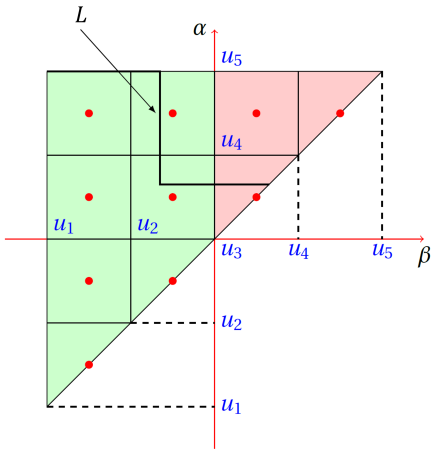

(A) Discretized Preisach triangle with $n_h = 4$. This corresponds to 5 input levels (ranging from u_1 to u_5) and $n_q = 10$ total hysterons. L is an arbitrary memory curve. The active hysterons are marked green, the inactive hysterons are marked red. The red dots mark the centers of the hysterons, which correspond to the locations where $\mu\left(\beta, \alpha\right)$ is defined. Taken from [44], modified.

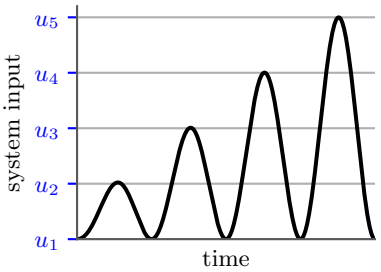

(B) Probe signal with 4 peaks / 5 input levels, appropriate to identify the system in (A).

FIGURE 5.3.4: Discrete version of a Preisach triangle (A) including the probe signal required for identification (B).

of the system were activated by the probe signal at which time. This information can be easily obtained by simulating the memory curve L. For each change in $u(t)$, the memory curve is calculated accordingly, and it is evaluated which hysterons are active.

If both the output of the system and the hysteron states are known, the weight function $\mu(\beta, \alpha)$ can be determined. Assuming the probe signal $u(t)$ consists of n_t samples recorded in the time period $t_1 < t < t_{n_t}$, the output of the system at each of these time points is given by [36]

$$\begin{bmatrix} y(t_1) \\ \vdots \\ y(t_{n_t}) \end{bmatrix} = \begin{bmatrix} R_1(t_1) & ... & R_{n_q}(t_1) \\ \vdots & \ddots & \vdots \\ R_1(t_{n_t}) & ... & R_{n_q}(t_{n_t}) \end{bmatrix} \begin{bmatrix} \hat{\mu}_1 \\ \vdots \\ \hat{\mu}_{n_q} \end{bmatrix} + \eta \tag{5.3.3}$$

where $\hat{\mu}_{1,...,n_q}$ refers to the value of the discrete weight function $\mu(\beta, \alpha)$ for the corresponding hysteron with output $R_{1,...,n_q}$ and η is a constant offset. The offset must be taken into account so that any offset of the output of the system is not included in the weight function - this can lead to reduced quality of results [36]. Equation (5.3.3) is an overdetermined linear system of equations in which the vector $[\hat{\mu}_1, ..., \hat{\mu}_{n_q}]^T$ and η are the only unknown variables. The discrete weight function and offset can be determined by a least squares fit. This provides the complete description of the examined system.

If the weight function describing the system is known, the voltage required to achieve a desired displacement can be calculated. However, since no direct mathematical inversion of the Preisach model exists, the determination of the desired voltage must be done numerically. In the context of this work, the "closest match algorithm" as proposed in [45] is used.

The goal of the algorithm is to find the input u^* whose output is closest to a desired output $\bar{y}$, based on the past and the current state of the discretized system. For this purpose, the current input is varied until the output calculated on the basis of the fitted weight function of the system reaches the desired value, but without leaving the allowed input range or exceeding or falling below the target output, which would corrupt the memory curve and prevent further simulations proceeding from the current state. A flowchart of the algorithm is shown in simplified form[10] in fig. 5.3.5.

The algorithm is initialized with a starting input $u^{(0)}$, an associated output $y^{(0)}$ and a Preisach triangle with a memory curve $L^{(0)}$ and a weight function $\mu(\beta, \alpha)$ obtained by the fit procedure described before. At the start of the algorithm, i.e. iteration 0, it is checked whether the current output $y^{(0)}$ is larger or smaller than the desired output $\bar{y}$. If the current output is smaller than the desired output, it is increased iteratively by $\Delta u = (u_{\text{max}} - u_{\text{min}})/n_h$. Iteration continues until either the output of the system reaches the desired output or the allowed maximum output u_{max} is reached. Once the maximum output is reached, u_{max} is output as the best matching input u^*. If the target output is exceeded before the maximum input is reached, the current output $y^{(n)}$ is compared to the output $y^{(n-1)}$ of the last iteration. Based on which output deviates less from the target output, the current input $u^{(n)}$ or the input $u^{(n-1)}$ of the previous iteration is output as the best-fit input u^*. If the previous iteration is chosen, the system is completely reset to the previous iteration. This requires that during each iteration the memory curve, which contains the information about the current states of the hysterons, is buffered. This is not shown in the flowchart for the sake of simplicity. The case in which $y^{(0)} > \bar{y}$ applies initially is analogous to the case explained, and therefore requires no separate explanation.

[10] The technically interested reader is referred to the appendix (chapter 7), which contains the complete non-simplified algorithm in detailed pseudo-code, which was implemented in Python as part of this work.

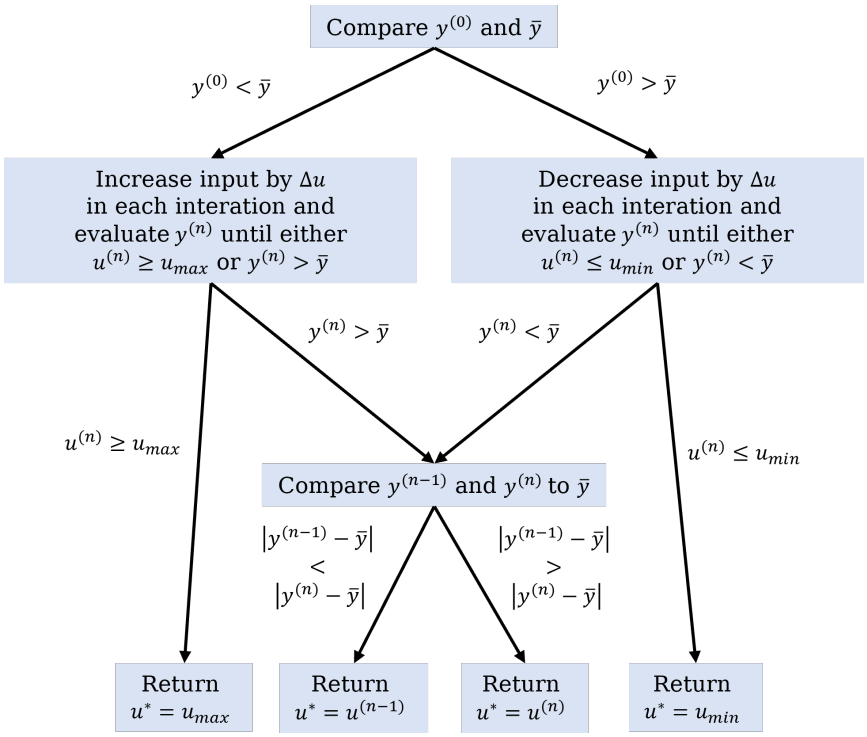

FIGURE 5.3.5: Simplified flowchart of the "closest match algorithm" as proposed by [45].

Regarding the practical use of the algorithm, it must be noted that during a single run, the algorithm only returns the best-fitting input for a single desired output. If, as in this work, a signal of a gravitational wave consisting of n samples is to be simulated with a piezo, the algorithm must be executed successively for each of these samples, using the memory curve of the last run of the algorithm as the starting point.

Hysteresis correction with the "closest match algorithm" for the piezo in the voltage range up to 100 V

In order to verify whether the hysteresis of the piezos used can be corrected by fitting and inversion of a discrete Preisach model, the explained procedure was tested on the piezo of the large mirror. For this purpose, the complete usable voltage range from 0 V to 100 V was utilized, which was subdivided with a discretization level of $n_h = 20$. Accordingly, a probe signal with 20 peaks was applied to the piezo to identify the weight function. A period of 18 seconds was chosen for the total duration of the probe signal to operate below the time scales where any thermal drift might be relevant. The probe signal, along with the response of the interferometer output to the last peak, is shown in fig. 5.3.6a. To estimate the uncertainty, the measurement was performed ten times. To calculate the displacement of the piezo from the interferometer output, the method discussed earlier was used. The calculated displacement is illustrated in fig. 5.3.6b.

The obtained displacement of the piezo fully meets the expectations. If the voltage is increased from 0 V to a value smaller than 100 V, and then decreased again, minor hysteresis loops are generated, which lie in the envelope that is generated when the voltage is increased from 0 V to 100 V and then decreased again.

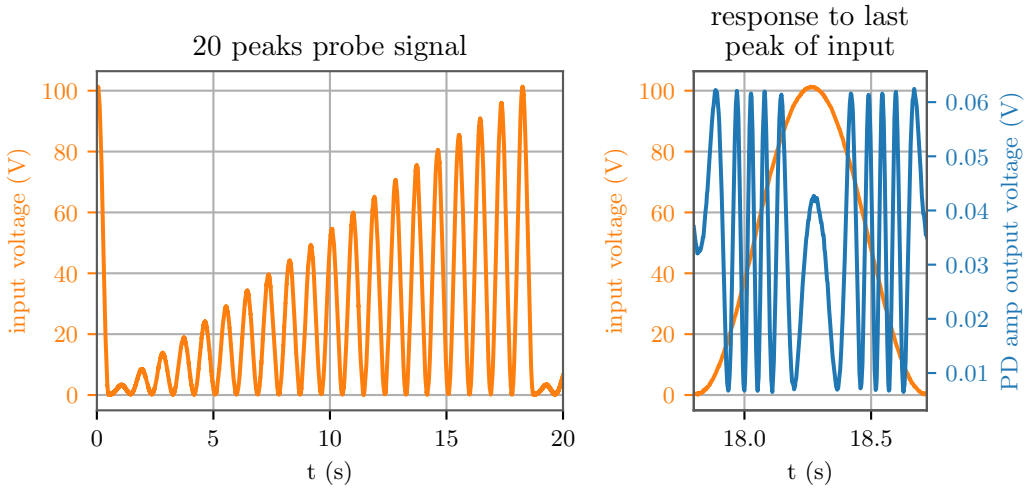

(A) **Left:** Probe signal used to identify the weight function. **Right:** Response of the interferometer output (blue) to the last peak of the probe signal (orange) for better visualization of the process. Uncertainties smaller than symbol size.

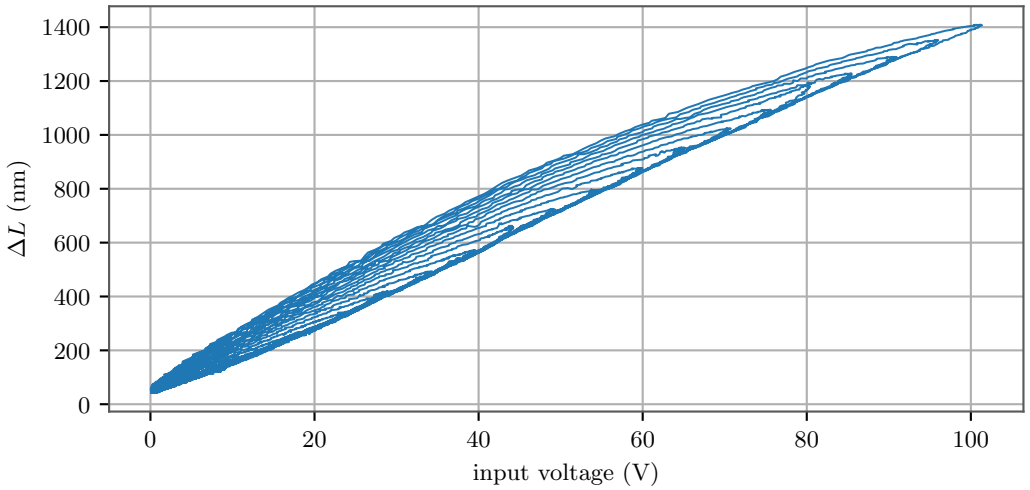

(B) Displacement response of the piezo to the probe signal as a function of the input voltage.

FIGURE 5.3.6: Probe signal to identify the weight function and response of the system, in an operation range from 0 V to 100 V.

To obtain the weight function, the input signal used (the probe signal) was first divided into $n_h = 20$ voltage bins. Starting from the binned signal, the memory curve L was simulated to obtain the time course of the hysteron states R of the discrete Preisach model. Subsequently, the weight function μ and the offset η were obtained by the explained least suqares fit to eq. (5.3.3). For the offset, $\eta = (732.4 \pm 2.0)\,\text{nm}$ was found. The weight function is shown in fig. 5.3.7.

The obtained results of the fit agree with the expectations for the model. An important observation is that most of the weight lies on the diagonal of the Preisach triangle. Above the diagonal, the weight function has significantly lower values. This can be explained by the fact that the hysteresis of the measured piezo is relatively small, and the ascending and descending branches are relatively close to each other. A theoretical Preisach triangle, which has only weights on the diagonal, corresponds to a system completely without hysteresis, since the

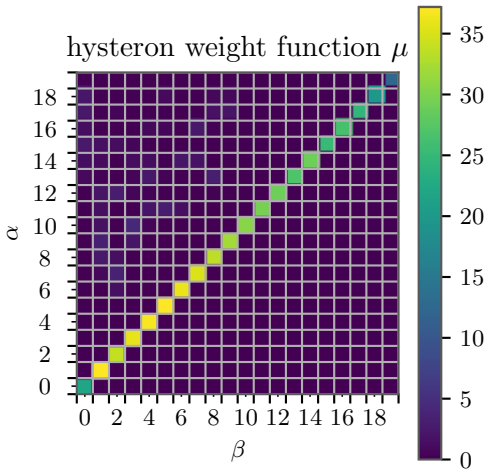

FIGURE 5.3.7: Plot of the fitted weight function $\mu(\beta, \alpha)$ in the Preisach triangle. Note: The Preisach triangle includes only the half-plane $\alpha \geq \beta$. The values of the cells with $\alpha \leq \beta$ are uniformly 0, since $\mu(\beta, \alpha)$ is undefined here. This relationship is difficult to see because the values of $\mu(\beta, \alpha)$ above the diagonal are very small.

switch-on and switch-off thresholds of all hysterons, whose weight is not 0, are identical. The obtained value of $\eta = (732.4 \pm 2.0)$ nm also corresponds to the expectations, since it is about half as large as the maximum measured displacement of the piezo ($1/2 \cdot \Delta L_{\text{max}} = (684.0 \pm 1.5)$ nm). This is a logical consequence of the fact that the hysterons have an output of -1 when switched off, and an output of $+1$ when switched on. Thus, if half of all hysterons are activated, the summed output of the hysterons (ignoring the weight function) is 0. The difference between η and $1/2 \cdot \Delta L_{\text{max}}$ is caused by the weights of the hysterons.

To assess the quality of the fit, the output of the fitted discrete Preisach model for the probe signal used, compared to the previously measured response of the piezo to this probe signal, is shown in fig. 5.3.8. Regarding the type of representation, it should be noted that the output of the fitted Preisach model is independent of time, and depends only on the input of the model - for the purpose of comparison, the output was projected onto the same time axis as the measured output of the piezo.

Comparing the outputs of the real and fitted systems directly reveals the discrete nature of the model used, evident from the step-like slope of the model output. Overall, however, the discrete Preisach model reproduces the real data with very high accuracy, as can be seen by considering the last peak, shown in fig. 5.3.8a on the right. However, consideration of the first peaks in fig. 5.3.8a also reveals a weakness of the model. Where in the output of the real piezo the first peak is recognizable, the output of the discrete model remains at the minimum possible value of 52.19 nm. This is not a computational error, but due to the fact that the first peak of the probe signal generated with the function generator was a few millivolts lower than the first bin of the discrete model at $u_{\text{max}}/20 = 5.668$ V, and the first hysteron at this voltage is thus still assumed to be inactive. However, since minor deviations of a voltage signal are a systematic problem that occurs in any real experimental setup, this should be understood less as a problem of this particular fitting of the Preisach model, and more as a general problem in fitting the Preisach model to real measured data.

Looking at the output of the model compared to the measured hysteresis curves, shown in fig. 5.3.8b, also shows how well the model approximates the real data. However, due to the discrete nature of the model, the quantification of the goodness of fit is challenging. This is demonstrated by the calculation of the reduced chi-squared value often used for assessing goodness of fit. Given the Preisach model fitted to the data, this can be defined as

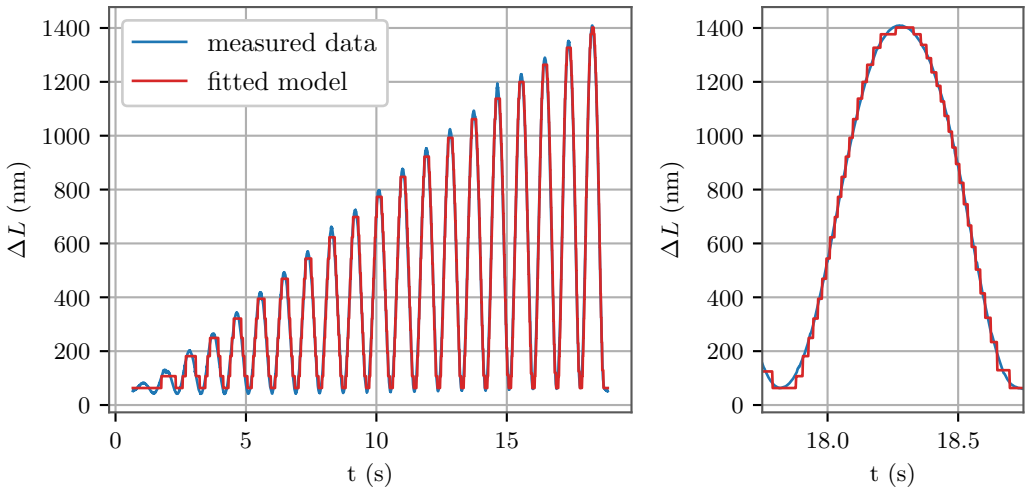

(A) Comparison of the response of the piezo to the probe signal (blue) with the response of the fitted discrete Preisach model to the same probe signal (red), as a function of time. **Left:** Overview of the complete probe signal. **Right:** Comparison of the last peak. Uncertainties of measured data smaller than symbol size.

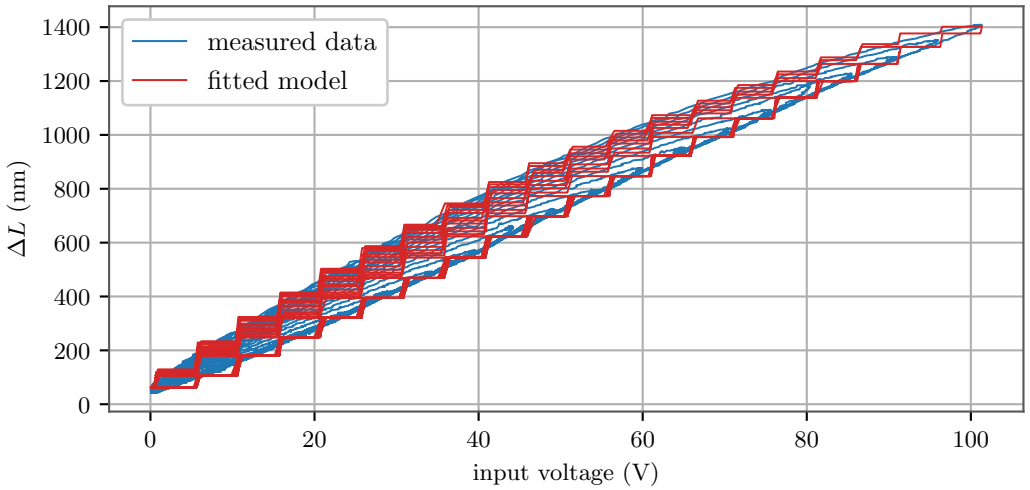

(B) Comparison of the response of the piezo to the probe signal (blue) with the response of the fitted discrete Preisach model to the same probe signal (red) (same data set as in (A)), here as a function of input voltage, analogous to the plot in fig. 5.3.6b. Uncertainties of measured data smaller than symbol size.

FIGURE 5.3.8: Comparison of the output of the real piezo and the output of the fitted model in response to the probe signal.

$$\chi^2_\nu = \frac{\chi^2}{\nu} = \frac{1}{\nu} \sum_i \frac{\left(y_i^{\text{piezo}} - y_i^{\text{Preisach}}\right)^2}{\sigma_i^2} \tag{5.3.4}$$

where y_i^{piezo} denotes the real measured data including uncertainties σ_i, y_i^{Preisach} the output of the model, and i the number of data points. The number of degrees of freedom is described by ν, where here $\nu = 211$, since the fit adjusts the weights of 210 hysterons as well as the constant offset eta. Applying eq. (5.3.4) to the presented data set, one obtains $\chi^2_\nu = 90.876$. Intuitively, the model thus appears to represent the data poorly. In the given scenario,

however, such a high χ^2_ν value is not unusual, since a discrete model with relatively low resolution is fitted here to continuous measured data.

In order to better assess the actual quality of the model, it is useful to evaluate the performance of the model with respect to its intended purpose, i.e. the correction of the hysteresis. For this purpose, an attempt was made to increase the displacement of the piezo as linearly as possible, i.e. without hysteresis, up to the maximum displacement and then to decrease it. Accordingly, a triangular signal $\Delta L(t)$ was created with a total of 200 points, which is shown in blue in fig. 5.3.9.

Subsequently, the explained "closest match algorithm" was used for all data points of the signal to determine, based on the fitted model, the voltages with which the piezo must be driven to achieve the desired displacement as accurately as possible. The voltage states calculated in this way are inherently discrete (cf. red line in fig. 5.3.9). In order to use the calculated voltages as input of the piezo, the staircase-like signal was linearly interpolated. The centers of the "steps" as well as the first and the last data point itself were used as interpolation points. The interpolation is shown as an orange line in fig. 5.3.9. Looking at the calculated input signal, which is supposed to compensate for the hysteresis, it is noticeable that its shape is "inverse" to the hysteresis, as expected. On the descending branch, the voltage is lowered faster than it was increased on the ascending branch to avoid the typical "lag" of hysteresis. Before using the calculated voltage signal on the piezo, a cross-check is performed. This is done by using the calculated voltage signal as input to the Preisach model to check the expected output of the real system. This is shown as a purple staircase in fig. 5.3.9, including an interpolation of this staircase in pink. According to the expectations, the output of the model is almost identical to the triangular signal that is to be reproduced.

To check the success of the method, the response of the real piezo to the calculated corrected voltage signal was compared with the response to a simple triangular signal with

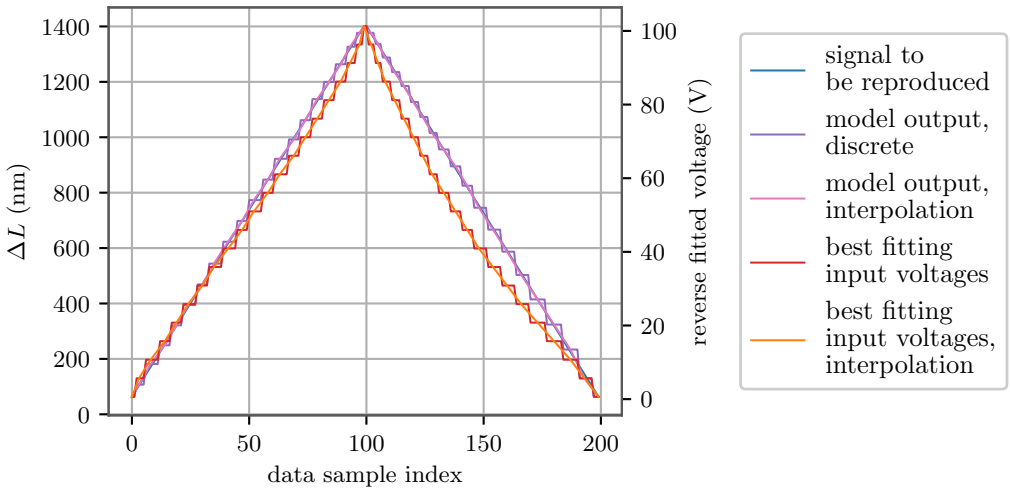

FIGURE 5.3.9: Representation of the triangle signal to be reproduced (blue), together with the calculated voltages to reproduce the signal (red). The interpolation of this voltage signal is shown in orange. Also shown is the result of the cross-check (model output of the calculated voltage signal) in purple, and its interpolation in pink. The calculated voltages refer to the right axis, the signal to be reproduced and the result of the cross-check to the left axis. The signal to be reproduced is difficult to recognize, as it is almost congruent with the result of the cross-check.

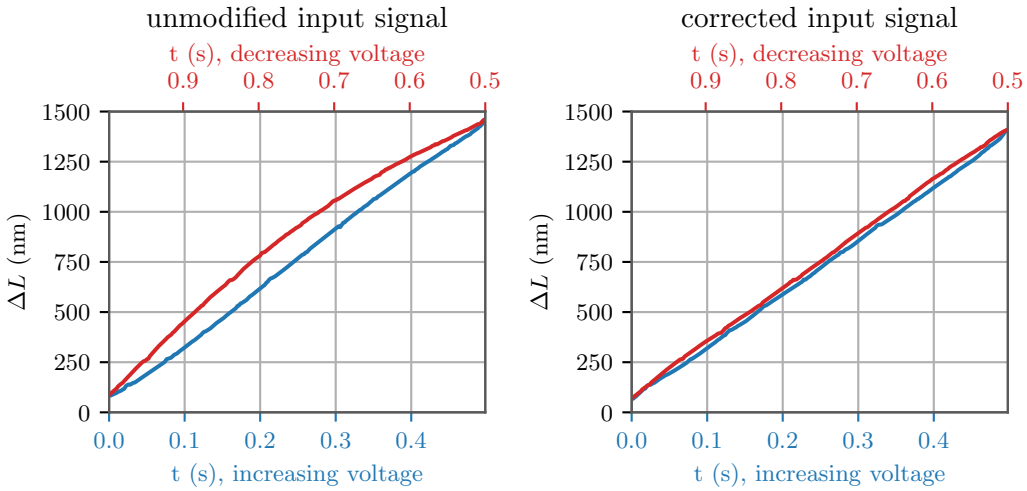

FIGURE 5.3.10: **Left:** Response of the piezo to an unmodified triangular signal. **Right:** Response of the piezo to the corrected voltage signal for hysteresis compensation. In both cases, the descending branch (red) is plotted in reverse time above the ascending branch (blue) for comparison, indicated by the reversed time axis at the top. Uncertainties smaller than symbol size.

an amplitude of 100 V. In both cases, the response to ten signals, each with a period of one second, was determined and averaged. The results are illustrated in fig. 5.3.10.

Examination of the results shows that the hysteresis correction does indeed work very well. Considering the response of the piezo to the corrected input signal, it is immediately noticeable that the hysteresis has been almost completely eliminated compared to the already known response to a conventional triangular signal. In order to capture the improvement mathematically, the displacement in the middle of the ascending as well as the descending branch (i.e. at 0.25 s as well as 0.75 s) was compared for both signals. With uncorrected signal, the displacements at the midpoints of the branches are (767 ± 5) nm and (921 ± 13) nm, respectively, which is a relative difference of $(20.0 \pm 1.9)\%$. Taking the uncertainties into account, this result agrees with the result discussed earlier in this section (depicted in fig. 5.3.3). Looking at the corrected signal, the extents in the midpoints of the branches are (720.0 ± 2.7) nm and (748 ± 4) nm, respectively, corresponding to a relative difference of $(3.8 \pm 0.6)\%$. Compared to the uncorrected signal, the hysteresis was thus reduced by about 81%. This shows that very impressive results can already be achieved with a discretization level of $n_h = 20$. The high effort of adapting the Preisach model to the measured data can thus be worthwhile depending on the application purpose.

Transfer of the demonstrated principle of hysteresis correction to a smaller voltage range up to 9 V

The discussed results show that hysteresis correction using the Preisach model yields very good results in the full usable voltage range up to 100 V. However, when using the interferometer as an outreach experiment, much smaller voltage ranges are used. The use of lower voltages is necessary because the signals of gravitational waves should be displayed on the interferometer in such a way that the brightness of the center fringe visible on the observation screen is unambiguously related to the arm length. As discussed earlier, an unambiguous relationship exists only if the working range is less than a quarter wavelength of the laser. In the following, it is therefore investigated how well the demonstrated principle of hysteresis correction can be transferred to smaller voltage ranges.

For this purpose, the same measurements as for the larger voltage range were carried out, with appropriate adjustments. The voltage range was limited to a maximum of 9 V, since it was seen in past measurements that the displacement of the piezo to be expected at this voltage is about 110 nm, which is well below $\lambda/4 = 133\,\text{nm}$. In addition, a safety buffer of more than 20 nm is included to operate safely within the intended range even in the presence of minor imperfections such as misalignment of the optics or inaccurate adjustment of the operating point for destructive interference. The discretization level chosen was $n_h = 10$. A higher discretization level could not be realized because the responses of the interferometer output to the first peaks of the probe signal are too close to the noise level at lower voltages than $9\,\text{V}/n_h = 0.9\,\text{V}$. For the period of the probe signal, five seconds were chosen. The period was chosen shorter than that of the probe signal in the large voltage range because the interferometer output is closer to the noise level in this measurement, and 50 instead of 10 measurements had to be performed to obtain a result in which the lowest peak of the probe signal is sufficiently distinguishable from the noise. The response of the interferometer to the probe signals as a function of time, as well as a function of input voltage, is displayed in fig. 5.3.11.

The measured response of the piezo to the probe signal fully meets the expectations. The comparison of fig. 5.3.11a with fig. 5.3.6a (plot on the right) illustrates well the advantage of the small voltage range, which lies in the unambiguity of the data. The hysteresis, well visible in fig. 5.3.11b, is expectedly less pronounced in the investigated voltage range than in the complete voltage range up to 100 V. Compared to fig. 5.3.6b, the minor hysteresis loops are visually less distinguishable from each other.

The weight function $\mu(\beta, \alpha)$ fitted to the data according to the explained methods, shown in fig. 5.3.12, reflects this observation: the weight lies almost exclusively on the diagonal of the Preisach triangle. As expected, the values of the weights are lower than in the large voltage range, since they correspond to the values of the displacement, which are equally lower. The fitted value of the constant offset is $\eta = (58.3 \pm 0.4)\,\text{nm}$, which meets the expectations.

The comparison of the output of the model with the measured displacement behavior of

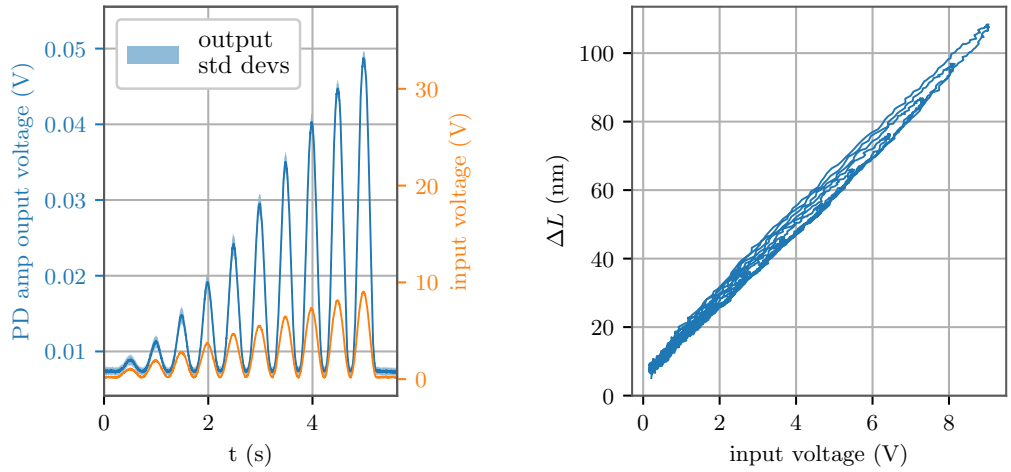

(A) Probe signal used to identify the weight function (orange), including the response of the interferometer output (blue) for better visualization of the process.

(B) Displacement response of the piezo to the probe signal as a function of the input voltage. Uncertainties not included for better overview.

FIGURE 5.3.11: Probe signal to identify the weight function and response of the system, in an operation range from 0 V to 9 V.

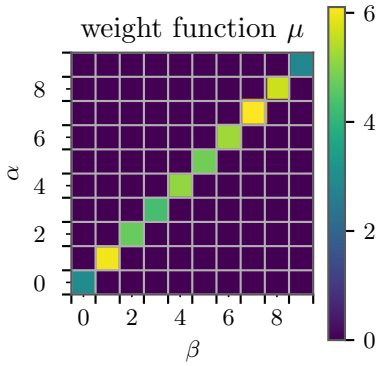

FIGURE 5.3.12: Plot of the fitted weight function $\mu(\beta, \alpha)$ in the Preisach triangle. Note: The Preisach triangle includes only the half-plane $\alpha \geq \beta$. The values of the cells with $\alpha \leq \beta$ are uniformly 0, since $\mu(\beta, \alpha)$ is undefined here. This relationship is difficult to see because the values of $\mu(\beta, \alpha)$ above the diagonal are very small.

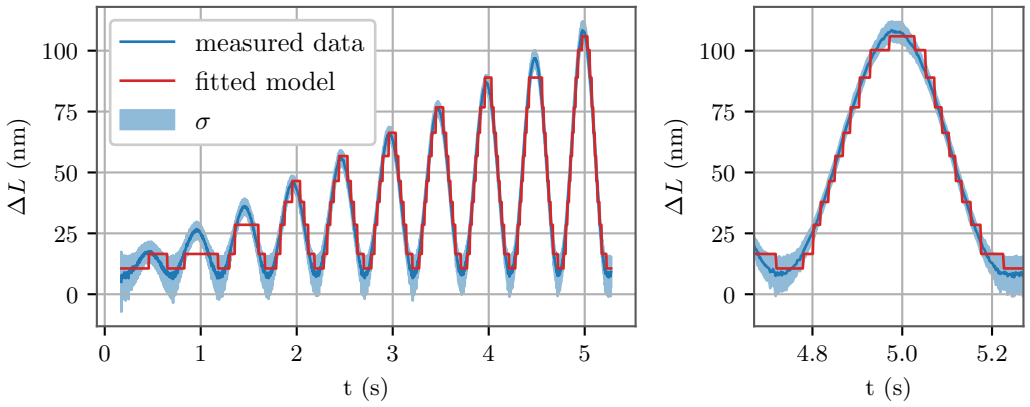

(A) Comparison of the response of the piezo to the probe signal (blue) with the response of the fitted discrete Preisach model to the same probe signal (red), as a function of time. **Left:** Overview of the complete probe signal. **Right:** Comparison of the last peak. Uncertainties σ shown as light blue area.

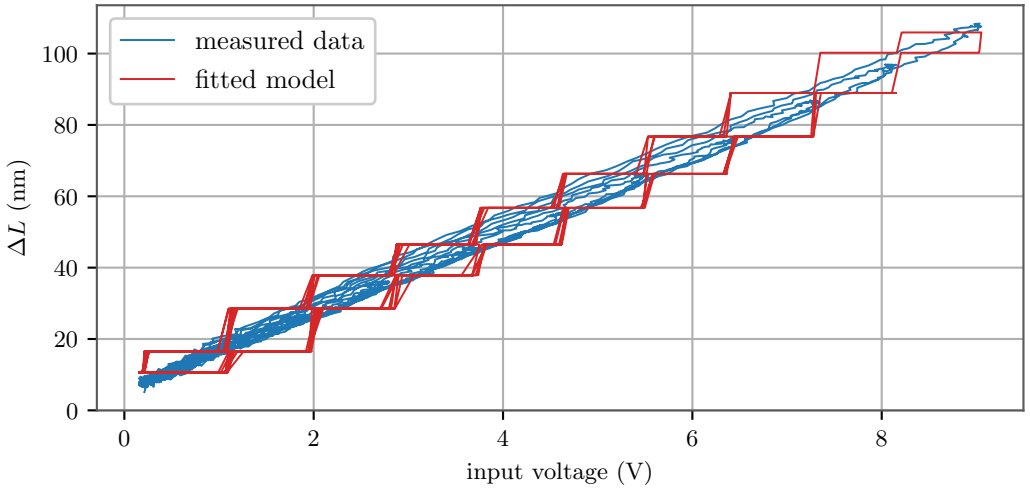

(B) Comparison of the response of the piezo to the probe signal (blue) with the response of the fitted discrete Preisach model to the same probe signal (red) (same data set as in (A)), here as a function of input voltage, analogous to the plot in fig. 5.3.11b. Uncertainties not included for better overview.

FIGURE 5.3.13: Comparison of the output of the real piezo and the output of the fitted model in response to the probe signal.

the piezo is shown in fig. 5.3.13, where the same representation form as in fig. 5.3.8 was chosen. Here, the disadvantage of the reduced discretization level is well visible. Especially the second, third and the second to last peak, shown in fig. 5.3.13a (left plot), are not modeled accurately, because the amplitudes of the peaks in the probe signal created with the function generator deviate slightly from the borders of the voltage bins of the discrete model. This problem generally also exists at higher discretization levels (e.g. as previously observed in the full voltage range with $n_h = 20$), but is not as significant there. Furthermore, especially at the last peak, shown in fig. 5.3.13a (right plot), it is recognizable that the behavior of the real system is not reproduced as precisely as with a higher discretization. For the sake of completeness, the value of $\chi^2_\nu = 1.852$ associated with the fit should also be mentioned here. This is significantly lower than the value of $\chi^2_\nu = 90.876$, which was obtained for the fit in the large voltage range. The obvious reason is that the uncertainties relative to the measured data are much larger due to the lower amplitude of the displacement of the piezo. Although the model with the lower discretization level reproduces the measured data less precisely, as expected, the value of χ^2_ν does not reflect this.

In order to compare the results in the small voltage range with the results in the large voltage range, the success of the hysteresis correction was again checked on the basis of a triangular signal $\Delta L(t)$, which is to be tracked with the piezo. Completely analogous to the approach in the larger voltage range, the "closest match algorithm" was used to compute, based on the fitted model, the voltage profile that must be used as input to the piezo in order to best match the desired displacement curve. Figure 5.3.14a shows the triangular signal to be reproduced, the voltages computed with the algorithm (including linear interpolation), and the output of the system simulated as a cross-check using the computed voltage signal (also including linear interpolation).

When looking at the interpolation of the computed voltages, it is noticeable that they deviate significantly less from the symmetry of the triangle than in fig. 5.3.9. This is in line with expectations, since in the limited voltage range considered, the hysteresis is lower than in the full range.

Figure 5.3.14b shows the responses of the piezo to an unmodified triangle signal (left) and to the voltage signal computed using the "closes match algorithm". The descending branch of the triangle is again "flipped over" in time to allow comparison with the ascending branch. Unlike the correction in the full voltage range, the correction of the hysteresis does not seem to work effectively here. This is clearly noticeable in a visual comparison. A quantitative comparison of the displacements of the midpoints of the ascending and descending branches (at 0.25 s and 0.75 s, respectively) confirms this: for the signal without correction the relative difference is $(6.2 \pm 0.7)\%$, for the signal with correction the relative difference is $(6.4 \pm 0.6)\%$. Consequently, the hysteresis is not corrected. The reason for this is the low discretization of the model, which cannot be chosen higher due to the signal quality. Another noteworthy feature is that the inaccurate model produces artifacts in the time evolution of the displacement when the hysteresis correction is attempted. This is well visible in the right plot in fig. 5.3.14. The beginnings and ends of both the ascending and descending branches appear slightly bent. In view of the rather poor fit of the model to the data, this is not surprising.

Upon final review of the results, it can be stated that hysteresis correction by fit of the Preisach model yields good results in the full voltage range of the piezo, while no correction of hysteresis is achieved in the reduced voltage range. The crucial limitation is the discretization level of the model, which is practically limited by the signal quality of the interferometer output. With respect to the outreach experiment, where small voltage ranges are used, hysteresis correction with the Preisach model thus does not seem to be the ideal method. Regarding the discussed results, the question arises whether a hysteresis correction

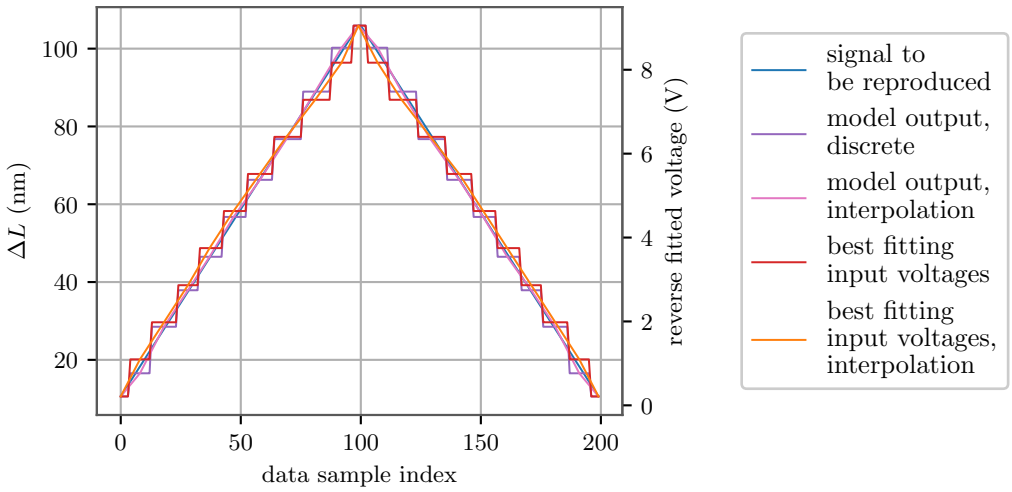

(A) Representation of the triangle signal to be reproduced (blue), together with the calculated voltages to reproduce the signal (red). The interpolation of this voltage signal is shown in orange. Also shown is the result of the cross-check (model output of the calculated voltage signal) in purple, and its interpolation in pink. The calculated voltages refer to the right axis, the signal to be reproduced and the result of the cross-check to the left axis. The signal to be reproduced is difficult to recognize, as it is almost congruent with the result of the cross-check.

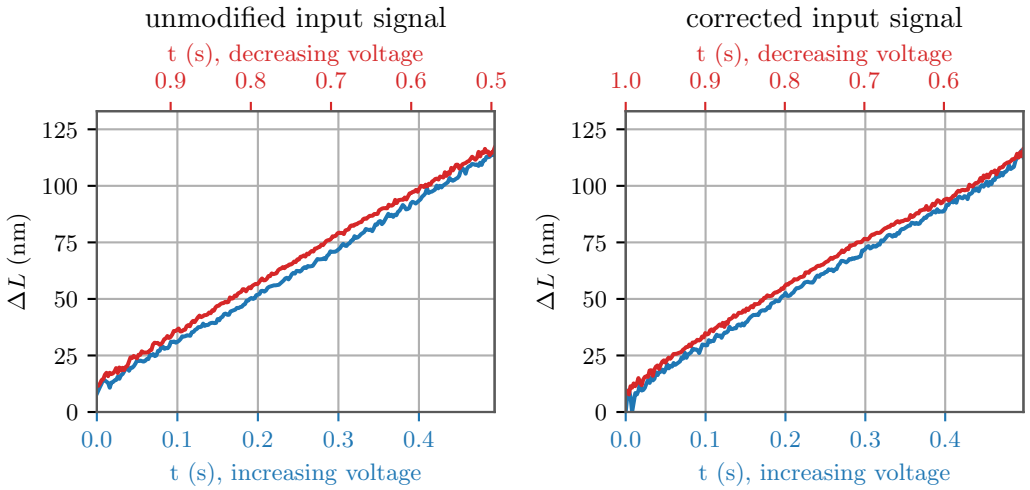

(B) **Left:** Response of the piezo to an unmodified triangular signal. **Right:** Response of the piezo to the corrected voltage signal for hysteresis compensation. In both cases, the descending branch (red) is plotted in reverse time above the ascending branch (blue) for comparison, indicated by the reversed time axis at the top. Uncertainties not included for the sake of clarity. For both plots, the average uncertainties of ΔL are about 5 nm.

FIGURE 5.3.14: An attempt at hysteresis correction in the small voltage range. **Top:** Output of the "closest match algorithm" for tracking a triangular signal. **Bottom:** Comparison of the piezo's responses to an unmodified triangular signal and to the corrected signal calculated by the algorithm.

is necessarily required for the representation of gravitational wave signals, since the hysteresis in the corresponding voltage range is already significantly smaller than in the full voltage range. As is shown in the next chapter, the hysteresis correction is indeed not sensible in the outreach experiment, yet this does not limit the experiment's quality.

5.4 Use of the interferometer for visualizing gravitational wave signals

Now that the setup has been discussed in detail, this final section will deal with the verification of the core function of the interferometer, i.e. the simulation of gravitational wave signals. As a test signal, to be visualized with the interferometer, the "GW150914" depicted in fig. 3.3.2 was chosen, since this is an excellent candidate for this due to its high popularity and scientific importance. The event data has been published by the LIGO Scientific Collaboration, and is openly available at [46].

As already explained in section 5.3.2, for the representation of a signal the displacement of the piezo must be varied in a range of $\Delta L < \lambda/4$, so that for the observer an unambiguous correlation between the brightness of the center fringe on the screen and the change of the arm length, i. e. the strain imposed by the gravitational wave, is recognizable. The maximum strain of the signal, reached at about 0.42 s, was therefore scaled to a target displacement of 105.92 nm, which corresponds to the highest voltage bin (upper threshold of the highest row of hysterons) of the model fitted to the desired range. The baseline of the gravitational wave signal was scaled to half of the maximum displacement, and thus lies in the middle between constructive and destructive interference. It should be mentioned that the selected scaling only applies to the piezo of the large mirror, which was examined in the last section for its hysteresis behavior. All the investigations listed below were also carried out with this piezo for the sake of comparability. The strain of the gravitational wave to be simulated, as well as the rescaling to the desired displacement of the piezo, are shown in fig. 5.4.1a.

Regarding the visualization of the signal, the performance of two approaches will be compared. The first approach assumes an approximately linear relationship between the input voltage and the displacement of the piezo, meaning that the hysteresis is ignored. To track the gravitational wave signal, the target displacement is simply scaled linearly to an input voltage range of the piezo from 0 V to 9 V, as used in the previous section. Second approach is to use the Preisach model and the "closest match algorithm" to calculate the voltage which, according to the model, most closely matches the gravitational wave signal to be reproduced. For this purpose, the fit of the Preisach model performed and explained in section 5.3.2 is used in the considered voltage range from 0 V to 9 V. The interpolated output of the "closest match algorithm" for the signal to be reproduced is shown in fig. 5.3.14b.

Analogous to the observations in section 5.3.2, the disadvantage of the Preisach model with a too low discretization level also becomes apparent in fig. 5.4.1b. For instance, the same target voltages are calculated for all peaks up to approximately 0.37s. The differences in the amplitudes of the peaks of the gravitational wave signal are too small to be considered by the discrete model with only 10 different voltage levels. A similar problem occurs at the end of the signal. Since the amplitude of the gravitational wave signal varies not sufficiently here for the desired voltage to change, the last interpolation step is relatively long. A manual correction of the interpolation would be possible, but against the sense of the comparison of the methods.

To compare the performance of the two approaches, the responses of the piezo to the signal assuming linear correlation as well as to the signal obtained from the "closest match algorithm" were recorded. As duration of the input signals of the piezo 4.6 s were chosen. This is a factor of 21.9 longer than the gravitational wave signal duration of 0.21 s. The scaling was chosen so that the signal can be easily followed and understood by the observer, which is not the case with a duration of just two tenths of a second. The non-integer value of the chosen factor is caused by the fact that at the used function generator only fixed sampling rates can be used. All measurements were performed ten times to obtain standard deviations. The results are illustrated in fig. 5.4.2. To assess the degree of similarity between the responses and the signal to be replicated, the gravitational wave signal and the responses were

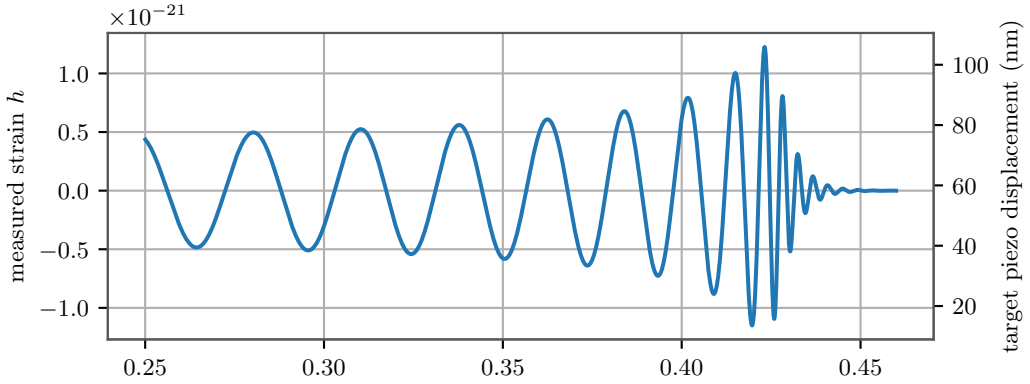

(A) Measured strain of the binary black hole merger "GW150914" (left axis), as well as rescaling in target displacement of the piezo to display the signal on the interferometer (right axis). Time scale according to original data.

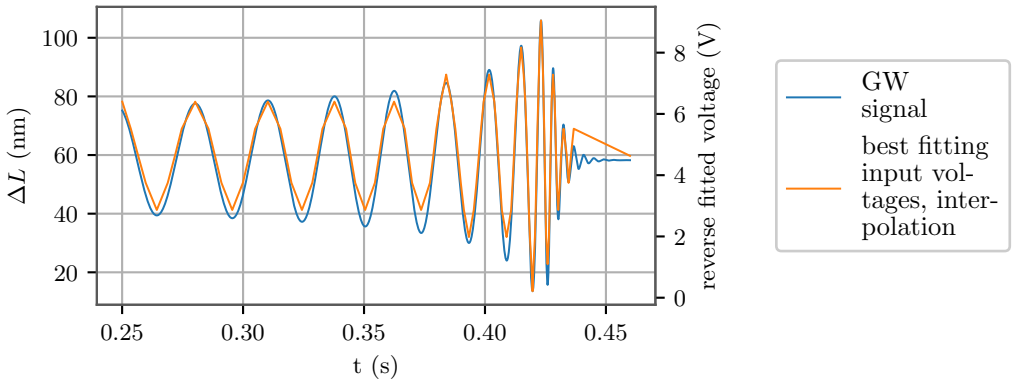

(B) Gravitational wave signal to be reproduced (blue), together with the linear interpolation of the computed voltages to reproduce the signal (orange). The computed voltages refer to the right axis, the signal to be reproduced to the left axis.

FIGURE 5.4.1: Gravitational wave signal to be reproduced, including scaling to the desired displacement of the piezo, and voltages computed with the "closest match algorithm" to reproduce this signal.

each scaled to a maximum amplitude of 1 and a baseline of 0. To employ a quantitative measure of similarity, the difference between the piezo's response and the gravitational wave signal was calculated, and also plotted. The time axis of the recorded responses is scaled to align with the time axis of the gravitational wave signal.

When looking at the results for the input signal without correction, it is noticeable that each peak of the gravitational wave signal is reproduced well. This is especially clear from the magnification in the lower left in fig. 5.4.2, where it is visible that the deviations between output and target are within the order of magnitude of the measurement uncertainties. With respect to the use as an outreach experiment this implies that the existing differences between the response of the piezo and the gravitational wave signal serving as a template are sufficiently small for the observer of the outreach experiment not to be able to notice them. Upon close inspection, a lag between the piezo's response and the gravitational wave signal is apparent. As can be seen by the residuals in green, this lag is more pronounced in the later part of the signal (around 0.41 s to 0.43 s in gw time) than in the first part of the signal. Since the piezo's response and the gravitational wave signal refer to two different time axes that have merely been scaled to the same length, this lag should not be taken as absolute,

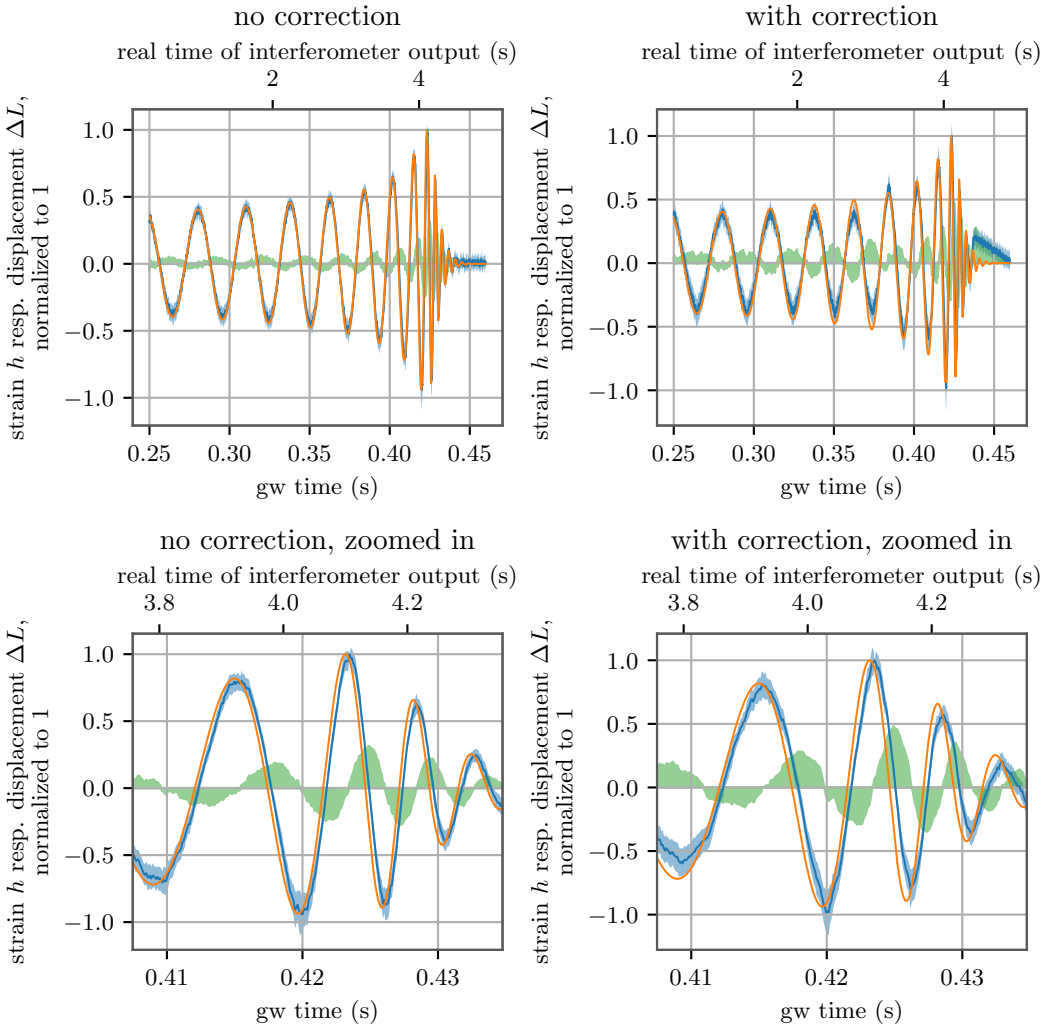

FIGURE 5.4.2: Displacement responses of the piezo to the signals generated after the two explained approaches (blue) compared to the gravitational wave signal to be reproduced (orange). The uncertainties of the displacement are shown as the light blue area. The green region denotes the difference between the gravitational wave signal and the response of the piezo. Both strain and displacement are normalized to a maximum amplitude of 1 with a baseline of 0. Strain and interferometer output refer to their own lower and upper time axes, respectively. The **left column** ("no correction") refers to the signal where a linear relationship was assumed, the **right column** ("with correction") refers to the signal generated using the "closest match algorithm". For better visibility, the **bottom row** shows a zoom of the signal part between 0.41 s and 0.43 s.

but rather as an indication that, as expected, the piezo's response time is more significant at higher frequencies than at lower ones. The lag observed here is comparable in magnitude to the rise and fall times observed in section 5.3.1.

Considering the results of the approach using the Preisach model, a look at the residuals shows that the deviations are larger overall than for the ansatz assuming a linear relationship. Especially the already mentioned interpolation artifact near the end of the signal is significant. The lag is also larger compared to the linear approach. It is assumed that this too is caused by the low discretization level of the Preisach model. This leads to a lower resolution of the

voltage signal calculated by the "closest mach algorithm", which in turn leads to a coarser interpolation. This in turn can manifest itself, among other things, in a temporal offset.

To quantitatively assess the accuracy of the gravitational wave signal replication for both approaches, the integral of the difference given by

$$\int_{0.25\,\mathrm{s}}^{0.46\,\mathrm{s}} |\Delta L^* - h^*|\, dt_{\mathrm{gw}}, \tag{5.4.1}$$

where ΔL^* corresponds to the normalized piezo displacement and h^* corresponds to the normalized gravitational wave strain, can be employed. This integral corresponds to the absolute of the green area plotted in fig. 5.4.2. The integral is 0.0072 for the signal assuming a linear correlation, and 0.0158 for the signal based on the fitted Preisach model. The integral is thus larger by a factor of about 2.2 for the Preisach approach than for the linear approach. This result shows that the attempt to correct for hysteresis is ineffective. Not only is the quality of the replicated signal not improved compared to the approach of ignoring the hysteresis, but it is even negatively affected. However, the quality of the outreach experiment does not suffer from this, since the relationship between input voltage and displacement of the piezo is sufficiently linear that gravitational wave signals can be represented without deviations visible to the observer. This is impressively demonstrated by the available results.

Upon final consideration of the present result, it can be concluded that the constructed and commissioned Michelson interferometer very well fulfills its task of visualizing gravitational wave signals in order to present them in outreach experiments. The gravitational wave signals are reproduced with high accuracy so that an observer can easily follow the course of the signal. Thereby, any desired signal can be scaled using the explained procedure and displayed on the interferometer.

6 Conclusion

In this master thesis, a Michelson interferometer is constructed with the goal of illustrating the complex principles of gravitational wave detection in a simple manner in the context of an outreach experiment.

A central part of the work is the development and realization of a setup that is specifically designed to visualize the effect of a gravitational wave including the possibility to quantitatively measure the displayed wave. To achieve this goal, a classical Michelson interferometer is constructed with several enhancements. The first important design decision is the integration of a second beamsplitter, through which the generated interference pattern can be simultaneously projected onto an observation screen and onto a photodetector for performing measurements. The second extension, elementary to the outreach experiment, is the use of piezo actuators for translation of the mirrors, which allows the variation of the arm length and thus the display of gravitational wave signals. As measures for seismic isolation, the base plate of the interferometer is provided with feet made of polyurethane, and placed on a table with a granite table top and a total mass of about 100 kg. Furthermore, a servo circuit is employed to adjust the arm length. To be able to use the experimental setup later as an outreach experiment, the function of the individual components is characterized and optimized.

Analysis of the vibration reduction measures shows that they partially fulfill their intended function. For seismic activities with frequencies greater than 100,Hz, vibrations are damped with a maximum attenuation of more than 25 dB. However, for lower frequencies between 3 Hz and about 40 Hz, the vibrations are found to be amplified by more than 10 dB in some cases, for which no cause can be identified. Further research in the future may be instructive here. Since in practical application it is found that the advantages of damping high-frequency vibrations outweigh the disadvantages, the noise reduction measures are retained.

Investigation of the interference contrast shows that the use of a secondary beamsplitter, crucial for use as an outreach experiment, has no negative influence on the interference contrast. A fringe visibility of $K = 0.766 \pm 0.007$ is achieved, which can be considered an excellent result with respect to the theoretical maximum value of 1.

An analysis of the performance of the servo circuit shows that it is capable of setting an interference minimum in under 10 seconds and holding it for a period of one hour. Upon further investigation, it is found that the interferometer output with the servo circuit turned off exhibits a drift that covers the full range from interference minimum to interference maximum over a 30 minute period. It is hypothesized that the drift is of thermal origin. Future studies may be revealing for a better understanding of this behavior. Further, it is found that the drift can be reduced by several orders of magnitude by installing an acrylic cover over the interferometer. Consequently, the drift is not further relevant for use as an outreach experiment.

In order to control the arm length of the interferometer with the highest possible precision, the response behavior of the piezos is analyzed. Examination of the step response of the piezos shows that the time to reach the desired displacement is in the order of $\mathcal{O}(10\,\mathrm{ms})$. Therefore, the reaction times are found low enough to be ignored in the outreach experiment. Comparison of the displacement behavior of both piezos shows that one of them has a

displacement of (1460.09 ± 0.03) nm in agreement with the manufacturer's specifications at 100 V, while the displacement of the other piezo is unexpectedly high with (1919.9 ± 1.6) nm. A production error is suspected to be the reason.

Both piezos exhibit hysteresis of approximately 20%. To correct for hysteresis, the Preisach hysteresis model is implemented and fitted to the behavior of one of the piezos. It is shown that hysteresis can be corrected by numerically inverting the Preisach model by applying the "closest match algorithm". However, this correction only succeeds in the complete available expansion range of the piezo, corresponding to the voltage range from 0 V to 100 V. A correction of the hysteresis in smaller expansion regions up to one quarter of the laser wavelength (corresponding to the voltage range from 0 V to 9 V.), which are used for the representation of gravitational wave signals, remains unsuccessful. This is due to the noise on the interferometer output, which prohibits the evaluation of a higher resolution probe signal, which would be required for a more accurate fit of the Preisach model. However, it is shown that in small expansion ranges the hysteresis is low enough to not visibly distort displayed gravitational wave signals.

Finally, it is demonstrated that gravitational wave signals can be reproduced on the interferometer with very high precision - the deviations between the gravitational wave signal used as a template and the displayed signal are within the measurement uncertainties.

It can be concluded that, within the scope of this thesis, a setup has been created that fully meets the design goal. The setup impressively demonstrates that by implementing appropriate control technology it is possible to display gravitational waves in a way that is comprehensible to an observer, while at the same time measuring what is seen with nanometer precision. Therefore, the setup has great potential in outreach activities.

At the same time, there are still possibilities to extend and improve the hardware of the setup in the future. For instance, past research shows that ways exist to reduce the hysteresis behavior of the piezos without fitting a mathematical model, such as by adding a mechanical bias [47], or inserting a capacitor in series with the piezoelectric actuator to control not the voltage but the charge applied to the piezos [48]. However, these improvements are of more interest for extended use of the interferometer, since the effect of hysteresis on the display of gravitational wave signals is small. More purposeful are further investigations of the observed drift to make the setup usable without the acrylic cover. This would allow the observer in the outreach experiment to be "closer to the action". Furthermore, it seems reasonable to develop a software that allows to create arbitrary signals on the computer, prepare them for the piezo and have them played without having to use the function generator. This would further increase the flexibility of the outreach experiment.

7 Appendix

Closest match algorithm

Pseudo code for the closest match algorithm, as proposed in [45]. The variable y describes the output of the system, while u describes the input. The desired output is marked by $\bar{y}$, the corresponding voltage (which also is the output of the algorithm) is u^*. The system's memory curve is marked by L (not to be confused with the piezo's displacement), the backed up memory curve is denoted $\tilde{L}$. The variable n refers to the current iteration. For the other variables, the current iteration is indicated in the superscript.

- Step 0 [**Initialization**]. Set $n = 0$. Compare $y^{(0)}$ and $\bar{y}$: if $y^{(0)} = \bar{y}$, let $u^* = u^{(0)}$, $L^* = L^{(0)}$, go to Step 3; if $y^{(0)} < \bar{y}$, go to Step 1.1; otherwise go to step 2.1;
- Step 1 [**Case** $y^{(0)} < \bar{y}$].
  - Step 1.1: If $u^{(n)} = u_{\text{max}}$, let $u^* = u^{(n)}$, $L^* = L^{(n)}$, go to Step 3; otherwise $u^{(n+1)} = u^{(n)} + \Delta u$, $\tilde{L} = L^{(n)}$ [back up the memory curve], $n = n + 1$, go to Step 1.2;
  - Evaluate $y^{(n)} = y\left(u^{(n)}; L^{(n-1)}\right)$, and (at the same time) update the memory curve to $L^{(n)}$. Compare $y^{(n)}$ with $\bar{y}$: if $y^{(n)} = \bar{y}$, let $u^* = u^{(n)}$, $L^* = L^{(n)}$, go to Step 3; if $y^{(n)} < \bar{y}$, go to Step 1.1; otherwise go to Step 1.3;
  - Step 1.3: If $|y^{(n)} - \bar{y}| \leq |y^{(n-1)} - \bar{y}|$, let $u^* = u^{(n)}$, $L^* = L^{(n)}$, go to Step 3; otherwise $u^* = u^{(n-1)}$, $L^* = \tilde{L}$ [restore the memory curve], go to Step 3;
- Step 2 [**Case** $y^{(0)} > \bar{y}$].
  - Step 2.1: If $u^{(n)} = u_{\text{min}}$, let $u^* = u^{(n)}$, $L^* = L^{(n)}$, go to Step 3; otherwise $u^{(n+1)} = u^{(n)} - \Delta u$, $\tilde{L} = L^{(n)}$ [back up the memory curve], $n = n + 1$, go to Step 2.2;
  - Evaluate $y^{(n)} = y\left(u^{(n)}; L^{(n-1)}\right)$, and (at the same time) update the memory curve to $L^{(n)}$. Compare $y^{(n)}$ with $\bar{y}$: if $y^{(n)} = \bar{y}$, let $u^* = u^{(n)}$, $L^* = L^{(n)}$, go to Step 3; if $y^{(n)} > \bar{y}$, go to Step 2.1; otherwise go to Step 2.3;
  - Step 2.3: If $|y^{(n)} - \bar{y}| \leq |y^{(n-1)} - \bar{y}|$, let $u^* = u^{(n)}$, $L^* = L^{(n)}$, go to Step 3; otherwise $u^* = u^{(n-1)}$, $L^* = \tilde{L}$ [restore the memory curve], go to Step 3;
- Step 3. Exit.

Table of components

TABLE 7.0.1: Tabular listing of optical components and equipment used.

Model designation	Description	Quantity
Breadboard		
n/a	custom aluminum breadboard, $41 \times 50 \times 4\,\mathrm{cm}$	1
Thorlabs AV4/M	sorbothane rubber feet	4
General mounting equipment		
Thorlabs TRA75/M	75 mm posts	8
Thorlabs PH75/M	75 mm post holders	8
Thorlabs BA1S/M	mounting base	8
Photodetector unit		
Thorlabs SM05PD1A	Si-photodiode, 350 nm - 1100 nm	1
Thorlabs SM05M10	1" long lens tube, 1/2" diameter	1
Thorlabs LMR05AP	alignment help for 1/2" lens tube	1
Thorlabs FL05532-10	532 nm bandpass filter	1
Thorlabs SM05RR	1/2" retaining ring	1
Thorlabs SM05RC/M	1/2" slip ring	1
Light source		
Thorlabs CPS532-C2	532 nm collimated laser, 0.9 mW (class 2)	1
Thorlabs LDS5-EC	laser power supply	1
Thorlabs VC1/M	small V-clamp laser holder	1
Diverging lens		
Thorlabs LA1509 N-BK7	1" plano-convex lens, $f = 100\,\mathrm{mm}$	1
Thorlabs KM100	kinematic mirror/lens mount	1
Beamsplitters		
Thorlabs EBS2	2" 50:50 beamsplitter	2
Thorlabs LMR2/M	2" lens mount with retaining ring	2
Piezo controlled mirrors		
Thorlabs BB1-E02	1" broadband dielectric mirror	1
Thorlabs BB07-E02	0.7" broadband dielectric mirror	1
Thorlabs KM100T	1" threaded kinematic mirror mount	2
Thorlabs SM1CP2	1" externally threaded end cap	2
Thorlabs PA4HEW	Piezoelectric stack actuator (max. 2.1 μm at 150 V)	2
Viewing screen		
Thorlabs EDU-VS1/M	post-Mountable white polystyrene viewing screen	1
Servo circuit		
Phidgets HUB0000_0	control hub	1
Phidgets OUT1000_0	voltage output module, 0 V - 4.2 V	1
Phidgets VCP1000_0	voltage input module (± 40 V)	1
Additional equipment		
Rigol DG1032Z	Two channel function generator	1
PI E-665	piezo controllers/voltage sources	2

Bibliography

[1] Adam Burrows and James M. Lattimer. "Neutrinos from SN 1987A". In: *The Astrophysical Journal* 318 (July 1987), p. L63. DOI: 10.1086/184938. URL: https://doi.org/10.1086/184938.

[2] The Pierre Auger Collaboration. *The Pierre Auger Observatory*. Last retrieved Wednesday 15th June, 2022, 08:33 from https://www.auger.org/. 2022.

[3] The IceCube Collaboration. *IceCube Overview*. Last retrieved Wednesday 15th June, 2022, 08:33 from https://icecube.wisc.edu/. 2022.

[4] Albert Einstein. "The Field Equations of Gravitation". In: *Sitzungsber. Preuss. Akad. Wiss. Berlin (Math. Phys.)* 1915 (1915), pp. 844–847.

[5] *Press release: The Nobel Prize in Physics 2017*. Last retrieved Wednesday 15th June, 2022, 08:33. 2017. URL: https://www.nobelprize.org/prizes/physics/2017/press-release/.

[6] ET steering committee. *ET design report update 2020*. Nov. 2020. URL: https://apps.et-gw.eu/tds/?content=3&r=17245.

[7] Ch.W. Misner, K.S. Thorne, and J.A. Wheeler. *Gravitation*. W. H. Freeman and company San Francisco, 1973. ISBN: 0-7167-0344-0.

[8] Michael Ruhrländer. *Allgemeine Relativitätstheorie Schritt für Schritt*. Springer Berlin Heidelberg, 2021. DOI: 10.1007/978-3-662-62083-0. URL: https://doi.org/10.1007/978-3-662-62083-0.

[9] James B Hartle. *Gravity: An Introduction to Einstein's General Relativity: Pearson New International Edition*. Pearson Education Limited, 2013. ISBN: 978-1-292-03914-5.

[10] Alexandre Le Tiec and Jérôme Novak. "Theory of Gravitational Waves". In: *An Overview of Gravitational Waves*. WORLD SCIENTIFIC, Feb. 2017, p. 33, Figure 9. DOI: 10.1142/9789813141766_0001. URL: https://doi.org/10.1142/9789813141766_0001.

[11] C J Moore, R H Cole, and C P L Berry. "Gravitational-wave sensitivity curves". In: *Classical and Quantum Gravity* 32.1 (2014), p. 015014. DOI: 10.1088/0264-9381/32/1/015014. URL: https://doi.org/10.1088/0264-9381/32/1/015014.

[12] C J Moore, R H Cole, and C P L Berry. *Gravitational Wave Detectors and Sources*. A Gravitational Wave Sensitivity Curve Plotter. Last retrieved Wednesday 15th June, 2022, 08:33 from http://gwplotter.com/. Licensed under a Creative Commons Attribution-NonCommercial-ShareAlike 3.0 Unported License (see https://creativecommons.org/licenses/by-nc-sa/3.0/). 2022.

[13] Vishal Baibhav et al. "Gravitational-wave detection rates for compact binaries formed in isolation: LIGO/Virgo O3 and beyond". In: *Phys. Rev. D* 100 (6 2019), p. 064060. DOI: 10.1103/PhysRevD.100.064060. URL: https://link.aps.org/doi/10.1103/PhysRevD.100.064060.

[14] B. P. Abbott et al. “Observation of Gravitational Waves from a Binary Black Hole Merger”. In: *Phys. Rev. Lett.* 116 (6 2016), p. 061102. DOI: 10.1103/PhysRevLett.116.061102. URL: https://link.aps.org/doi/10.1103/PhysRevLett.116.061102.

[15] Vassiliki Kalogera and Albert Lazzarini. “LIGO and the opening of a unique observational window on the universe”. In: *Proceedings of the National Academy of Sciences* 114.12 (Mar. 2017), pp. 3017–3025. DOI: 10.1073/pnas.1612908114. URL: https://doi.org/10.1073/pnas.1612908114.

[16] Ernazar Abdikamalov, Giulia Pagliaroli, and David Radice. *Gravitational Waves from Core-Collapse Supernovae*. 2022. arXiv: 2010.04356 [astro-ph.SR].

[17] J. Abadie et al. “SEARCH FOR GRAVITATIONAL WAVES ASSOCIATED WITH GAMMA-RAY BURSTS DURING LIGO SCIENCE RUN 6 AND VIRGO SCIENCE RUNS 2 AND 3”. In: *The Astrophysical Journal* 760.1 (2012), p. 12. DOI: 10.1088/0004-637x/760/1/12. URL: https://doi.org/10.1088/0004-637x/760/1/12.

[18] Nelson Christensen. “Stochastic gravitational wave backgrounds”. In: *Reports on Progress in Physics* 82.1 (2018), p. 016903. DOI: 10.1088/1361-6633/aae6b5. URL: https://doi.org/10.48550/arXiv.1811.08797.

[19] Robert S Shankland. “Michelson and his interferometer”. en. In: *Phys. Today* 27.4 (Apr. 1974), pp. 37–43.

[20] Eugene Hecht. *Optik*. De Gruyter, 2018. ISBN: 9783110526653. DOI: doi:10.1515/9783110526653. URL: https://doi.org/10.1515/9783110526653.

[21] Giles Hammond, Stefan Hild, and Matthew Pitkin. “Advanced technologies for future laser-interferometric gravitational wave detectors”. In: *Journal of Modern Optics* 61 (Feb. 2014). DOI: 10.1080/09500340.2014.920934.

[22] Christian Corda. “A clarification on a common misconception about interferometric detectors of gravitational waves”. In: (2011). DOI: 10.48550/ARXIV.1103.4783. URL: https://arxiv.org/abs/1103.4783.

[23] LIGO Caltech. *What is LIGO?* Last retrieved Wednesday 15th June, 2022, 08:33 from https://www.ligo.caltech.edu/page/what-is-ligo. 2022.

[24] Dennis Ugolini et al. “LIGO analogy lab—A set of undergraduate lab experiments to demonstrate some principles of gravitational wave detection”. In: *American Journal of Physics* 87.1 (Jan. 2019), pp. 44–56. DOI: 10.1119/1.5066567. URL: https://doi.org/10.1119/1.5066567.

[25] Peter R. Saulson. “Gravitational wave detection: Principles and practice”. In: *Comptes Rendus Physique* 14.4 (2013). Gravitational waves / Ondes gravitationnelles, pp. 288–305. ISSN: 1631-0705. DOI: https://doi.org/10.1016/j.crhy.2013.01.007. URL: https://www.sciencedirect.com/science/article/pii/S163107051300008X.

[26] Gabriela González. “Suspensions thermal noise in the LIGO gravitational wave detector”. In: *Classical and Quantum Gravity* 17.21 (2000), pp. 4409–4435. DOI: 10.1088/0264-9381/17/21/305. URL: https://doi.org/10.1088/0264-9381/17/21/305.

[27] S Hild et al. “Sensitivity studies for third-generation gravitational wave observatories”. In: *Classical and Quantum Gravity* 28.9 (2011), p. 094013. DOI: 10.1088/0264-9381/28/9/094013. URL: https://doi.org/10.1088/0264-9381/28/9/094013.

[28] D. V. Martynov et al. “Sensitivity of the Advanced LIGO detectors at the beginning of gravitational wave astronomy”. In: *Physical Review D* 93.11 (June 2016). DOI: 10.1103/physrevd.93.112004. URL: https://doi.org/10.1103/physrevd.93.112004.

[29] B P Abbott et al. “LIGO: the Laser Interferometer Gravitational-Wave Observatory”. In: *Reports on Progress in Physics* 72.7 (June 2009), p. 076901. DOI: 10.1088/0034-4885/72/7/076901. URL: https://doi.org/10.1088/0034-4885/72/7/076901.

[30] and J Aasi et al. “Advanced LIGO”. In: *Classical and Quantum Gravity* 32.7 (2015), p. 074001. DOI: 10.1088/0264-9381/32/7/074001. URL: https://doi.org/10.1088/0264-9381/32/7/074001.

[31] *General overview of the ET observatory layout*. Last retrieved Wednesday 15th June, 2022, 08:33 from http://www.gwoptics.org/research/et/layout/.

[32] Rudolf Gross and Achim Marx. *Festkörperphysik*. De Gruyter Oldenbourg, 2014. ISBN: 9783110358704. DOI: doi:10.1524/9783110358704. URL: https://doi.org/10.1524/9783110358704.

[33] I. D. Mayergoyz. “The Classical Preisach Model of Hysteresis”. In: *Mathematical Models of Hysteresis*. Springer New York, 1991, pp. 1–63. DOI: 10.1007/978-1-4612-3028-1_1. URL: https://doi.org/10.1007/978-1-4612-3028-1_1.

[34] Walter Heywang, Karl Lubitz, and Wolfram Wersing. *Piezoelectricity: evolution and future of a technology*. Vol. 114. Springer Science & Business Media, 2008.

[35] D. C. Jiles and D. L. Atherton. “Theory of ferromagnetic hysteresis (invited)”. In: *Journal of Applied Physics* 55.6 (Mar. 1984), pp. 2115–2120. DOI: 10.1063/1.333582. URL: https://doi.org/10.1063/1.333582.

[36] Jon Åge Stakvik et al. “On Implementation of the Preisach Model: Identification and Inversion for Hysteresis Compensation”. In: *Modeling, Identification and Control: A Norwegian Research Bulletin* 36.3 (2015), pp. 133–142. DOI: 10.4173/mic.2015.3.1. URL: https://doi.org/10.4173/mic.2015.3.1.

[37] Tiberiu-Gabriel Zsurzsan et al. “Preisach model of hysteresis for the Piezoelectric Actuator Drive”. In: *IECON 2015 - 41st Annual Conference of the IEEE Industrial Electronics Society*. IEEE, Nov. 2015. DOI: 10.1109/iecon.2015.7392524. URL: https://doi.org/10.1109/iecon.2015.7392524.

[38] Alexander Franzen. *gwoptics ComponentLibrary*. A free vector graphics library for illustrations of optics experiments. Last retrieved Wednesday 15th June, 2022, 08:33 from http://www.gwoptics.org/ComponentLibrary/. Licensed under a Creative Commons Attribution-NonCommercial 3.0 Unported License (see https://creativecommons.org/licenses/by-nc/3.0/). 2022.

[39] Berit Schlüter. *Personal communication*. Laser polarization studies conducted by Berit Schlüter, using the same laser model as in this work. 2021.

[40] Thorlabs Inc. *PA4HEW piezoelectric actuator product information*. Last retrieved Wednesday 15th June, 2022, 08:33 from https://www.thorlabs.com/thorproduct.cfm?partnumber=PA4HEW. 2022.

[41] Peter Bormann and Erhard Wielandt. “Seismic Signals and Noise”. en. In: *New Manual of Seismological Observatory Practice 2 (NMSOP2)* (2013). DOI: 10.2312/GFZ.NMSOP-2_CH4. URL: https://gfzpublic.gfz-potsdam.de/pubman/item/item_124248.

[42] Thorlabs Inc. *AV4(/M) Isolator Vibration Damping*. Product documentation plot. Last retrieved Wednesday 15th June, 2022, 08:33 from https://www.thorlabs.com/newgrouppage9.cfm?objectgroup_id=6421&pn=AV4/M. 2022.

[43] Hewon Jung and Dae-Gab Gweon. "Creep characteristics of piezoelectric actuators". In: *Review of Scientific Instruments* 71.4 (Apr. 2000), pp. 1896–1900. DOI: 10.1063/1.1150559. URL: https://doi.org/10.1063/1.1150559.

[44] Jon Age Stakvik. "Identification, Inversion and Implementaion of the Preisach Hysteresis Model in Nanopositioning". MA thesis. Norwegian University of Science and Technology, 2014.

[45] Xiaobo Tan, Ram Venkataraman, and P. S. Krishnaprasad. "&lttitle&gtControl of hysteresis: theory and experimental results&lt/title&gt". In: *SPIE Proceedings*. Ed. by Vittal S. Rao. SPIE, Aug. 2001. DOI: 10.1117/12.436463. URL: https://doi.org/10.1117/12.436463.

[46] Gravitational Wave Open Science Center. *Data release for event GW150914*. Last retrieved Wednesday 15th June, 2022, 08:33 from https://www.gw-openscience.org/events/GW150914/. Licensed under a Creative Commons Attribution 4.0 International (CC BY 4.0) License (see https://creativecommons.org/licenses/by/4.0/).

[47] Prof. Dr. Carsten Fallnich. *Personal communication*. Exchange on the use of mechanical preload to reduce hysteresis and creep in piezo actuators. 2021.

[48] Hiroshi Kaizuka and Byron Siu. "A Simple Way to Reduce Hysteresis and Creep When Using Piezoelectric Actuators". In: *Japanese Journal of Applied Physics* 27.Part 2, No. 5 (1988), pp. L773–L776. DOI: 10.1143/jjap.27.l773. URL: https://doi.org/10.1143/jjap.27.l773.

Acknowledgements

At this point I would like to thank all the people who supported me during this master thesis. I thank...

Prof. Dr. Alexander Kappes for welcoming me back into his working group for my master thesis, after I had already enjoyed writing my bachelor thesis in his group. Thank you very much for the great supervision and the continuous support through all the challenges that this project has brought over one and a half exciting years.

I would also like to thank Prof. Dr. Christian Weinheimer for kindly agreeing to be the second examiner of my thesis.

Furthermore, I would like to thank Prof. Dr. Christine Thomas and Alexander Mundt from the Geophysics department, who supported me with their knowledge especially concerning the seismic isolation of my setup, or rather the characterization of it. Many thanks also to Stefan Klingen, who provided and installed the seismometers for the vibration measurements.

Furthermore, I *shall* very much thank Daniel, Lew, Berit, Javi and Willem, who proofread my not-so-short thesis shortly before it was due, and helped me to correct more than just a few commas.

Of course I would also like to thank the whole AG Kappes for the great working atmosphere and the many breaks and mensa meals in between. It was one and a half years, and with the exception of a few pyramid-demolishing-excavator-destroying-my-measurement-data-days, I was looking forward to attending university every day.

And thank you Berit for the coffee breaks - I drink lots and lots of coffee, but I never cracked your high score on the coffee tally (I think it was 28 cups or something?) until today.

Outside of university, I also want to thank my family and friends who supported me in writing this thesis. A big thanks to mom and dad, thanks to whom I can live here in beautiful Altenberge, and thanks to my sister Sonja for the emotional and musical support. And hey, thanks to Jan, Korab, Simon and Alex. You guys are really the best. I really don't know how I would have made it through the last year and a half without you guys.

Declaration of Academic Integrity

I hereby confirm that this thesis on the "Setup and commissioning of a Michelson interferometer for the demonstration of gravitational wave detection principles in outreach activities" is solely my own work and that I have used no sources or aids other than the ones stated. All passages in my thesis for which other sources, including electronic media, have been used, be it direct quotes or content references, have been acknowledged as such and the sources cited.

Münster, Wednesday 15th June, 2022:

I agree to have my thesis checked in order to rule out potential similarities with other works and to have my thesis stored in a database for this purpose.

Münster, Wednesday 15th June, 2022: